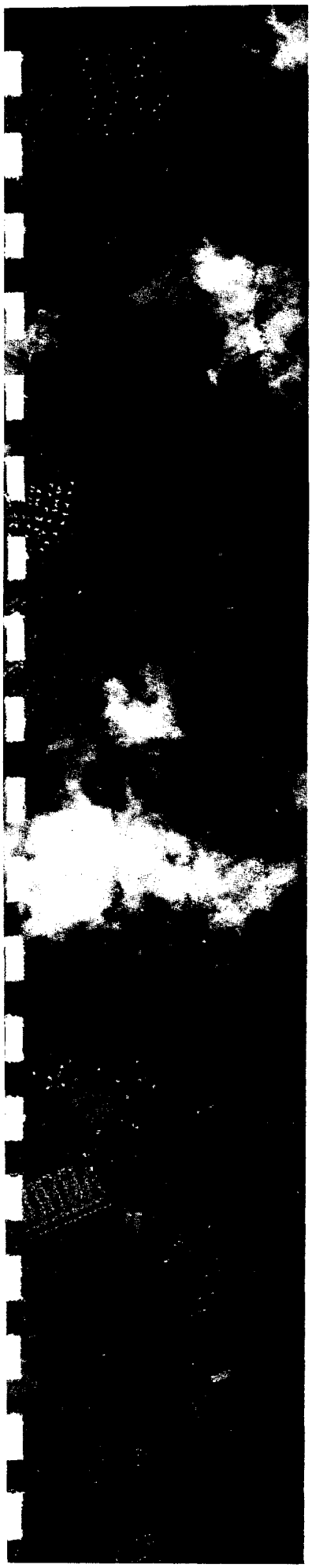

BIF-059-4035-69
Total No. of Pages 148
Copy No. 5 of 20 Copies

FINAL REPORT

IMAGE VELOCITY SENSOR PROGRAM

21 FEBRUARY 1969

Itek OPTICAL SYSTEMS DIVISION
ITEK CORPORATION • 10 MAGUIRE ROAD • LEXINGTON, MASSACHUSETTS 02173

SPG-69-013

CONTENTS

FIGURES

1. ABSTRACT AND INTRODUCTION

This final report summarizes the work accomplished by Itek on the Image Velocity Sensor (IVS) Development Program, contract no. [redacted] during the period 15 August 1967 to 31 January 1969. This program represents an extension of the work performed on the same contract reported in Itek document no. 9415-67-148.

The image velocity sensor, which is the subject of this report, is intended to be used in a high resolution photographic system consisting of a tracking mirror and frame camera. The available command signal for the tracking mirror is able to remove 99 percent of the image velocity resulting from the relative velocity of the earth and the vehicle. However, the resolution requirements of the system are such that further reduction of the image velocity is required. The Image Velocity Sensor measures the residual velocity at the center of the camera format, and its outputs are used to correct the tracking mirror rates in order to reduce that velocity to zero.

Since the Image Velocity Sensor is used in a nulling servo loop, the primary performance characteristics are bias, which affects the null accuracy, and linearity and gain, which affect the servo stability. The Itek sensor exhibits the following characteristics:

Bias $\leqq$ 0.004 inch per second

Linearity = $\pm$ 10 percent

Gain factor = 16.67 volts per inch per second $\pm$ 25 percent for a wide variety of input conditions

These characteristics are discussed in detail later in this report. Report no. BIF-059-9585-68 is a briefing of the acceptance test results obtained 3 December 1968.

Included in this report is a discussion of the theory of operation of the sensor and the results of experimental investigations. During the reporting period, two generations of the IVS were fabricated and tested. The differences between these two units, and their impact on performance, are presented in detail. Tests involving a picturephone camera are summarized and the development of an intensified vidicon camera is discussed. Potential sensor improvements are examined. Further mathematical model computer study results are presented. Results of an investigation made into the effects of helium on a vidicon are also discussed.

2. THEORY OF OPERATION

2.1 SIMPLIFIED ANALYSIS

The Itek Image Velocity Sensor (IVS) employs a vidicon tube as the image motion sensing device. Fig. 2-1 illustrates the vidicon principle of operation. An optical image focused on the surface of the photoconductor generates local conductivity changes in the photoconductor material. This action results in a charge pattern which is read out by a scanning electron beam. An equivalent circuit is shown in Fig. 2-2. Momentary passage of the electron beam over a spot charges the capacitor to the target voltage. Until the beam returns, the capacitor discharges through a resistance whose value is an inverse function of the local illumination, providing a charge reduction proportional to the time integral of illumination. Signal current is generated when the charge on the capacitor is restored by the beam. Integration also results from the combination of photoconductive and readout lags.

Smear, resulting from image motion, reduces the high frequency content of the video signal. The diagrams on Fig. 2-3 show this effect on a single scan line. The reduction in average value after passing the video signal through a high-pass filter and rectifier is a measure of the smear. In order to sense the direction of the image velocity, a modulator is provided which sinusoidally increases and decreases the input velocity (see Fig. 2-4). Subsequent demodulation of the rectified video signal provides direction sensing.

An approximate expression for the rectified video voltage as a function of smear is

$$E \simeq E_0 (1 - k S^2) \tag{2.1}$$

where E = rectified video voltage, volts
E_0 = rectified video voltage with zero smear, volts
S = smear, inches
k = constant, inches^{-2}

The modulated image velocity, V, produces a smear during the integration time, t_i, of magnitude

$$S \simeq \int_{t-t_i}^{t} V dt = \int_{t-t_i}^{t} (V_i + V_m \sin \omega t)\, dt \tag{2.2}$$

where V_i = input velocity, inches per second
V_m = peak modulation velocity, inches per second
ω = modulation frequency, radians per second

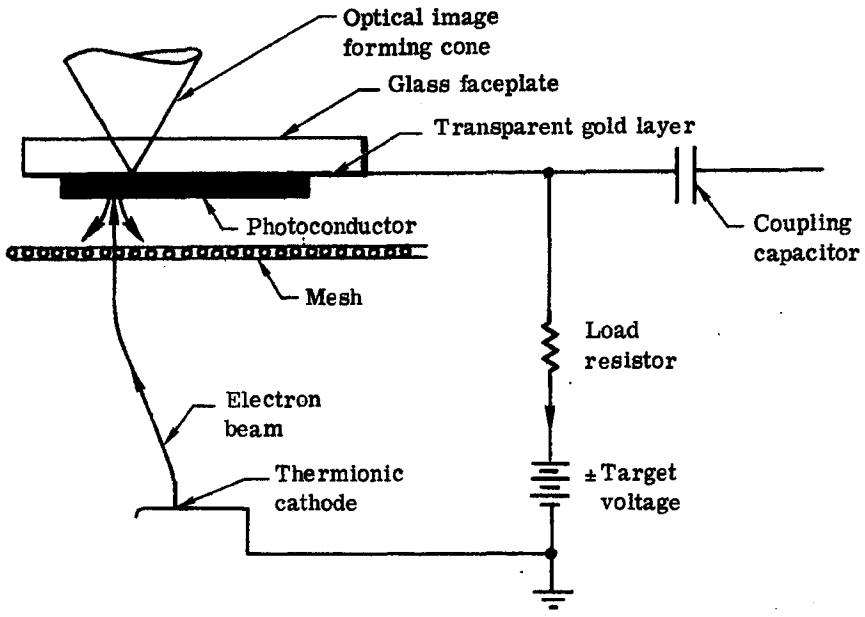

Fig. 2-1 — Vidicon principle

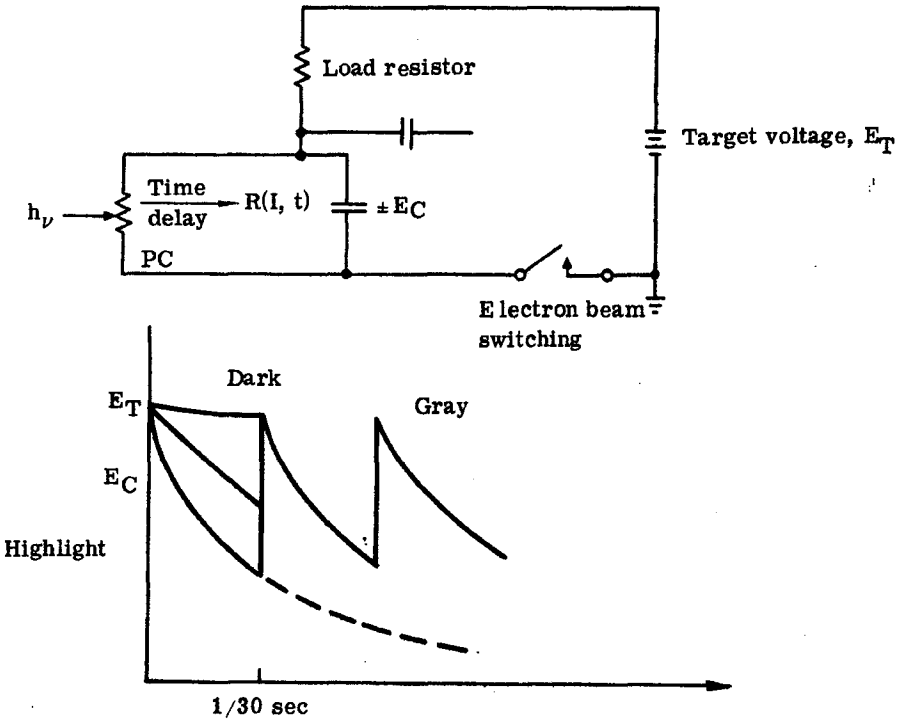

Fig. 2-2 — Equivalent vidicon circuit

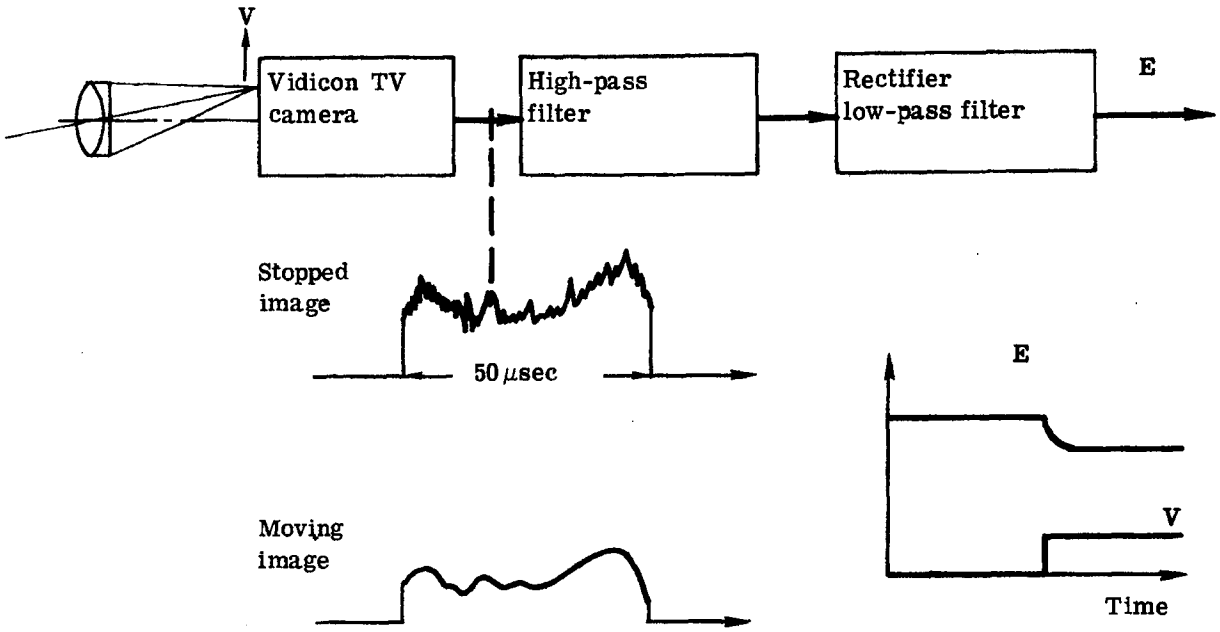

Fig. 2-3 — Rudimentary sensor

NOTE: Cylic image motion added with modulator

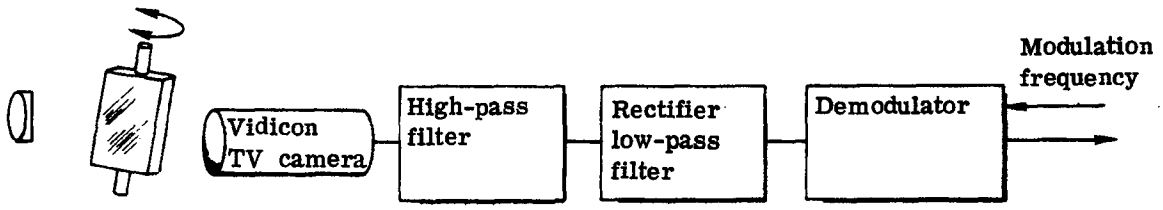

Fig. 2-4 — Sensor with modulation

$$S \simeq \left[V_i\, t - \frac{V_m}{\omega} \cos \omega t\right]_{t-t_i}^{t} \tag{2.3}$$

$$\simeq V_i\, t - V_i(t - t_i) - \frac{V_m}{\omega} \cos \omega t + \frac{V_m}{\omega} \cos \omega(t - t_i) \tag{2.4}$$

$$\simeq V_i\, t_i + \frac{2V_m}{\omega} \sin \frac{\omega t_i}{2} \sin \omega \left(t - \frac{t_i}{2}\right) \tag{2.5}$$

Substituting Equation (2.5) into Equation (2.1) and collecting terms yields

$$E \simeq E_0 \left[1 - k\, V_i^2\, t_i^2 - \frac{2kV_m^2}{\omega^2} \sin^2 \left(\frac{\omega t_i}{2}\right)\right]$$

$$+ E_0 \left[\frac{-4kV_m}{\omega}\, t_i \sin \left(\frac{\omega t_i}{2}\right)\right] V_i \sin \omega \left(t - \frac{t_i}{2}\right)$$

$$+ E_0 \left[\frac{2kV_m^2}{\omega^2} \sin^2 \left(\frac{\omega t_i}{2}\right)\right] \cos 2\omega \left(t - \frac{t_i}{2}\right)$$

$$\simeq E_{DC} + E_f + E_{2f}$$

The following relationships are evident:

1. The fundamental component, E_f, is proportional to V_i.
2. Dividing the magnitude of E_f by the magnitude of E_{2f} yields a signal which is independent of the scene characteristic, E_0.

$$\frac{E_f}{E_{2f}} = -\frac{4V_i}{V_m} \frac{\frac{\omega t_i}{2}}{\sin \frac{\omega t_i}{2}}$$

3. E_{DC} can also be used for normalization.

$$\frac{E_f}{E_{DC}} = \frac{\frac{-4k\, V_m}{\omega}\, t_i \sin \frac{\omega t_i}{2}\, V_i}{1 - k\, V_i^2\, t_i^2 \frac{-2k\, V_m^2}{\omega^2} \sin^2} \left(\frac{\omega t_i}{2}\right)$$

$$\simeq \frac{-4k\, V_m\, t_i}{\omega}\, V_i \sin \frac{\omega t_i}{2}$$

2.2 EXPERIMENTAL INVESTIGATIONS

2.2.1 Bias

The Itek sensor provides an output response to any image velocity however small. Thus, it can be stated that the sensor has a zero threshold. However, like nearly all analog instruments,

it does have what is variously called bias, offset or null (a small output, dependent on a number of conditions, even in the absence of image velocity). Since the previous report, dated 15 August 1967, a concerted effort has been made to determine the causes of bias and to reduce it well below the tolerable limit. This effort has been successful as the test results described in Section 3.3 indicate. Bias was found to have a systematic as well as a random component.

2.2.1.1 Systematic Bias

As described in the previous report, the signal from the vidicon is split electrically into two channels corresponding to two different patches on the vidicon raster in order to provide two-axis sensing. The original sensor split the raster on a line basis—the signal from the first half of every scan line was used to sense cross-track velocity and the signal from the last half of every scan line was used to sense along-track velocity. This method has the advantage of a higher sampling rate over the alternative, split-field approach. Bias tests were made with the TV camera in the brassboard sensor head which was mounted on the simulator. During the testing, it became increasingly apparent that the bias in one channel was nearly invariably positive, and the other was, with few exceptions, always negative. To eliminate the possibility that the two channels in the electronics were causing this condition, one channel was used with an external gating signal whose width and position in the video line could be controlled. The offset remained opposite in sign in the two half lines. The camera was then rotated 180 degrees, to cause the first half of the line to scan the image seen previously by the second half line. The polarity of the offsets for each half line reversed, thus eliminating the possibility that the electronics was treating one portion differently than the other. Also, when the glass plate in the modulator was removed, the bias disappeared. The source was therefore confined to either the vidicon camera or the optical system. The camera was removed from the brassboard sensor head and returned to the breadboard setup, viewing the film target belt through a Schneider lens. The same results were obtained. Therefore, the problem appeared to be due either to some peculiarity of the vidicon camera such as nonuniformity of sensitivity of the target surface, or to some nonuniformity effect on the image by the modulator-lens combination.

A test arrangement was built to isolate the bias cause to one of the two possibilities. This setup allowed for translation of the TV camera head in 1/8-inch steps normal to the optical axis and parallel to the raster scan lines. Bias measurements were made at each of five different camera head positions: 0, +1/8, +1/4, −1/8, and −1/4 inch. The scene, imaged on the vidicon face, was kept stationary and, thus, the image stayed fixed in space except for modulation. By means of an external gating signal, the sensor processing electronics was made to look at a portion of the raster which was a window 0.375 by 0.150 inch. The 0.150-inch dimension was in the direction of the scan lines. The total raster area is 0.375 by 0.500 inch. The gating signal was varied to adjust the window position in the scan direction in steps of 0.025 inch. Bias measurements were made at each of the five camera positions. By this means, it was possible to compare the bias for the same portion of the scene imaged at different places on the vidicon raster. Had the bias remained constant at different positions on the raster, the vidicon could be ruled out as the bias cause. However, such was not the case. The bias varied in a fairly consistent manner as a function of position on the raster, thus indicating that a vidicon characteristic apparently is involved in the systematic bias generation. Further tests on the systematic bias are summarized below. The optomechanical configuration and the block diagram of the test setup are shown in Figs. 2-5 and 2-6. The reference mark on the raster is simply to show the orientation of the TV camera, since for some tests the camera was rotated 180 degrees about the tube axis. The arrow on the raster labeled "scan" shows the first scan line. Normal scan is as shown. Some tests used reversed horizontal and/or vertical scan reversed electrically.

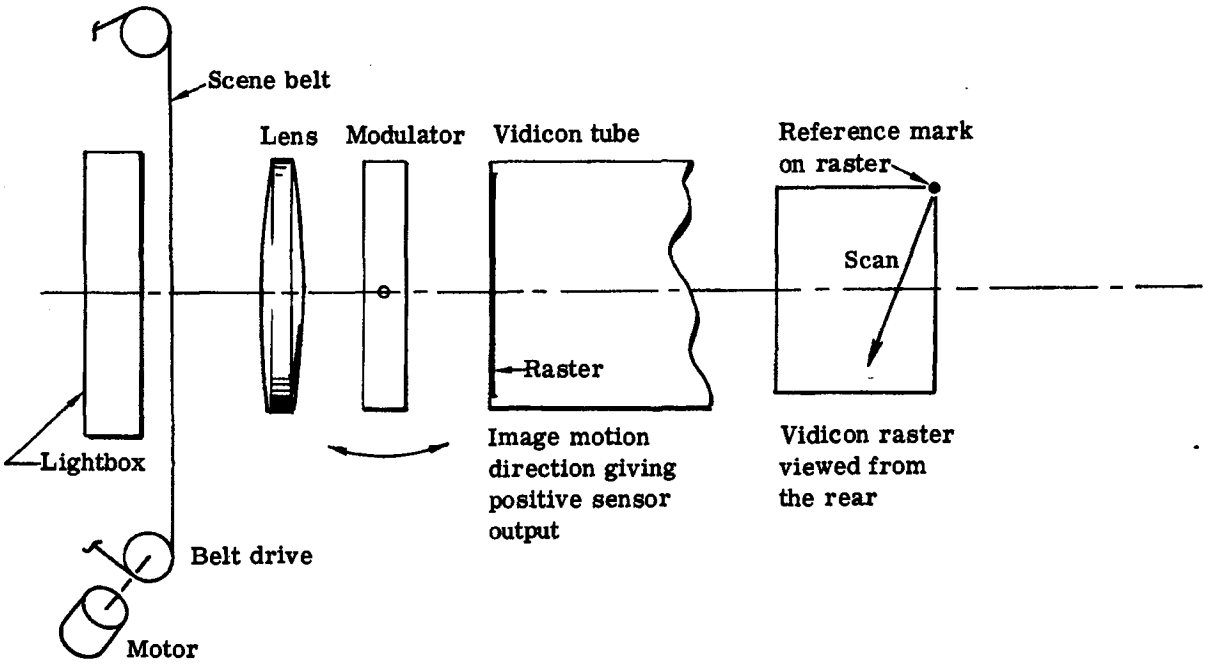

Fig. 2-5 — Sensor optical mechanical configuration

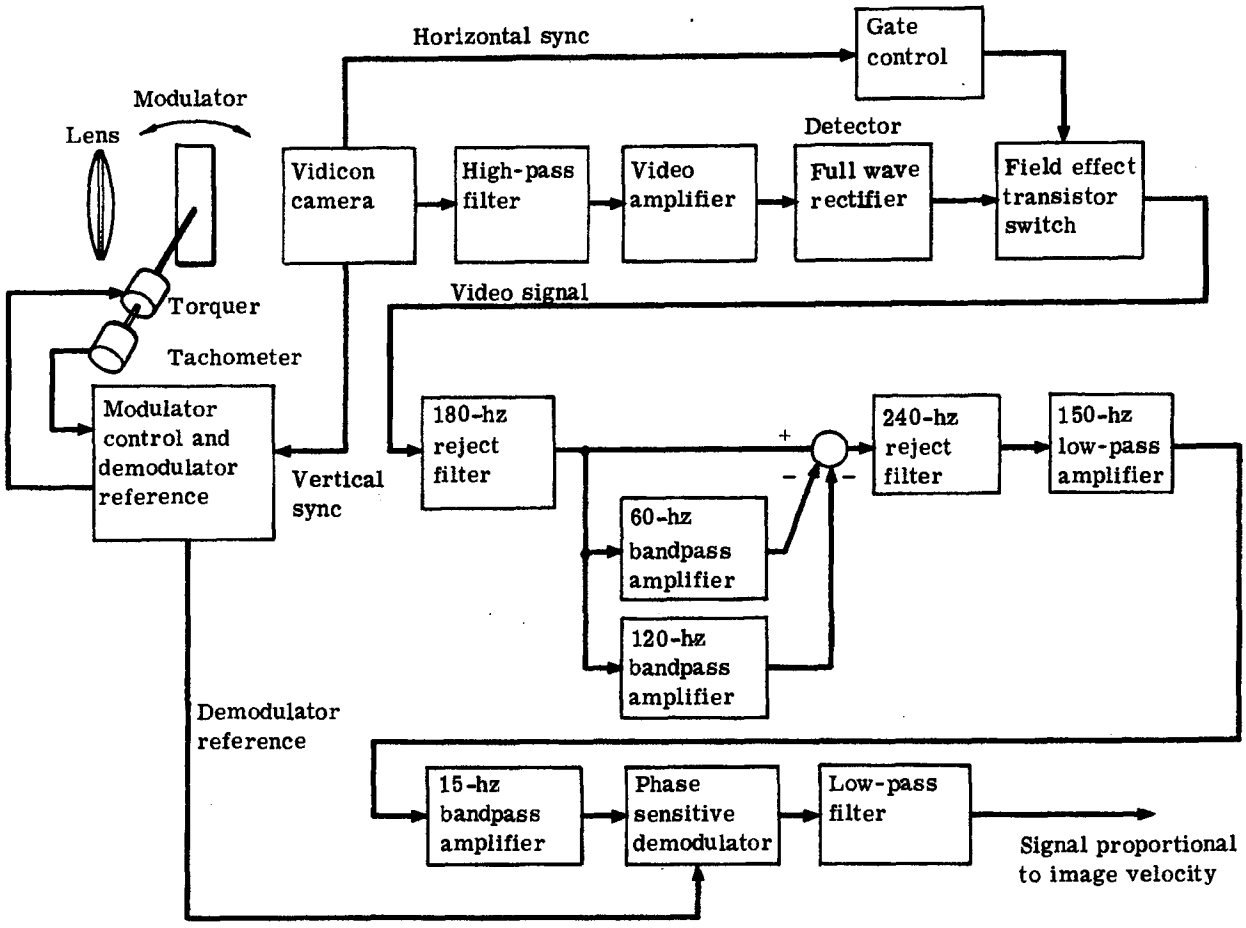

Fig. 2-6 — Diagnostic testing block diagram

1. Bias as a function of the position of the video information on the raster has the characteristic shown in Fig. 2-7. This characteristic is obtained whether the vidicon camera axis is aligned with, above, or below the lens optical axis. Other TV cameras all had this same characteristic. The variation in bias with position in the raster is not due to a phase shift but rather to an amplitude change in the signal prior to demodulation.

2. The above characteristic is decreased for a camera horizontal alignment change which causes the raster to shift to the "right" as in Fig. 2-7. It is increased for the opposite alignment change. In general, the bias polarity can be reversed by an alignment control change.

3. The camera electronic focus has a small effect on bias. If the horizontal alignment is adjusted to give zero bias for some portion of the raster used, an adjustment of the focus voltage up and down causes the bias to go plus and minus slightly. Whether an increase in focus voltage causes a positive or negative bias depends on what portion of the raster is used. Vertical alignment changes also alter bias slightly. However, neither of these controls affects bias nearly as significantly as the horizontal alignment.

4. If the TV head is rotated 180 degrees about its axis, for a random scene, the bias for a given position on the raster stays at roughly the same magnitude but reverses in polarity.

5. For a scene which is a slit of light at right angles to the scan direction, the bias is more positive if the direction of scan is the same as the image motion direction which gives positive sensor output. The bias with a real scene does not change appreciably with change in scan direction.

6. The bias characteristic is not altered if the modulator is in a telecentric beam. Making the modulator asynchronous with the TV frame rate does not eliminate bias.

Some of these test results are illustrated in Figs. 2-8 through 2-11. The effect of alignment control on the dark signal from the camera is shown in Fig. 2-12.

From the above, it is concluded that the bias as a function of position of information on the raster is caused by the inherent nature of the electron-optical scanning process which causes a gradient of sensitivity along the scan lines peaking in the center and dropping off on both sides. Therefore, with the split line method, an alignment control setting which gives zero average bias along full lines would result in both channels producing a bias, but of opposite polarities, as was noted experimentally above. One solution considered was to dynamically vary the alignment as a function of horizontal scan position. Since the bias due to either the first half line or the second half line information could be zeroed by the proper alignment setting, the proper dynamic variation of alignment should be able to produce simultaneously zero bias in both channels. This technique was attempted but it was found unfeasible to vary the alignment current at the line rate to the extent required. Another solution was to change to field splitting and to invert the aspect ratio. Instead of using a 4 by 3 horizontal to vertical, a 3 by 4 horizontal to vertical aspect ratio is used. The advantage is that with shorter horizontal lines, there is a smaller gradient, and, since full lines are used in each channel, the bias can average to zero along the lines with the proper alignment setting. This latter solution was the one actually used, and proved quite successful. It was found unnecessary to change alignment current from one half field to the next. This could easily have been done at the field rate.

2.2.1.2 Random Bias

In addition to the systematic bias discussed above, there is a bias which varies in magnitude and sign as a function of the particular portions of the image which oscillate about the edges of the

raster due to the modulation process. The average detected video can vary at a fundamental rate (resulting in bias) due to information coming into and out of the raster at the edges. One solution considered was to use a mechanical mask at the vidicon face to confine the image passing through the mask to be slightly smaller than the raster length. The mask would oscillate in synchronism with the optical modulation so as to keep the same image on the face of the vidicon. The edges of the image as defined by the mask would be confined to remain within the raster, and thus, no information would pass into and out of the raster. This technique was tested experimentally, simply by placing a corresponding mask on the scene which remains fixed. This approach is equivalent to moving the mask at the image. This had the effect of increasing the systematic bias due apparently to the effect of a sharp transition in signal when the scanning beam passed from the masked region of the raster to the unmasked region. Due to this, and the added complexity of actually implementing the method, the idea was not pursued further.

This bias can be decreased by decreasing the modulation amplitude, thus minimizing the information coming into and out of the raster. However, the linear range of the sensor is directly proportional to the modulation amplitude, and due to the required range, this method could not be employed.

Two techniques which did prove very effective were: (1) set the demodulator phase in quadrature with the random bias phase; and (2) raise the low cut-off end of the video bandpass filter from 100 to 700 khz. Because the edge effect bias is a function of modulation displacement, whereas the velocity sensitive signal is a function of modulation velocity, it would be expected that there would be a phase difference between the two fundamental signals. Previously, the demodulator had been set to be in phase with the fundamental detected video signal for a high velocity image in order to give maximum sensitivity. Measurement of the phase of the bias relative to that of the velocity signal showed that the bias could be removed with only a minor sacrifice in output sensitivity.

Figs. 2-13 and 2-14 show phase measurements at 7.5 and 15 hz, respectively, of the fundamental with image velocity and with no image velocity and the image positioned to give a high edge bias.

Fig. 2-15 shows an early test result illustrating the effect of changing the demodulator phase from that which gave maximum sensitivity to that which gave minimum edge bias. The edge bias was drastically reduced while the sensitivity was reduced by only 17 percent. The edge bias produced predominantly low frequency video information. Raising the low cut-off end of the video bandpass, therefore, reduced the edge bias at a further decrease in sensitivity. The signal-to-noise ratio was still quite good, however.

2.2.2 Linearity

An important system requirement is that the sensor output versus velocity is linear. Experiments determined that two criteria must be met in order to acquire linearity: (1) the average illumintion on the face of the vidicon must be at least 1 foot-candle; and, (2) the peak image modulation velocity on the vidicon face must be roughly double the dynamic range on the vidicon face over which linearity is required. The first of the above is covered in detail in Section 3.1. Fig. 2-16 illustrates the second criterion. The two curves show sensor fundamental output versus image velocity for a particular scene at an illumintion of 2 foot-candles on the vidicon. Three conclusions can be drawn: (1) the maximum sensor output occurs for an image velocity roughly equal to the peak modulation velocity; (2) at low image velocities, the sensitivities at the two conditions are almost equal; and (3) adequate linearity occurs for image velocities up to about half the peak modulation velocity.

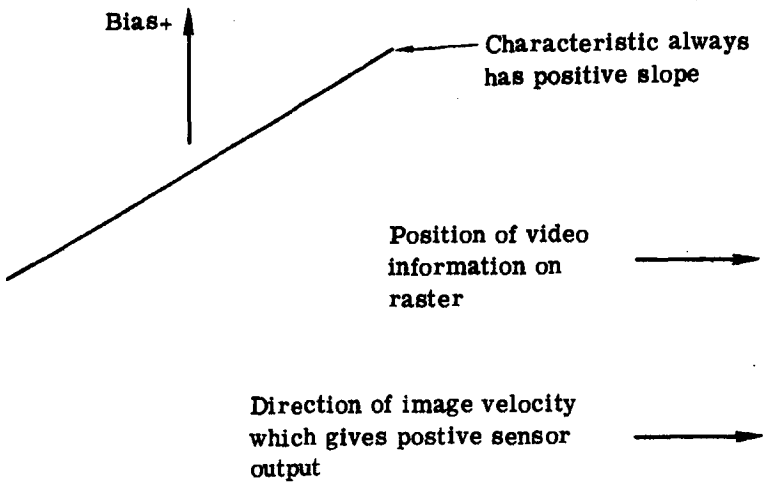

Fig. 2-7 — Bias versus position of video information on raster

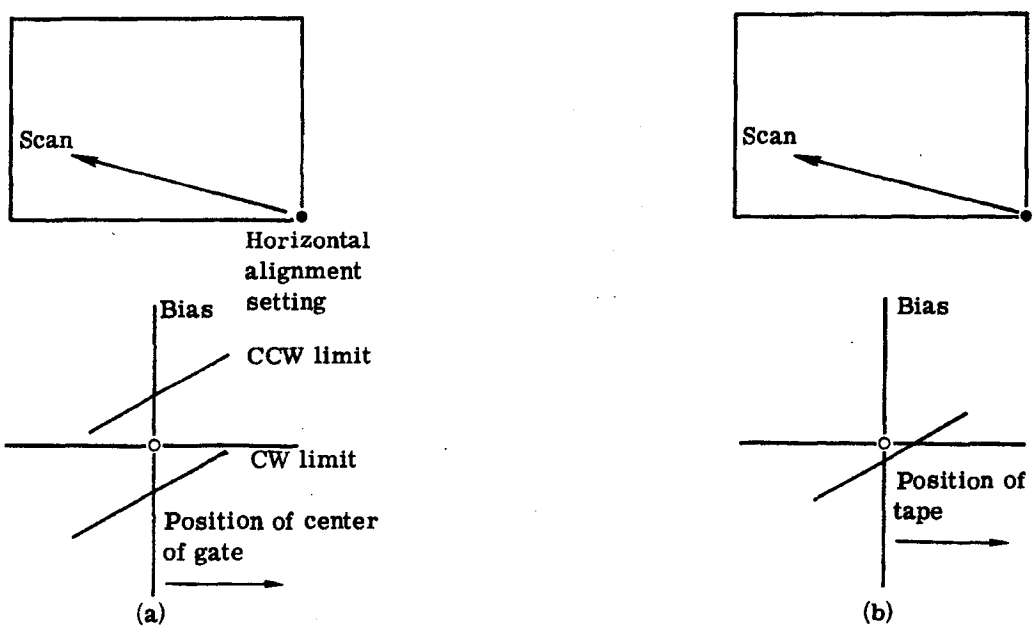

Fig. 2-8 — Test results of electrically reversed horizontal and/or vertical: (a) random scene (half line width gate used); (b) scene consisting of a uniform illumination source with a nonilluminated stripe approximately 0.030 inch on raster at right angles to scan direction, without gating

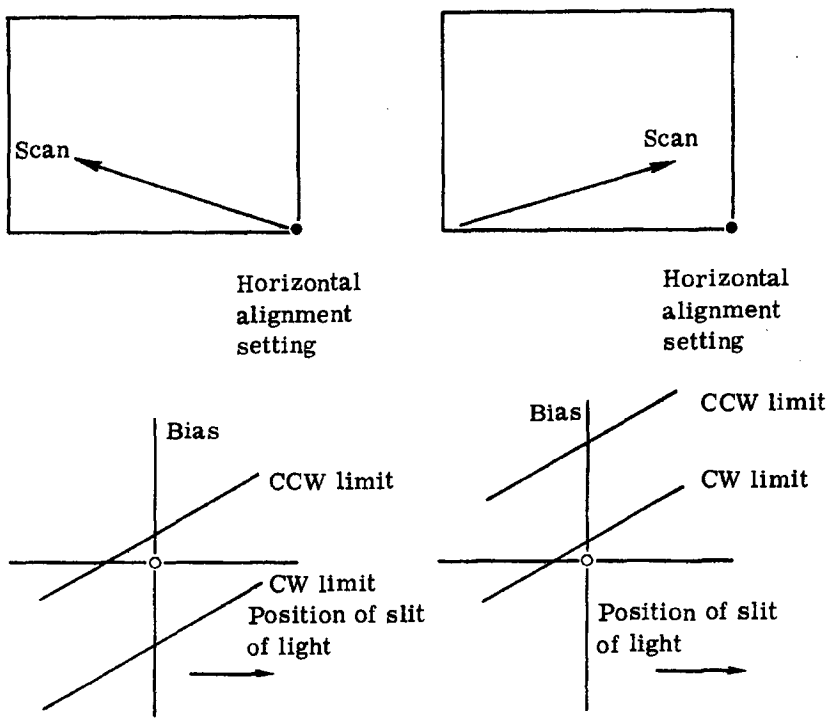

Fig. 2-9 — Test result (scene was a slit of light approximately 0.007-inch width on raster and at right angles to scan direction, without gating)

Fig. 2-10 — Real scene modulator in telecentric beam (half line width gate used)

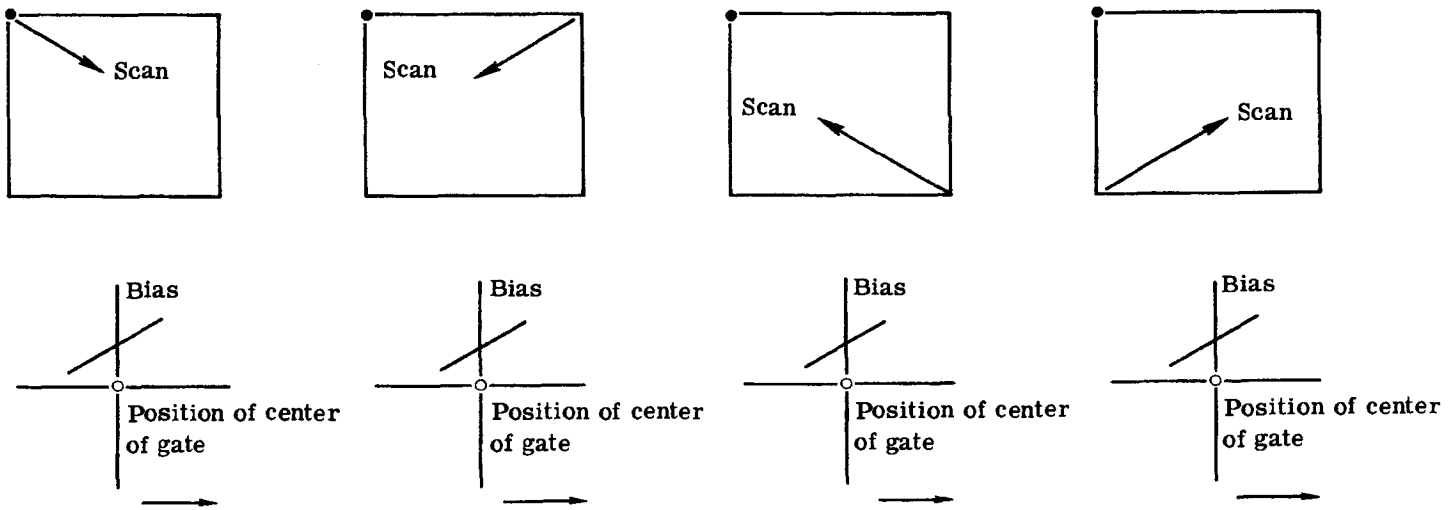

Fig. 2-11 — Real scene modulator in telecentric beam (half line width gate used, TV head rotated 180 degrees about optical axis from normal orientation)

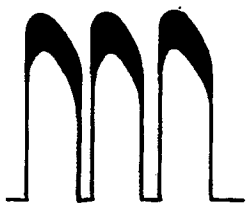

Three lines of dark signal with alignment control set at CW limit

Three lines of dark signal with alignment control set at CCW limit

Fig. 2-12 — Effect of alignment control on dark signal

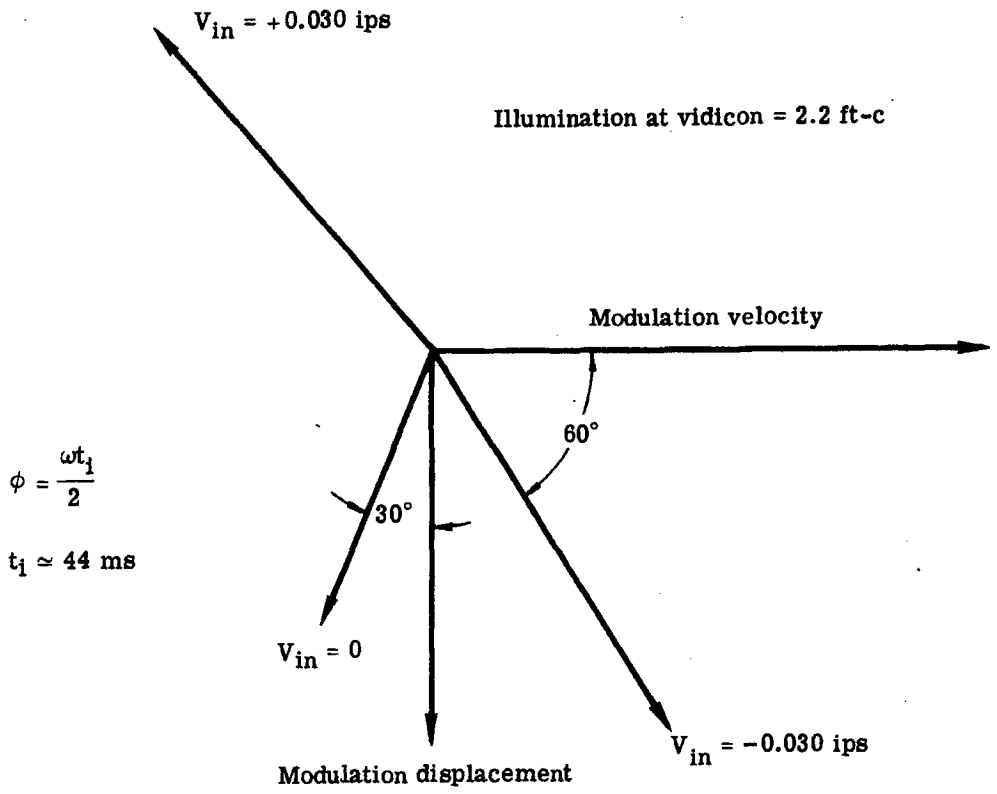

Fig. 2-13 — Null and velocity phase relationships, 7.5-hz modulation

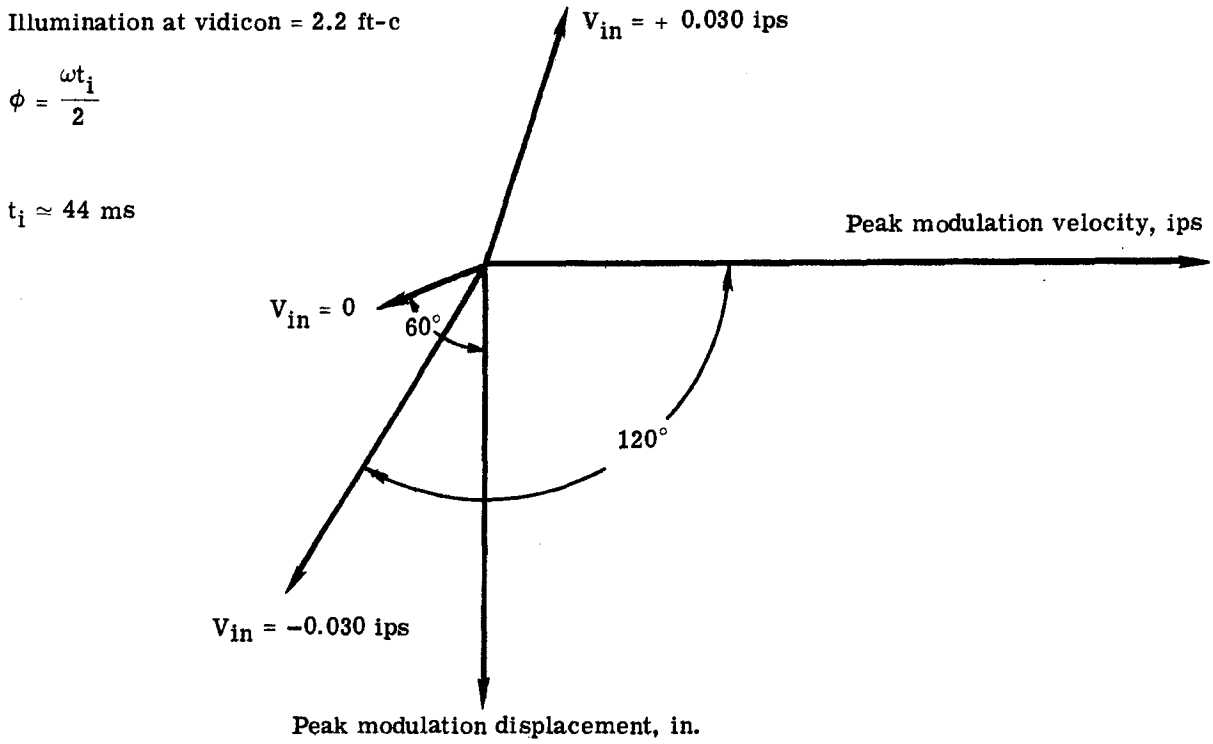

Fig. 2-14 — Null and velocity phase relationships, 15-hz modulation

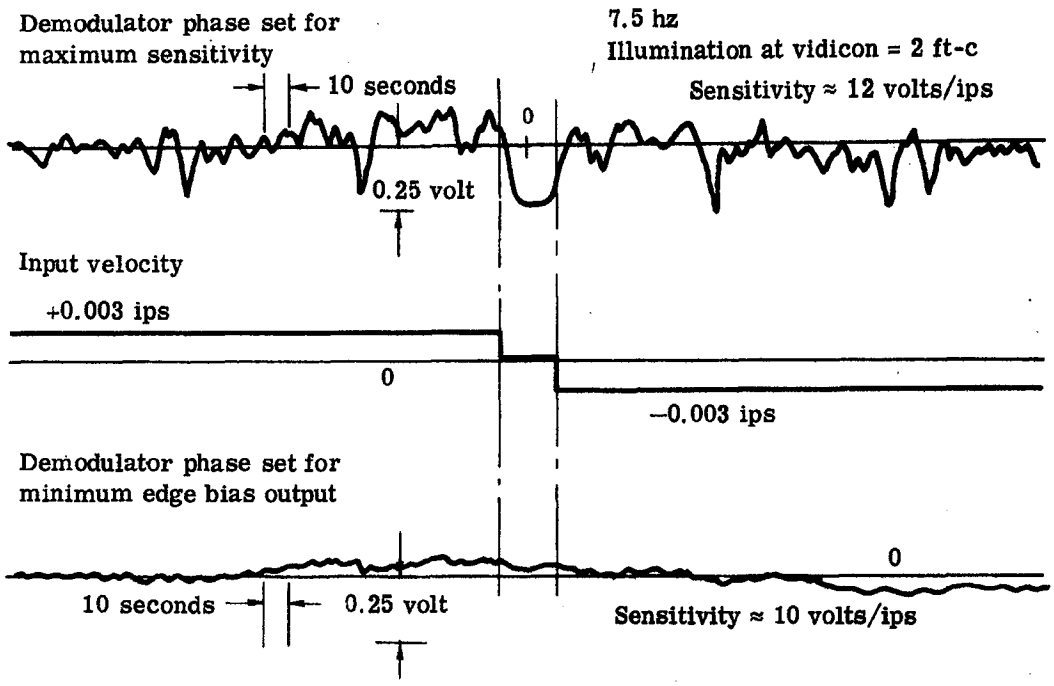

Fig. 2-15 — Demodulated output

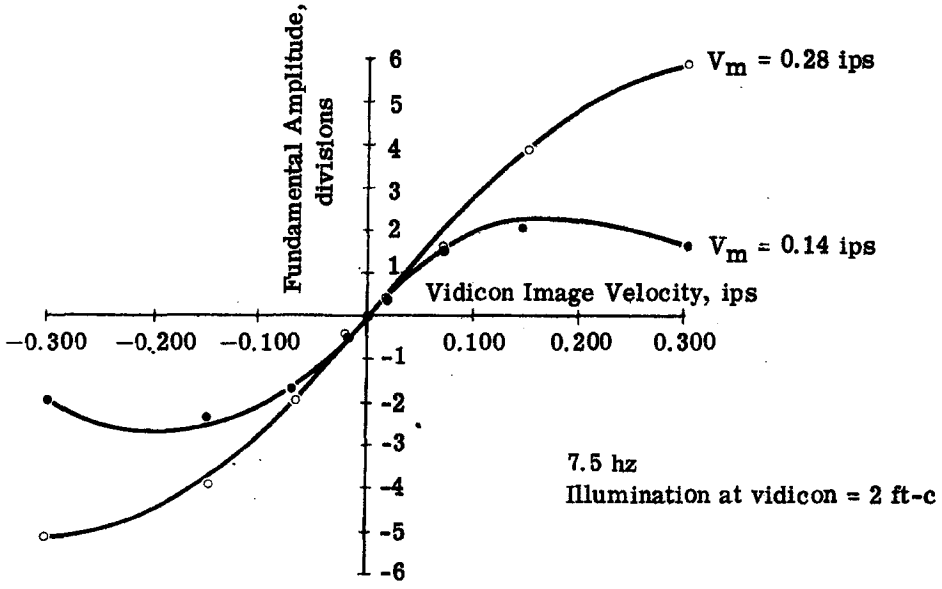

Fig. 2-16 — Dynamic range as a function of modulation amplitude

Since the edge bias varies directly with modulation amplitude, the modulation velocity should be minimized consistent with other requirements. The required dynamic range at the interface is 0.3 ips, which is 0.158 ips at the vidicon due to the 1.9 to 1 minification. The choice of 0.28 ips peak modulation gave a sensor output which became only slightly nonlinear at 0.3 ips.

2.2.3 Automatic Gain Control (AGC)

The Itek sensor does not inherently produce an output signal with a constant volt/inch/second sensitivity or gradient. The inherent sensitivity varies as a function of image content and illumination. Therefore, some sort of automatic gain control is necessary in order that the sensitivity remain within specifications: nominal, ±25 percent. The previous AGC utilized a feedback scheme which essentially varied the sensor gain in order to keep the second harmonic component of the detected video a constant. The shortcomings of this scheme are discussed in Section 3.2. Because of these shortcomings, some other method had to be developed. Section 6 of Appendix A provides the theoretical basis for an AGC based on the mathematical model of the sensor. The normalizing (or AGC) signal is derived from a separate bandpass filter and detector connected to the output of the video amplifier and bandpass filter which is used to derive the velocity signal. The analysis in Section 6 of Appendix A shows that the average output of the above detector is proportional to the sensitivity if the proper separate filter is used.

In the experimental investigation of this approach, simultaneous recordings were made of the sensor fundamental with scene velocity, the average output of the above special filter-detector, and also the average output of the normal video detector from which the fundamental is derived. The two average detected video signals varied nearly identically except for a constant scale factor as the scene was moved. Also, this variation was the same as the envelope of the fundamental. Fig. 2-17 shows one test recording of fundamental and average rectified video. These signals vary similarly with scene. These results gave indications that the approach was feasible. However, even in the absence of scene information, there was a significant amount of detected video due to amplifier noise, and to imperfections of the fiber optics when an intensifier was used. Therefore, a feedback scheme to vary amplifier gain to maintain a constant detected video output could not be used. Instead, the contribution due to amplifier noise and fiber optics had to be subtracted from the gross detected video in order to obtain a net signal due only to scene content. This signal is then proportional to the sensor gradient. In order to obtain a fixed gradient, the gain within the sensor must be divided by this net signal using an analog divider.

Experiments were run with the above approach, using a separate bandpass filter and detector and also using the normal bandpass filter and detector from which the fundamental is derived. The latter gave results at least as good as using the separate bandpass filter and detector. This latter, simpler, method was used. The analysis in Section 6 of Appendix A shows that the use of the separate filter-detector should give better results. The discrepancy between theory and experiment is attributed to the extraneous video due to noise and the fiber optics. The test results on the final system for a wide variety of conditions indicated good performance for the AGC used. This is discussed in detail in Section 3.

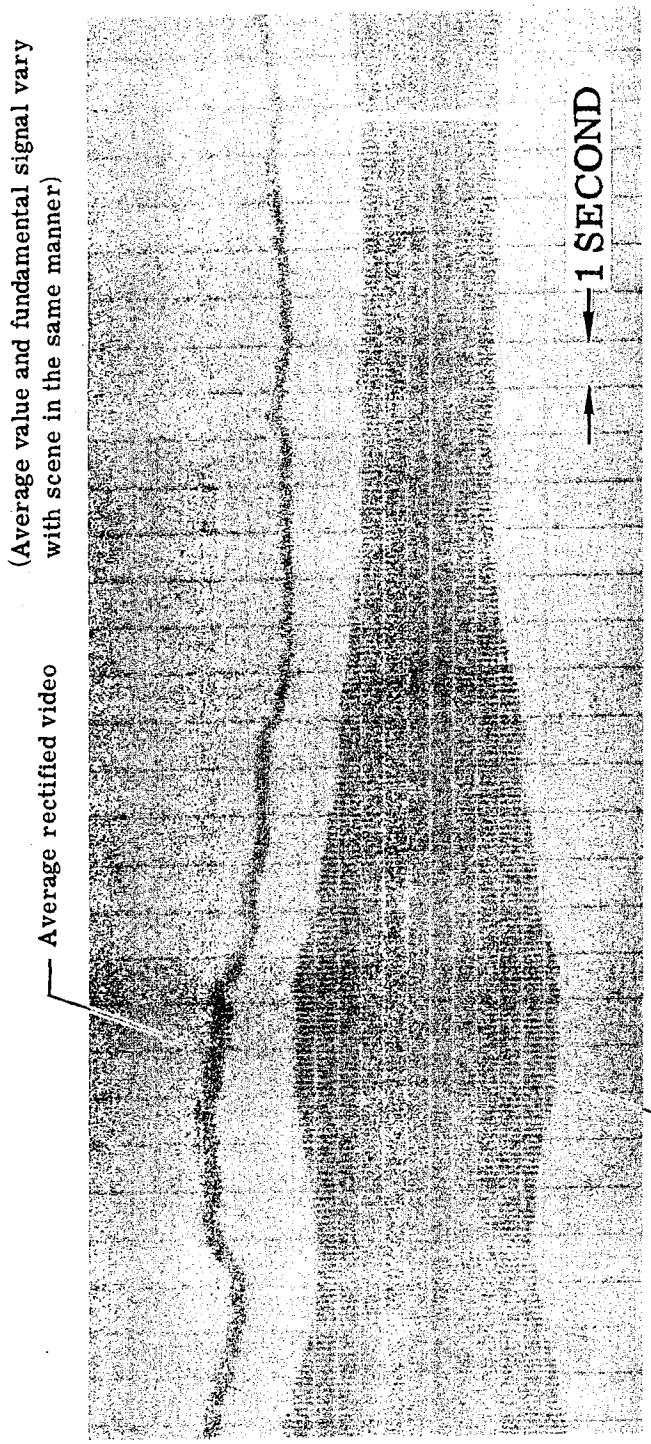

Fig. 2-17 — Automatic gain control (AGC)

3. ENGINEERING TEST MODEL AND ENGINEERING PROTOTYPE EVALUATION MODEL

An engineering test model sensor, designated Engineering Test Model A (ETMA) was delivered to the General Electric Company for evaluation. This unit was the only deliverable hardware produced during this program phase.

The ETMA sensor head, shown in Fig. 3-1, is the same as the brassboard unit shown in "Image Velocity Sensor, 15 August 1966 to 15 August 1967," report no. 9415-67-148 with the following exceptions:

1. A counterweight has been added to provide first moment balance of the rotating section.
2. The handwrapped magnetic shielding around the torquer-tachometer has been replaced with a custom fabricated shield.
3. The painted surfaces were replaced with black anodize to eliminate the problem of paint flakes on the optical surfaces.

The unit was aligned using the same approach as shown on page 4-1 of the above referenced report.

The electronics portion of the sensor was packaged in a rack with plug-in modular universal printed circuit boards.

Prior to delivery, the ETMA sensor was tested at Itek on the two-axis simulator developed on the earlier contract phase. The results of this testing are presented in a separate document (Itek document no. 9415-68-225, Test Report, Image Velocity Sensor, dated 27 March 1968). The report contains a description of the tests, a discussion of the test results, and copies of the test procedure, data sheets, and photographs of the scene material. All tests were performed in the open-loop mode; i.e., the sensor output was not fed back to reduce the input velocity.

The ETMA sensor was delivered to the General Electric Company at Valley Forge, Pennsylvania on 18 January 1968, where it underwent further tests on the GE Beta subsystem tester. These were also open-loop tests.

Both the Itek and GE tests indicated areas of performance which required improvement, notably null accuracy, linearity, and gain control. To this end, further development testing and the design of an Engineering Prototype Evaluation Model (EPEM) were initiated following the delivery of ETMA. These efforts were performed under a subcontract from the General Electric Company.

The development testing has been discussed in Section 2 of this report. The EPEM sensor, shown in Figs. 3-2 and 3-3, was tested at Itek and delivered to the General Electric Company on 3 December 1968. A photograph of the test setup is shown in Fig. 3-4. The simulator is the one

designed and built under contract [redacted] with the exception that a haze source and pellicle beam splitter were added to provide control of the image plane contrast.

The following sections compare the design features of ETMA and EPEM as they relate to the performance characteristics of the sensor. Since the two units were not tested under the same scene and illumination conditions, direct comparison of test results is not possible. However, the primary performance characteristics, linearity, null accuracy, and gain control, were evaluated for both units, and test results are presented.

Fig. 3-5 is a block diagram of the ETMA sensor and Fig. 3-6 shows the EPEM block diagram. The major differences between the two are shown in Table 3-1 and are discussed in detail in the following sections.

3.1 LINEARITY

One of the significant differences between the ETMA and EPEM sensors is the addition of an image intensifier to the EPEM. The ETMA unit contained an 8567 vidicon in the sensor head. The same type vidicon was used in the EPEM unit, except for a fiber-optics faceplate which was added to mate with the output face of the single stage image intensifier that preceded it. In addition to the obvious improvement in low light level performance, the image intensifier provided two significant benefits. The first, which will be discussed in detail in a later section of this report, is the capability to control the illumination on the face of the vidicon. The second, a relatively high illumination on the vidicon face, results in a sensor output signal that is linear with input velocity. It is this characteristic that will be discussed here.

Testing of ETMA revealed that the output signal was nonlinear, and that the degree of nonlinearity was a function of the illumination level. Fig. 3-7 is a plot of sensor output versus image velocity at the vidicon face as a function of vidicon illumination. These tests were performed without gain control, so the results are indicative of the basic characteristics of the ETMA sensor. It is evident from the curves that an illumination level of at least 1 foot-candle is required to produce a linear output signal. The addition of gain control increases the low light level signal and decreases the output signal with high illumination, but does not affect the basic characteristics. Curves of sensor output with AGC versus vidicon image velocity for the same conditions as Fig. 3-7 are shown in Fig. 3-8. Again, the curve for 1 foot-candle is straight, and the nonlinearity at low velocity inputs increases as the illumination level decreases.

From a system standpoint, nonlinearity in the output of an IVS is undesirable, and a variable nonlinearity is intolerable. Since the degree of nonlinearity was clearly a function of illumination level, some means of controlling that level was needed. One alternative was to reduce the illumination to the minimum value by means of an IRIS diaphragm or a variable neutral density filter. This approach, however, would force the IVS to perform under the worst possible conditions 100 percent of the time; and the nonlinearity, though it may be consistent, still remains. The other alternative, increasing the illumination level, required a light amplifying device, and a design change was implemented which included an image intensifier in the EPEM.

The success resulting from this change is evident from the results of the EPEM acceptance test performed on 3 December 1968. Sample recordings of one linearity test are shown in Fig. 3-9. As the input velocity was reduced, the recorder sensitivity was increased by the same factor. Therefore, perfect linearity would be indicated by all recordings having the same deflection. Fig. 3-10 is a plot of the data shown in Fig. 3-9. A straight line with a slope representing a gain factor of 15 volts per inch per second is also shown. The variation from this line is less than 10 percent.

All other tests, performed under different scene and illumination conditions, exhibit the same degree of linearity. The manner in which the gain factor varies is discussed in Section 3.2.

3.2 GAIN CONTROL

3.2.1 ETMA

The analysis of Section 2.1 indicated two possible means of controlling the gain of the sensor: (1) normalization with the average rectified video signal, and (2) the second harmonic. Both of these techniques were used in Engineering Test Model A (ETMA).

Fig. 3-11 is a schematic of the ETMA video amplifier. The output of the detector diodes, CR1, is amplified and filtered, and the resulting voltage is applied to the base of transistor Q3B. As this voltage is increased, Q3B draws more current from the collector of a transistor in the integrated circuit amplifier, WC1146T, thereby reducing the gain of the amplifier. This, in turn, reduces the output of the detector and the base voltage of Q3B. This approach has two major drawbacks. First, the removal of current from the integrated circuit amplifier introduces signal distortion at all but the lowest signal levels. Second, the high noise content of the video signal at low illumination levels severely limits the dynamic range of the AGC loop.

Normalization with the second harmonic signal is accomplished as shown in Fig. 3-12. The 30-hz, second harmonic signal is selected by a Q = 5 bandpass amplifier. The selected signal is then synchronously detected and the fullwave rectified output of the detector is filtered by a low-pass amplifier. A set point reference is also provided by this amplifier. The resulting dc output voltage is applied to the gate of an FET operating in its ohmic region as a voltage-controlled variable resistor. The drain to source resistance of the FET determines the feedback ratio, and consequently the gain, of the forward path amplifier. This loop tends to maintain the amplitude of the second harmonic constant.

The effectiveness of second harmonic AGC is limited by the following factors:

1. The long time constant required to effectively filter a fullwave rectified 30-hz signal to dc severely limits the capabilities of the system to respond to sudden changes in scene conditions.
2. The 30-hz frame rate of the TV camera introduces a 30-hz component in the video signal which is independent of scene information.
3. The amplitude of the 30-hz component, introduced by the modulation process, of the video signal varies with input image velocity.

Examination of Figs. 3-7 and 3-8 show that, while some gain control was accomplished, the results were inadequate. The only variable in the data shown is illumination level. When scene content and contrast are also changed, the output sensitivity varies from 3 volts per inch per second to 20 volts per inch per second.

3.2.2 EPEM

Gain control is accomplished in the EPEM sensor by controlling the vidicon illumination and normalizing the output with a portion of the average rectified video signal.

Vidicon illumination is controlled by varying the accelerating potential of the image intensifier. A block diagram of the control loop is shown in Fig. 3-13. The set point voltage is adjusted to

provide the maximum accelerating potential of 15 kilovolts with the minimum illumination on the input face of the intensifier. In the EPEM unit, this is set for 0.017 foot-candle in the interface image plane. An increase in input illumination causes the output of the vidicon to increase. After amplification and clamping, the video signal is applied to a low-pass filter, the output of which is a dc voltage indicative of the average illumination on the face of the vidicon. The increase in this signal causes the control voltage input of the high voltage power supply to decrease, which in turn decreases the accelerating potential of the intensifier and, therefore, the illumination on the vidicon. The high gain of the loop tends to maintain the vidicon illumination and video signal at a constant dc level. This process removes one of the input variables from the video signal, and greatly simplifies the remaining task of controlling the sensor gain under varying scene content and contrast conditions.

The approach used to accomplish this task has been outlined in Section 2.2.3 of this report. The experimental work discussed reveals that the average value of the rectified video voltage is proportional to the fundamental component with the exception that the average rectified video voltage varies from some dc level other than zero. This offset is the result of rectifying the signal produced by the fiber-optics faceplate of the vidicon. That is, when a uniform illumination is applied to the image intensifier, a hexagonal grid pattern is visible on the TV monitor. This pattern is stationary and therefore makes no contribution to the output velocity signal. Furthermore, the dc voltage that is produced by rectification of the resulting video signal is a constant as long as the average illumination on the face of the vidicon and the gain of the circuitry prior to rectification remain constant. Since both of these conditions are satisfied in the EPEM sensor, the unwanted signal is easily removed.

The portion of the rectified video voltage that remains is filtered to separate the 15-hz and dc components. The 15-hz component is then divided by the dc component producing a 15-hz signal whose magnitude is proportional to input velocity and relatively independent of input scene conditions.

Figs. 3-14 and 3-15 contain typical samples of the actual data recorded during the acceptance test of the EPEM unit. The sensor output signal for a constant input velocity is shown as a function of the input scene conditions listed in the tables. The New Haven and Lancaster scenes referred to in the figures contain different amounts of information, one being a view of a heavily built-up city and the other consisting largely of open farm land. The data shown in the charts represent approximately 7 percent of the total recorded in testing both axes. Examination of all the data yields the following results:

1. For the New Haven scene, 97 percent of the data taken with contrast ratios above 1.027:1 were within the ± 25 percent tolerance specified by EC701A, revision 6.
2. For the Lancaster scene, 68 percent of the data taken with contrast ratios above 1.08:1 were within the tolerance.
3. For the extremely low contrast levels, although the sensor output did not conform to specification, a usable signal was obtained.

3.3 BIAS

The general problem of sensor bias and the sensor parameters that affect it have been discussed in Section 2.2.1 of this report. The sensor configuration with regard to those parameters and the bias test results for the ETMA and EPEM units are summarized here.

3.3.1 ETMA

The ETMA sensor divided the vidicon raster on a line basis. The output demodulator was set for maximum sensitivity, i.e., in phase with the 15-hz signal at a high input velocity; 67 percent of the bias data obtained during the ETMA acceptance test were less than 0.010 inch per second per axis. The bias was less than 0.020 inch per second per axis 87 percent of the time.

3.3.2 EPEM

The EPEM sensor split the raster on a field basis. An alignment current adjustment was included to minimize the systematic bias. The output demodulator was set for minimum random bias, i.e., in quadrature with the zero velocity signal. During the EPEM acceptance test, the bias was never greater than 0.004 inch per second per axis, and was equal to or less than 0.001 inch per second per axis 75 percent of the time. Some samples of the bias data are shown in Fig. 3-16.

3.4 OUTPUT NOISE

In the ETMA, the gain to the 15-hz signal is provided prior to the selection of that signal from rectified video. Consequently, in order to avoid amplifier saturation, it is necessary to reject the 60- and 120-hz components of the rectified video signal, which are larger than the 15-hz components.

In the EPEM, the 15-hz signal is selected before it is amplified, and the Q = 5 filter does most of the filtering. Some 30-hz signal gets through, however, which when demodulated by 15-hz signal would produce a 15-hz output. Therefore, the 30-hz signal is selected, inverted and added back into the total signal, thereby eliminating the 30-hz component.

The demodulation of the 15-hz signal produces a 30-hz component at the sensor output which is sizable even after filtering. Therefore, the signal selection, inversion, and summation process is also performed at the output—considerably improving the sensor signal-to-noise ratio.

3.5 RELAY OPTICS

Both the ETMA and the EPEM utilize a relay system to re-image the aerial interface image on either a vidicon or intensifier. A commercial Wollensak 35-mm f/2 lens in conjunction with a custom designed field lens and field flattener is used in the ETMA design (see Fig. 3-17). The EPEM used all Itek designed elements (see Fig. 3-18).

An additional difference between ETMA and EPEM is the use of an "on-axis" and an "off-axis" prism in ETMA and a beam split "on-axis" prism in EPEM.

The MTF of the relay optics is considerably greater in EPEM because of specific application design. Fig. 3-19 shows the relative MTF for the two units. The EPEM design provides a higher signal-to-noise ratio for the stimulus material at the intensifier photocathode.

Another significant difference between EPEM and ETMA is the transmission of the relay optics. Transmission is 60 percent for ETMA and 85 percent for EPEM. It should be noted that the 85 percent does not include the beam splitter which provides approximately a 30-30 split.

3.6 UTILIZATION OF INTERFACE IMAGE (OFF-AXIS RATES, CROSS COUPLING)

It is required that the sensor indicate the center of format velocity which is the only point in the format indicative of the net vector tracking rate error. If one considers a coordinate system

which is aligned with the direction of displacement of a point resulting from tracking mirror pitch and roll, then the following is true. Cross-track velocity at any point on the along-track (or pitch) axis is equal to cross-track velocity at the center of format. Along-track velocity, however, can only be sensed at the center of format. (See Fig. 3-20.)

This fact makes it possible to locate the cross-track patch off axis providing the center of the patch is on the along-track axis. The center of the along-track patch must be at the center of format. Utilization of this approach requires rotation of the sensor to compensate for rotation of the along- and cross-track axes with tracking mirror roll.

In order to avoid the light loss that accompanies the use of a beam splitter, which is required to sense the velocity in both directions at the center of format, the offset patch approach was incorporated into ETMA.

The above approach is valid only if the sensor does not respond to velocities perpendicular to the direction of modulation and scan. While this is true in general, a scene which contains a significant amount of diagonal information does induce a cross-coupling output. This effect is immediately obvious if one considers a scene made up entirely of lines at 45 degrees to the direction of interest. Fig. 3-21 illustrates such a situation. The situation of Fig. 3-21(b) can be reached from that of Fig. 3-21(a) by moving the lines either down or to the right, or any combination of the two. If the view is limited by the rectangles, it is impossible to tell which of the three possibilities is actually occurring.

With the cross-track patch located off axis, an along-track velocity is present even when the center of format is being perfectly tracked, and it is possible for the tracking to be upset by the cross-coupling phenomenon.

When the image intensifier was incorporated into the EPEM unit, illumination was no longer a critical matter, and a beam splitter was also included so that both patches could be located at the center of format. Accordingly, once perfect tracking has been achieved, tracking cannot be disturbed. In addition, the roll capability was no longer required and was eliminated with a considerable saving of weight, power, and complexity.

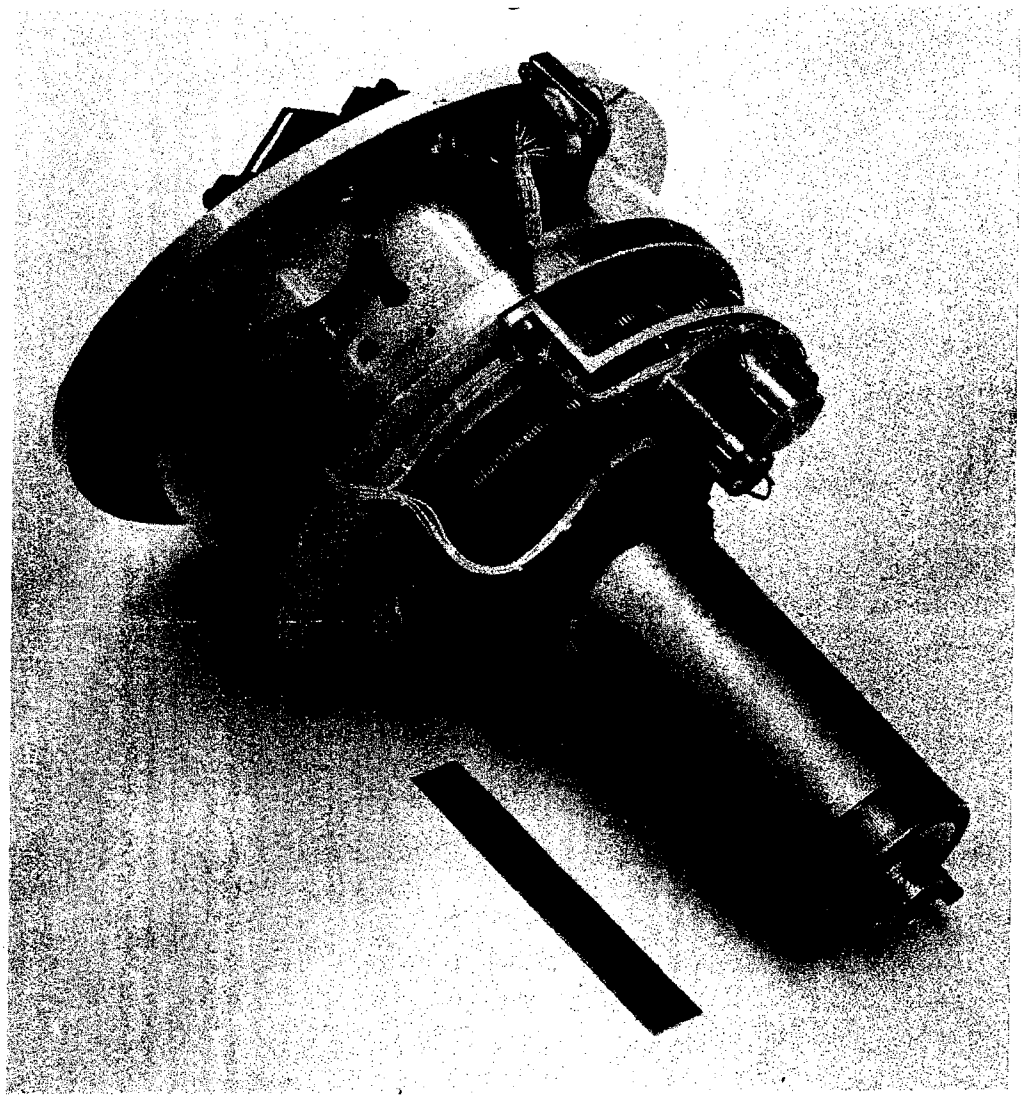

Fig. 3-1 — Engineering test model A

BIF-059-4035-69

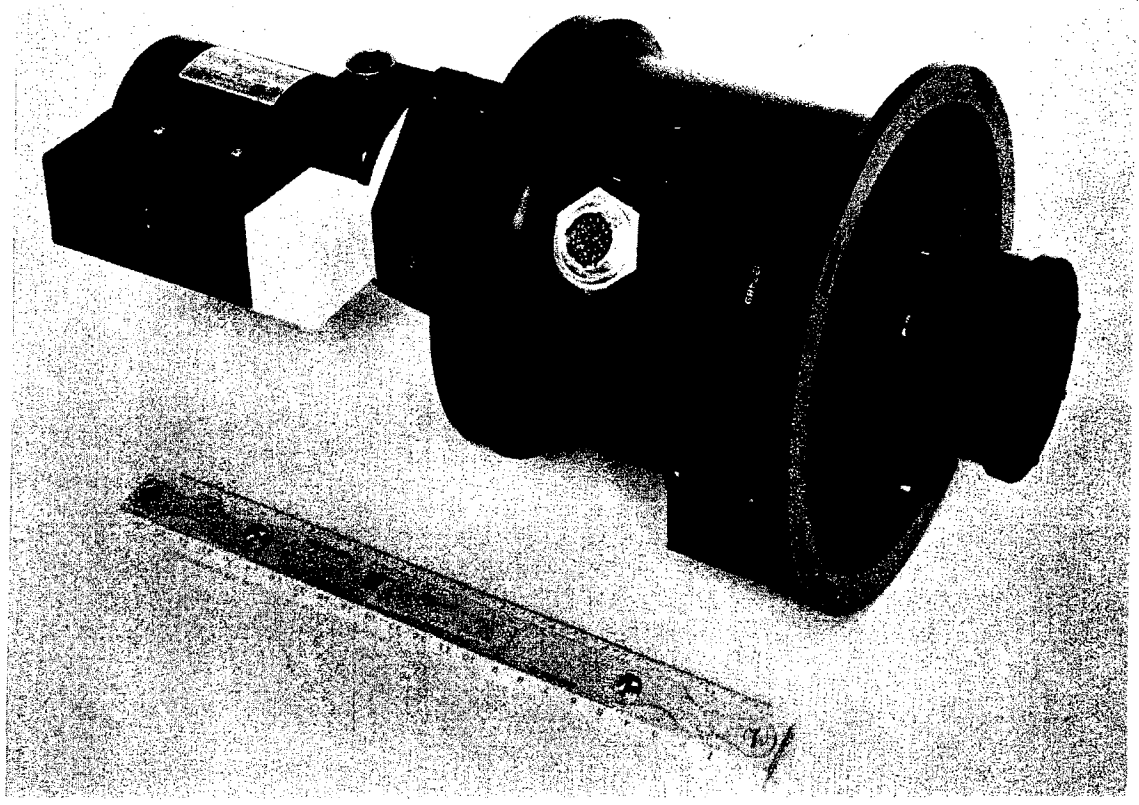

Fig. 3-2 — EPEM sensor head

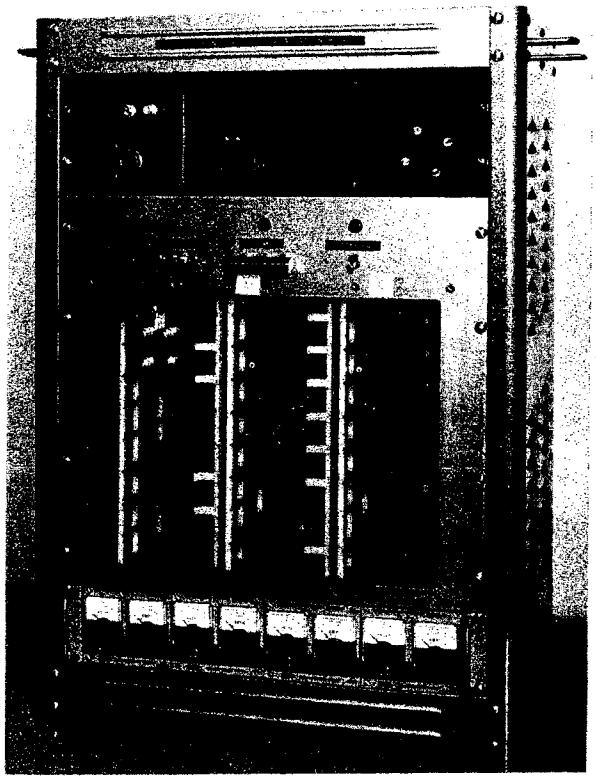

Fig. 3-3 — EPEM electronics rack

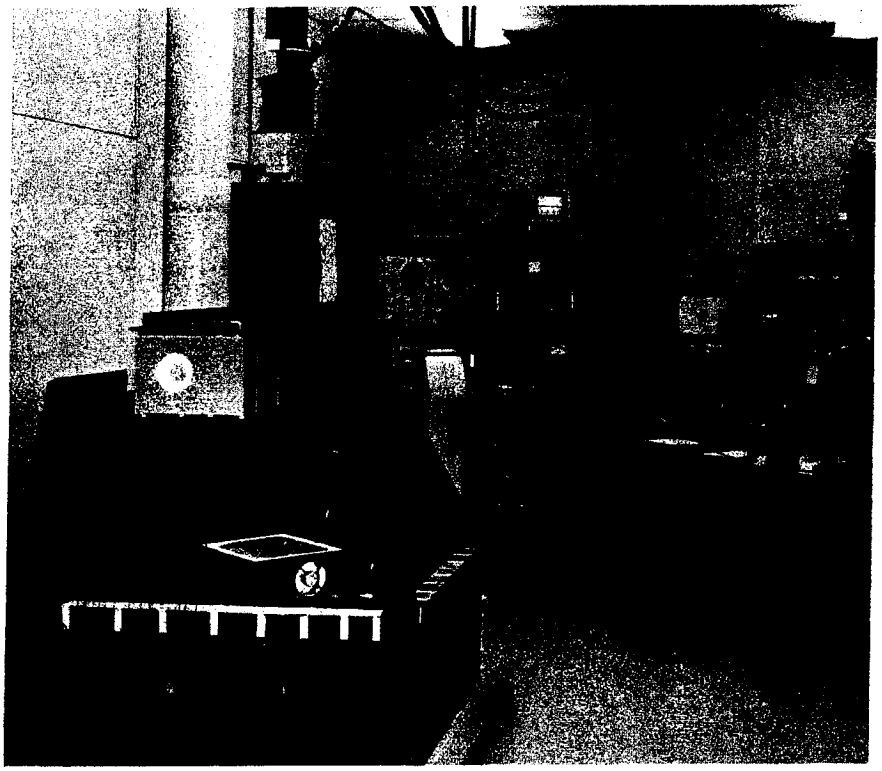

Fig. 3-4 — ETMA test setup

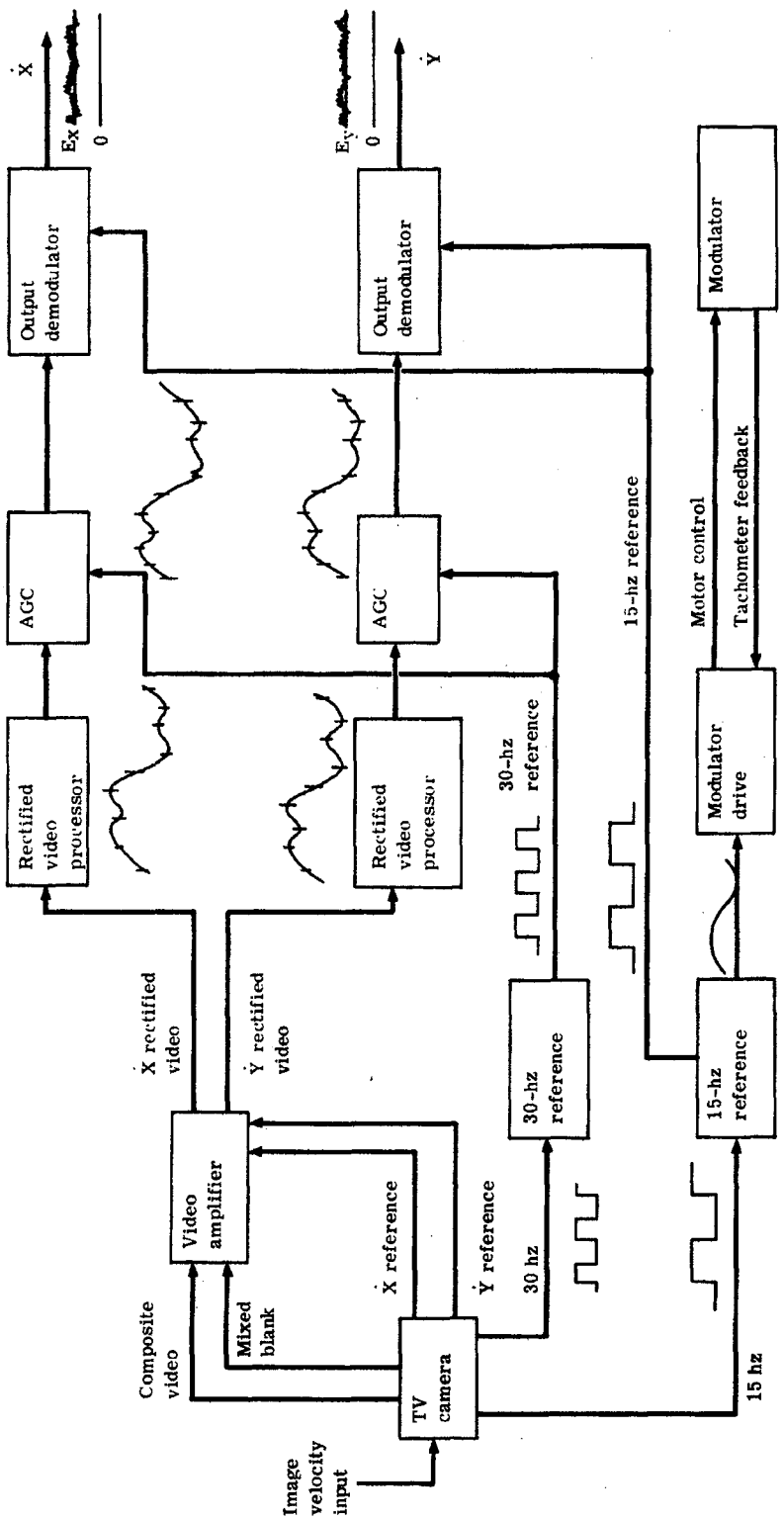

Fig. 3-5 — ETMA block diagram

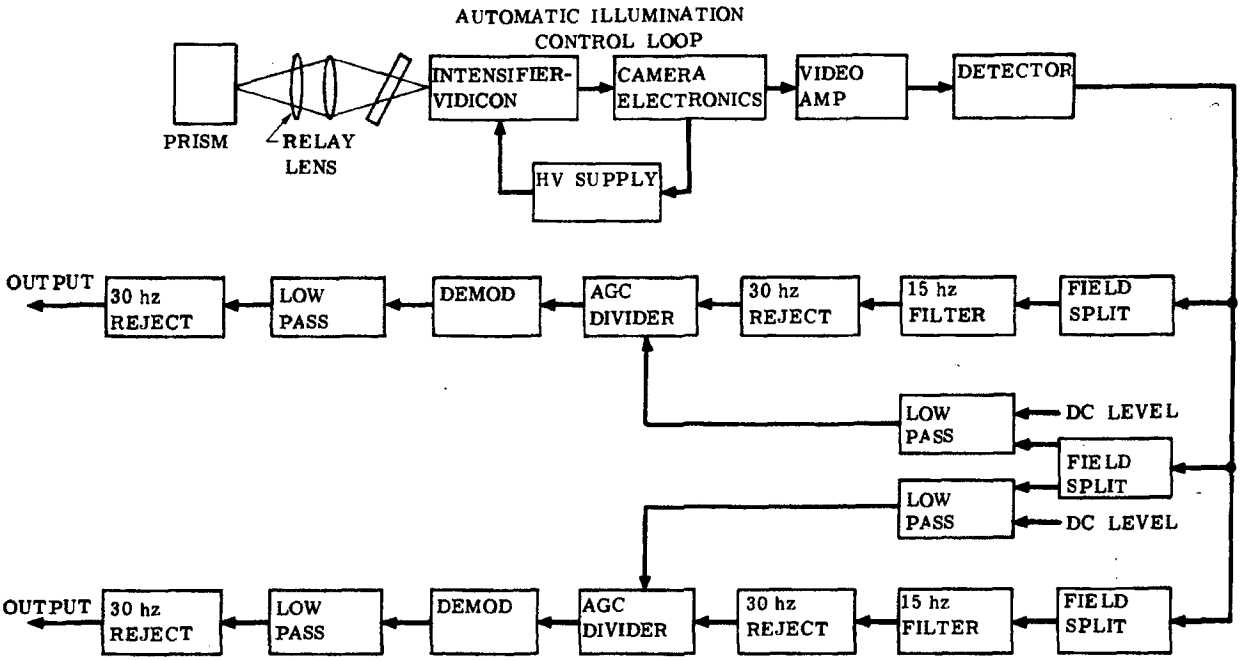

Fig. 3-6 — EPEM block diagram

Table 3-1 — Major Differences Between ETMA and EPEM

Engineering Test Model December 1967	Engineering Prototype Evaluation Model December 1968
Vidicon	Image-intensifier-vidicon
Line-split	Field-split
Offset patch	Central patches
Commercial lens	Itek-designed lens
Second harmonic AGC	AGC with average rectified video and illumination control
60-hz reject prior to demodulation	30-hz reject prior to demodulation
Demodulation in phase with high velocity signal	Demodulation 90 degrees out of phase with zero velocity signal
	Alignment current to remove remaining bias
	Rejection of 30 hz at output

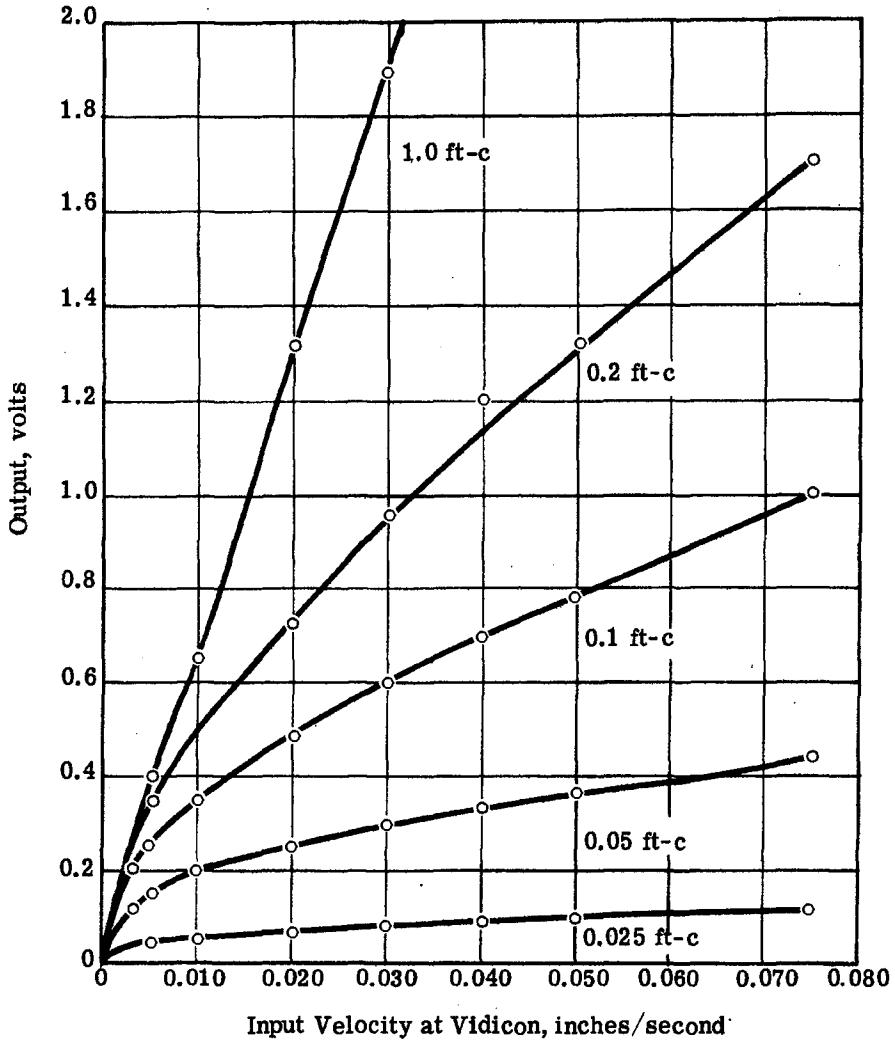

Fig. 3-7 — ETMA linearity as a function of vidicon illumination, without AGC

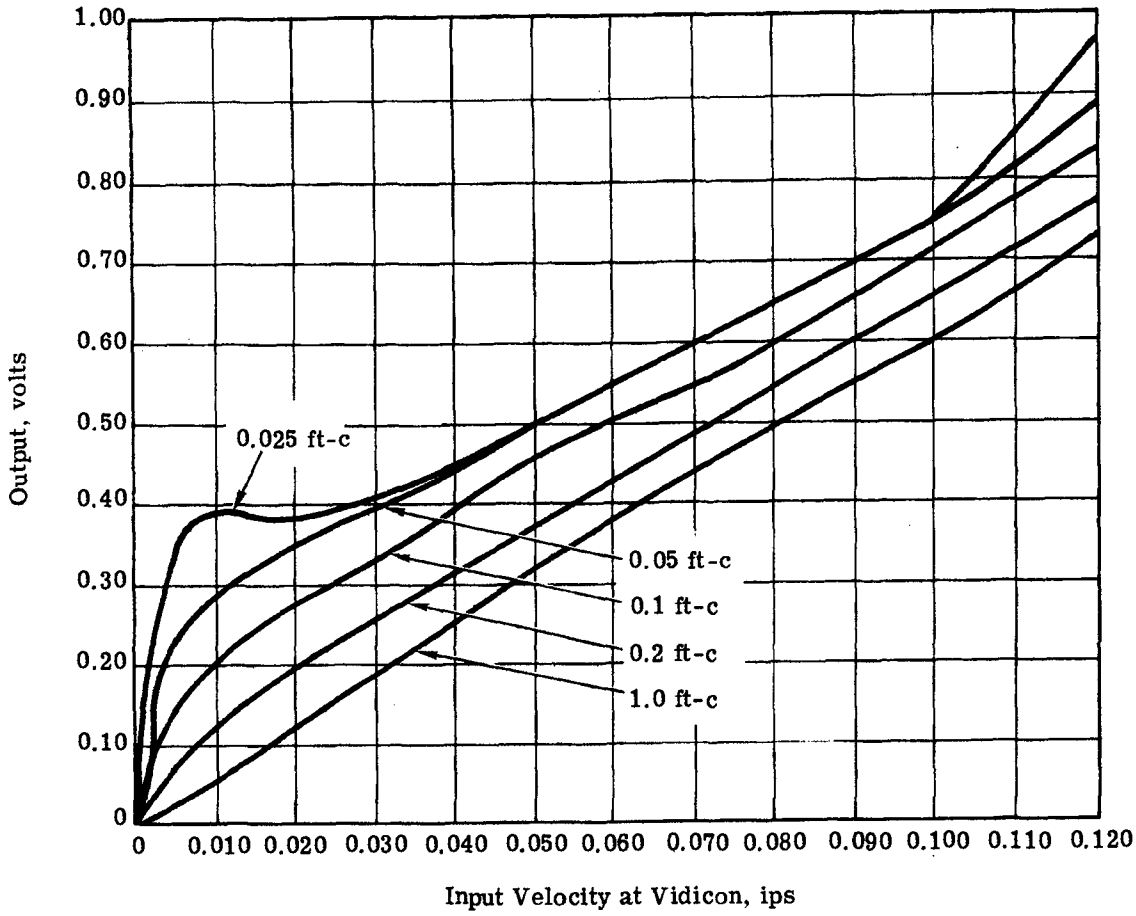

Fig. 3-8 — ETMA linearity as a function of vidicon illumination, with AGC

BIF-059-4035-69

New Haven scene
Illumination from scene = 0.19 ft-c
Illumination from haze = 0.27 ft-c
Contrast = 2.55/1

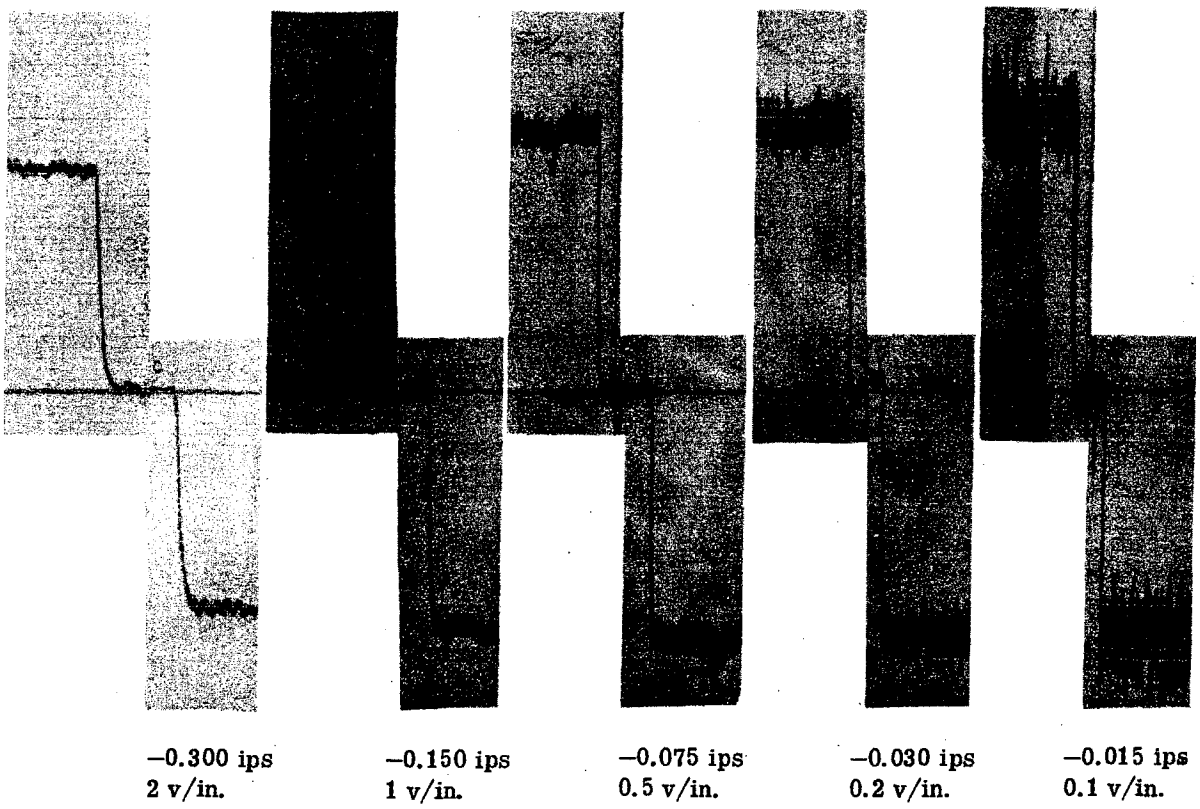

Fig. 3-9 — EPEM linearity test recordings, with image intensifier

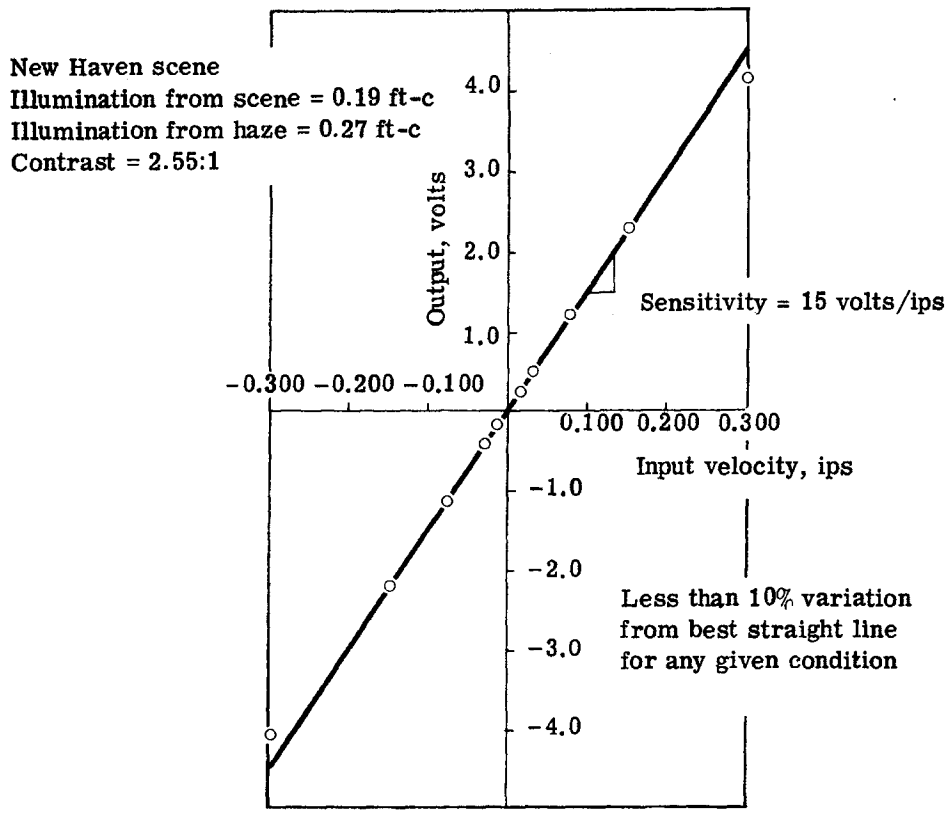

Fig. 3-10 — Linearity data plotted from EPEM test recordings, with image intensifier

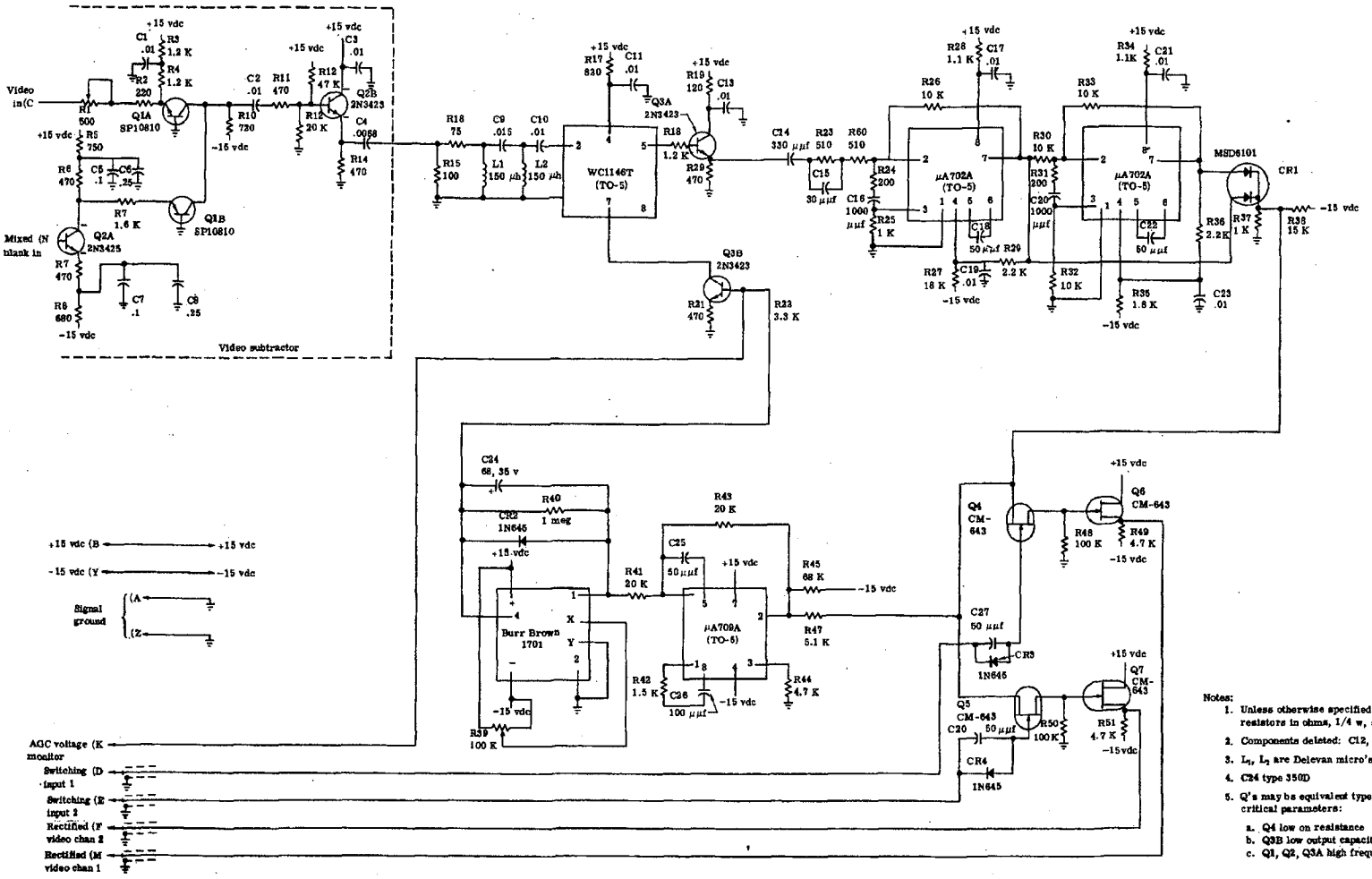

Fig. 3-11 — ETMA video amplifier

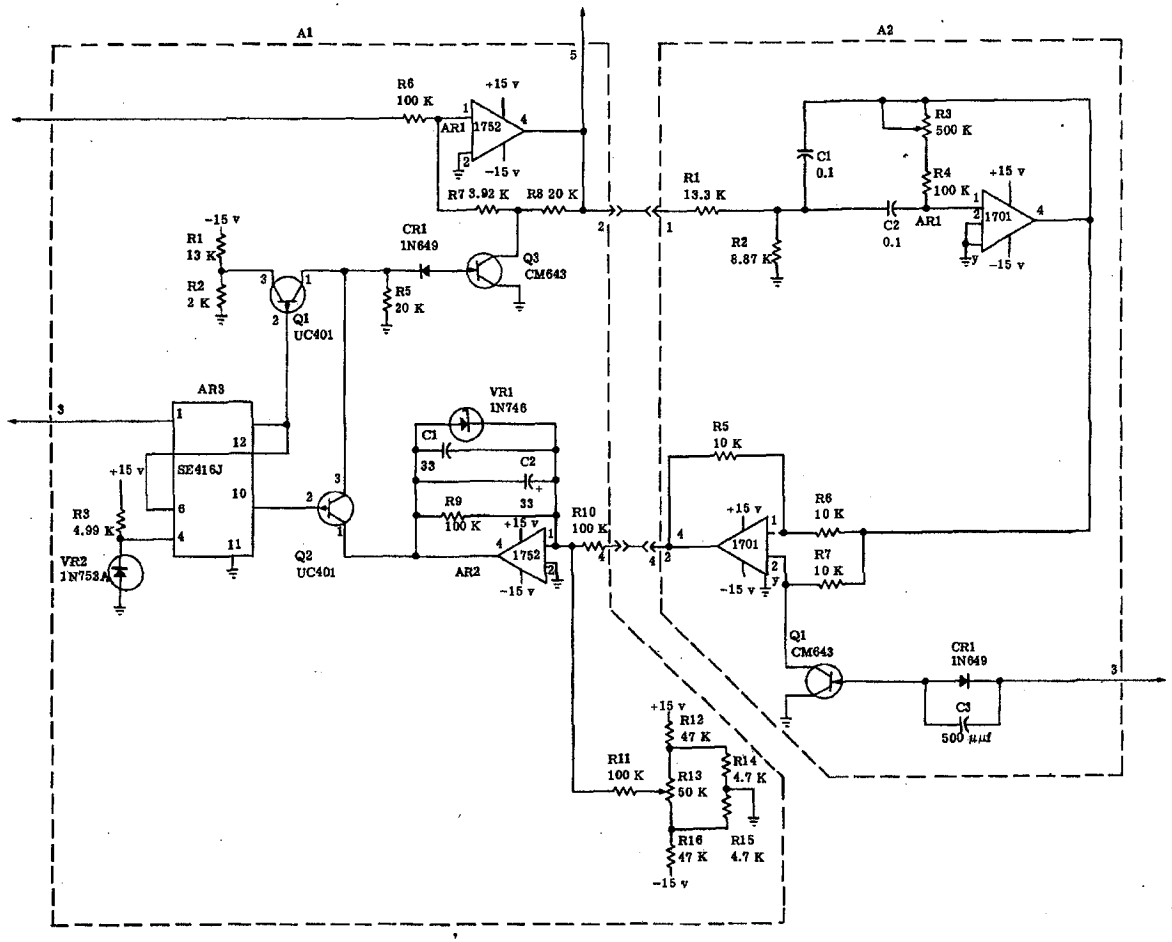

Fig. 3-12 — AGC amplifier

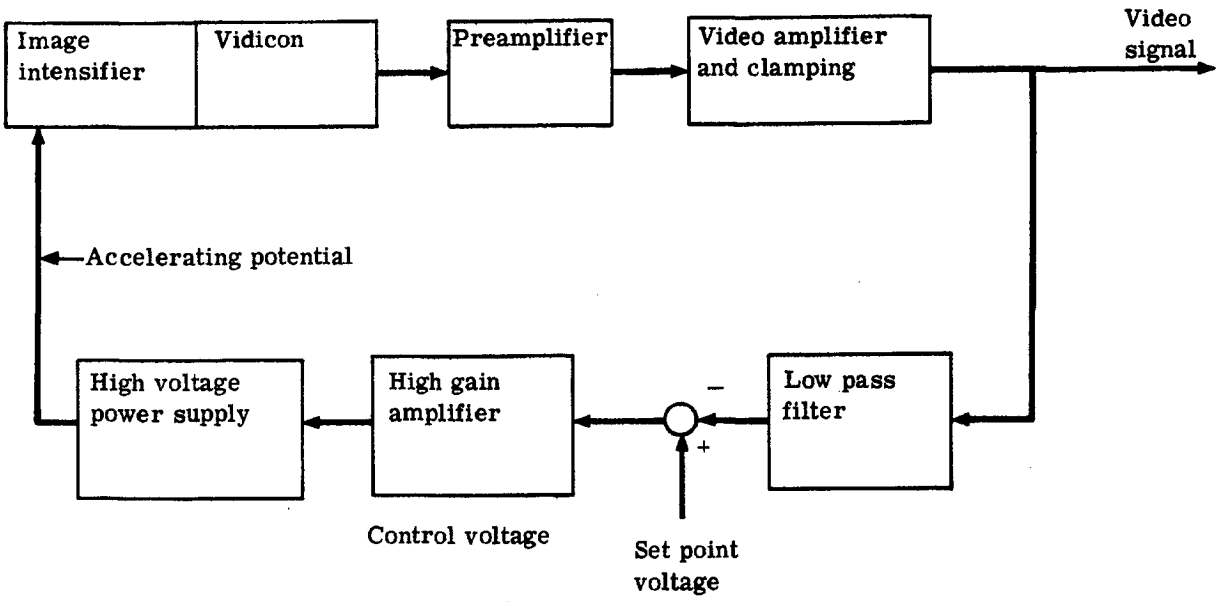

Fig. 3-13 — Automatic illumination control block diagram

Scene illumination, ft-c	0.241	0.189	0.189	0.189	0.030	0.030	0.030	0.030	0.030	0.006	0.006	0.006	0.006	0.006	0.006
Haze illumination, ft-c	0.540	0.540	0.271	0.027	0.540	0.427	0.171	0.086	0.009	0.540	0.427	0.214	0.107	0.043	0.017
Total illumination, ft-c	0.781	0.729	0.460	0.216	0.570	0.457	0.201	0.116	0.039	0.546	0.433	0.220	0.113	0.049	0.023
Contrast ratio	1.81	1.64	2.55	8.90	1.10	1.13	1.33	1.64	5.87	1.02	1.027	1.05	1.11	1.26	1.65

New Haven scene
Image velocity = 0.120 ips

Fig. 3-14 — EPEM test results—x-axis gain factor

Scene illumination, ft-c	0.185	0.185	0.185	0.115	0.115	0.115	0.019	0.019	0.019	0.019	0.019	0.019
Haze illumination, ft-c	0.540	0.214	0.017	0.540	0.271	0.086	0.540	0.427	0.171	0.086	0.021	0
Total illumination, ft-c	0.725	0.399	0.202	0.655	0.386	0.201	0.559	0.446	0.190	0.105	0.040	0.019
Contrast ratio	1.63	2.50	10.9	1.40	1.77	3.24	1.06	1.08	1.21	1.41	2.57	20

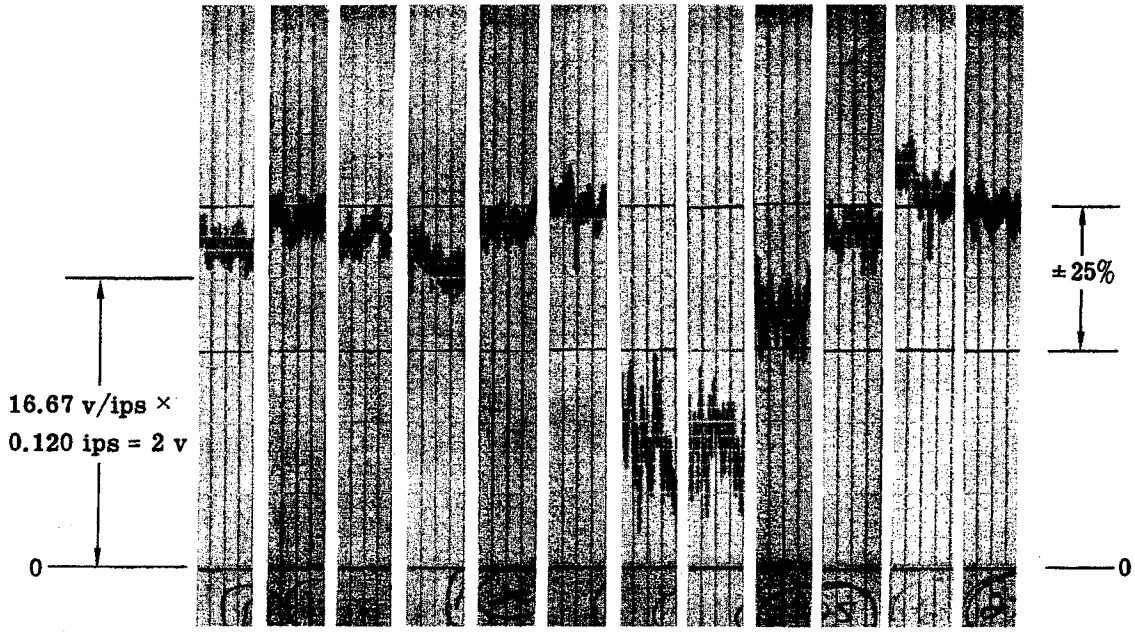

Lancaster scene
Image velocity = 0.120 ips

Fig. 3-15 — EPEM test results—y-axis gain factor

Input velocity = ± 0.015 ips
Recorder sensitivity = 0.1 volt/inch

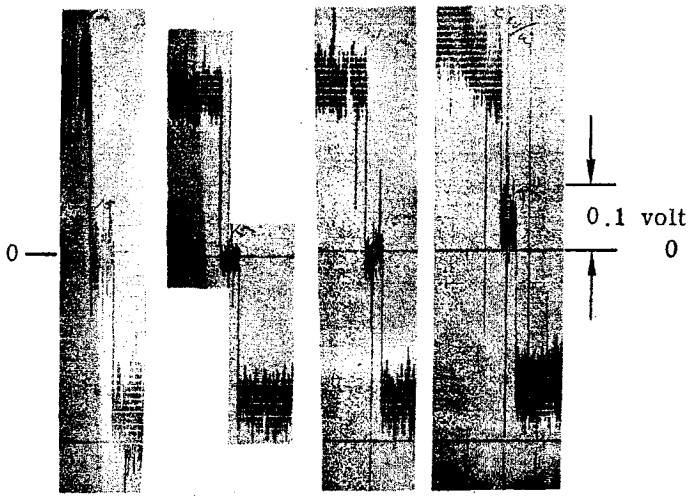

New Haven scene

X Axis	X Axis	X Axis	Y Axis
0.781 ft-c	0.271 ft-c	0.023 ft-c	0.023 ft-c
1.81:1	2.55:1	1.65:1	1.65:1

Bias for all scenes 100% ≤ 0.004 ips
75% ≤ 0.001 ips

Fig. 3-16 — EPEM test results—bias

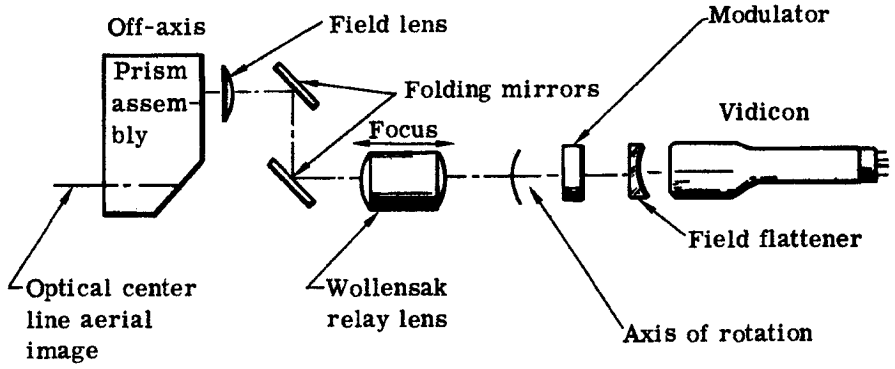

Fig. 3-17 — ETMA optical schematic

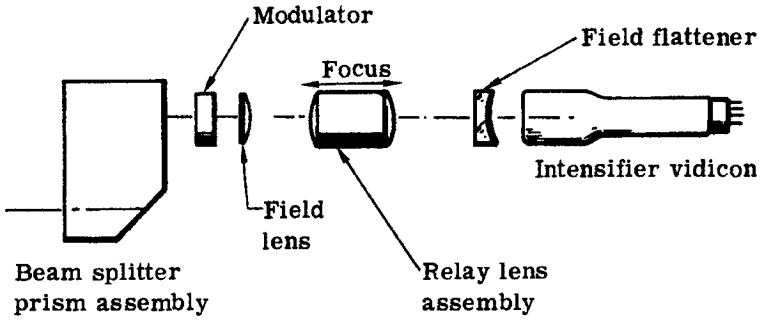

Fig. 3-18 — EPEM optical schematic

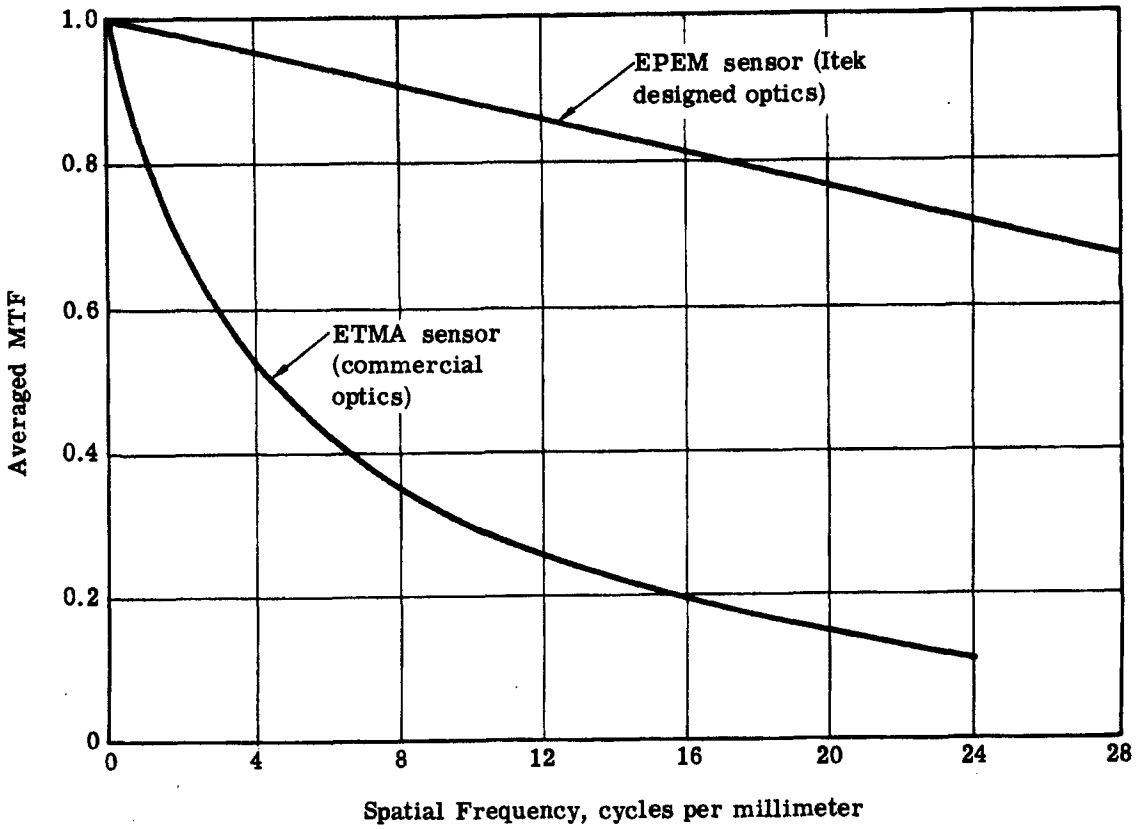

Fig. 3-19 — Relative MTF's of EPEM and ETMA

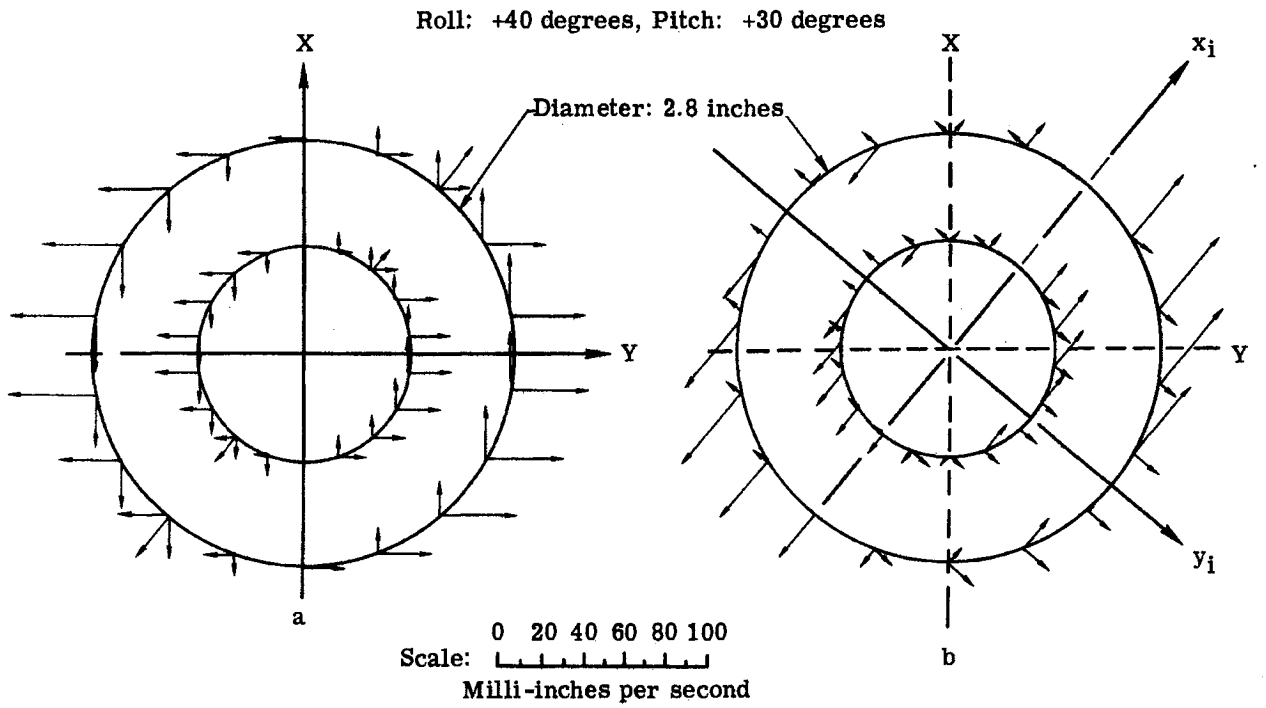

Fig. 3-20 — Off-axis image plane velocity for perfect tracking

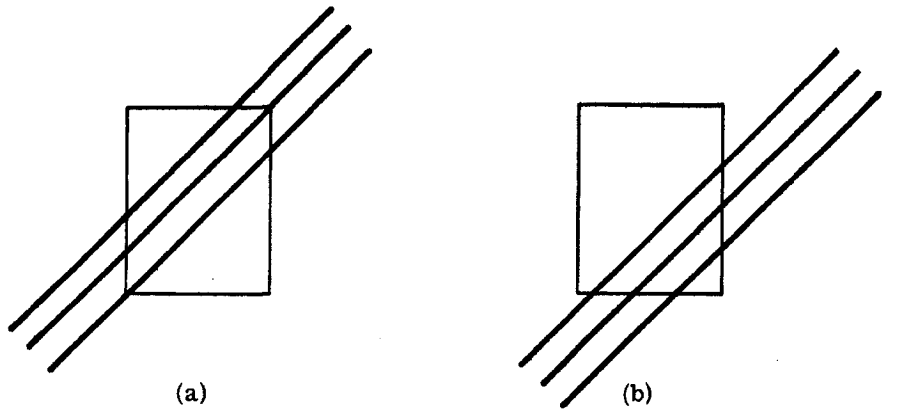

Fig. 3-21 — Cross-coupling effect

4. PICTUREPHONE CAMERA

4.1 DESCRIPTION

As previously indicated, the use of an image intensifier in the sensor was largely dictated by the need for linearity versus image velocity in the output signal. At the required low operating illuminations, the 8567 vidicon, which uses an Sb_2S_3 photoconductive layer, performed nonlinearly due to the large photoconductive lag. The intensifier solved this problem at the expense of added volume, weight, power, complexity, and the attendant necessity for a high voltage power supply. It would be desirable to solve the problem simply by using a vidicon which does not have the problem at low illuminations. Such a device, called the "Picturephone tube," has recently been developed by Bell Telephone. Texas Instruments has also developed essentially the same tube which uses an array of photodiodes instead of a photoconductive surface. The advantages cited for this tube are:

1. No image persistence due to photoconductive lag
2. Higher sensitivity
3. Wider spectral response, including sensitivity to a near IR gamma of unity
4. Low dark current
5. Longer life.

These advantages appeared satisfactory, and a Picturephone tube was acquired from Bell Laboratories, Whippany, New Jersey; also, a modified GPL 1000 camera was purchased from General Precision Laboratories. This was the same type camera used with the Picturephone tube at Bell Laboratories. This camera has the capability of being operated at 60 frames and 120 fields per second, as well as the conventional 30 frames and 60 fields per second.

4.2 EXPERIMENTAL RESULTS

Due to the lack of an image splitting prism and relay lens, the initial tests could not directly compare the IV and the Picturephone tube on the simulator. However, the tests so far using a Picturephone tube in a sensor have shown the following:

1. The sensor operates well at the lowest required illumination.
2. The output is linear with velocity at this illumination.
3. The bias is acceptable.

Fig. 4-1 shows the sensor output at three different velocities on the same scene. The tests were run with an illumination at the Picturephone tube of 0.023 foot-candle. The sensor gradients at ± 0.031, 0.065, and 0.130 inch per second on the Picturephone tube were 55, 51, and 48 volts per inch per second, respectively. Fig. 4-2 shows the same test at ± 0.007 inch per second on the Picturephone tube, indicating that the bias is low. Fig. 4-3 is a test at ±0.0033-inch-per-second image velocity at the Picturephone tube of less than 0.02 foot-candle illumination.

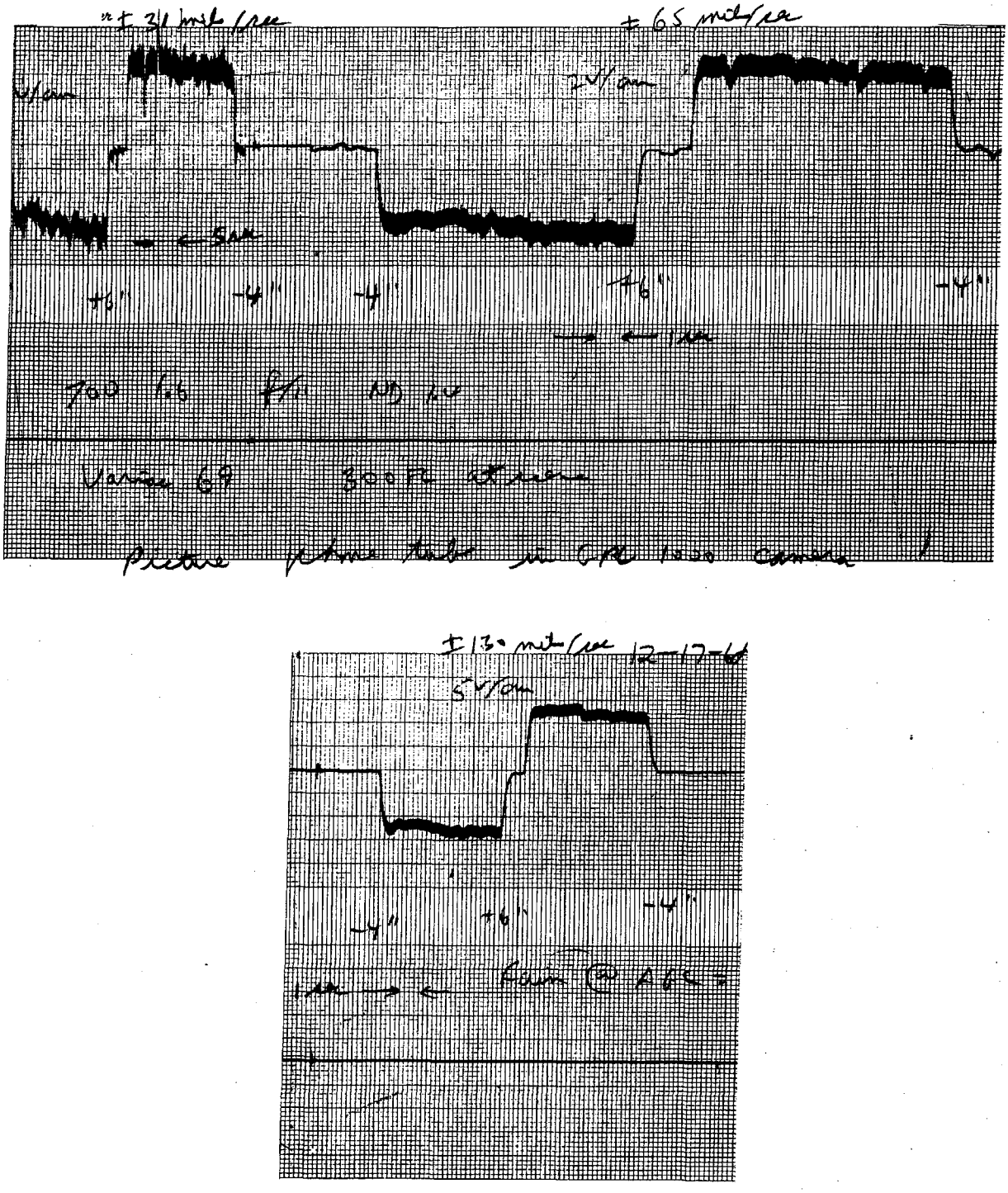

Fig. 4-1 — Sensor output at ±0.031, 0.065, and 0.130-inch-per-second image velocity

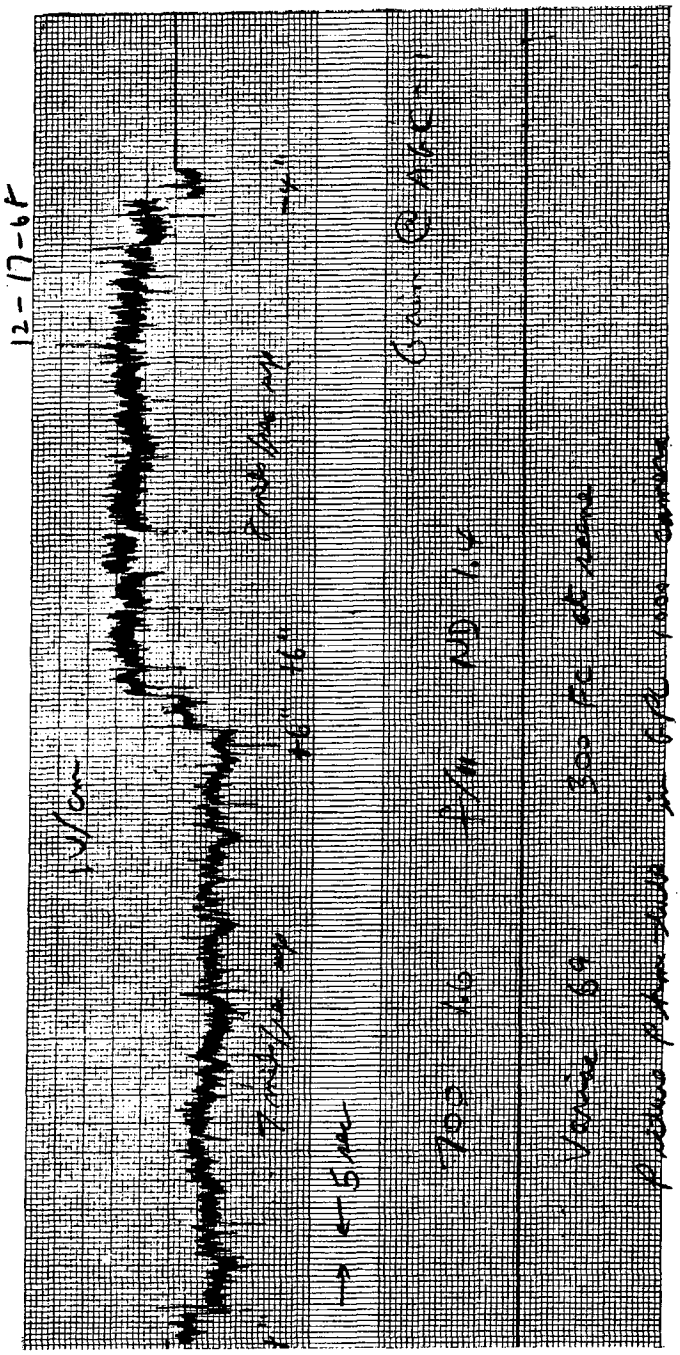

Fig. 4-2 — Sensor output at ± 0.007-inch-per-second image velocity indicating low bias

BIF-059-4035-69

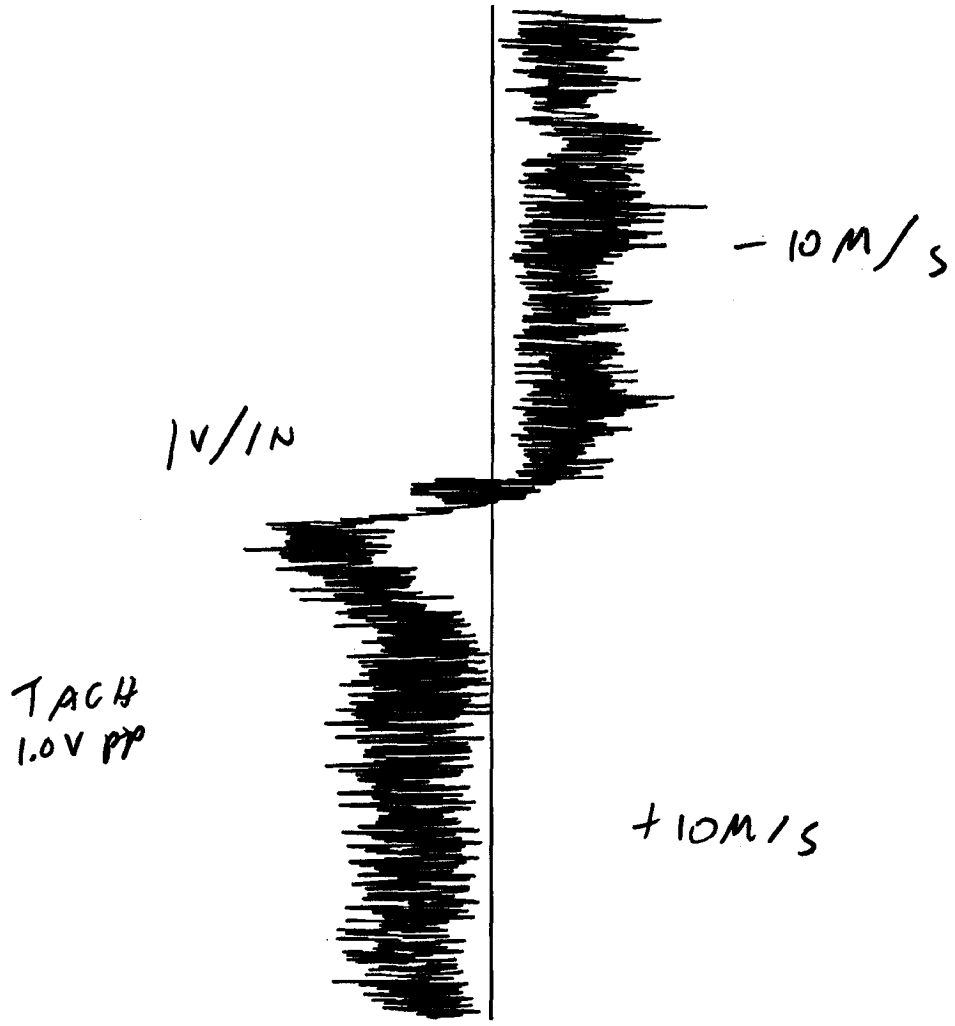

Fig. 4-3 — Sensor output at ±0.0033-inch-per-second image velocity

5. LOW LIGHT LEVEL CAMERAS

5.1 STUDIES

A study was conducted on TV camera tubes for low light level IVS operation. This study was summarized in Itek document no. 9415-67-173 dated 15 November 1967.

Various tube types such as lead oxide and antimony trisulfide vidicons were evaluated. The gain to be effected by use of image intensifiers with these devices was also determined.

The IVS mathematical model has indicated that the TV camera tube should exhibit low discharge lag and good integration and storage for maximum performance. The SEC vidicon exhibits all of these characteristics; however, its membrane target element raises questions regarding ruggedness. In addition, as it is a relatively new device, very few camera designs exist and insufficient data and history are available with regard to reliability. A short test gave inconclusive results which indicated possible operational problems when viewing low contrast scenes. That is, the modulation created by internal screens or grids may be greater than the modulation in the image.

The PbO vidicon (plumbicon) promised low discharge lag, low dark current, slightly higher sensitivity, and a gamma of unity. These characteristics suggested considerable improvement in performance when compared with an Sb_2S_3 vidicon such as the 8567. For this reason, an industrial plumbicon camera was obtained from the Amperex Corporation and subjected to several days of evaluation. Considerable improvement in subjective picture quality was observed on the monitor. However, its performance in the IVS was similar to that obtained with the 8567 tube. That is, the predicted improvement did not materialize. This can be attributed to the short storage time of the plumbicon. As this attenuates the smear effects, the IVS sensitivity is reduced.

Thus, it was concluded that the Sb_2S_3 vidicon offered the best alternative at this time.

In order to extend the illumination range of the 8567 vidicon, image intensifiers were investigated. It was concluded that a single stage, 25-millimeter, in and out image intensifier would provide the performance required.

5.2 ITEK INTENSIFIER VIDICON (IV) CAMERA DEVELOPMENT

An Itek intensifier vidicon camera system has been designed and developed. Fig. 5-1 shows the intensifier vidicon system schematic. The camera is packaged into two units consisting of a camera head and an electronic control box. The camera head consists of the housing, IV, preamplifier, and horizontal and vertical deflection circuits. The remainder of the camera electronics are contained in the electronics box. Where possible, integrated circuits are used to decrease the size and power consumption of the camera system. Several power supply configurations were designed to eliminate the series regulator but were not incorporated in the camera due to extreme ripple problems. High voltage and failsafe circuits are shown in Fig. 5-2.

5.2.1 Specifications

The design specifications of the IV camera are as follows:

1. Capability to function on a dc input supply voltage of 22 to 31 volts
2. Standard of 525 lines per frame; positive 2:1 interface; 30 frames per second, 60 fields per second
3. Horizontal resolution limited by IV response is 500 TV lines at center of format at highest light level
4. A 25-millimeter (1:1) intensifier mated to an 8567 vidicon with fiber optics in and out
5. A 7-mhz video bandwidth to accommodate 500 TV lines center resolution
6. Scan linearity within 1 percent of best fit straight line
7. DC restoration of clamping is keyed and adjustable
8. Crystal controlled sync generation from a master oscillator
9. No aperture connection or automatic target control
10. The IV is capable of operating at a light level of 5×10^{-3} foot-candle at the intensifier photocathode.

5.2.2 Circuit Description

Horizontal Deflection Circuit

The horizontal deflection circuit (Fig. 5-3) was designed as a positive feedback current integrator with the deflection yoke as the integrating element. It is also a ringing type of deflection circuit to decrease the power consumption. The linearity and size of the deflection current is adjustable as well as the position of the raster.

Vertical Deflection Circuit

The vertical deflection circuit (Fig. 5-4) consists of a positive feedback voltage ramp generator driving a negative current feedback power amplifier. The ramp generator is similar to a boatstrap integrator with loop gain equal to one. The amplitude, linearity and postion of the deflection circuit is adjustable.

Maximum use of integrated circuits is used in each of these circuits, where applicable.

Power Supply

The power supply is a dc to dc converter with input regulation only. The converter is driven at the half frequency of the horizontal line frequency so that switching transients of the converter occur during the vidicon blanking time.

When power is switched, the converter is driven from a relaxation oscillator to obtain the necessary output voltages to start the sync generator. Then the sync generator horizontal drive pulses are fed back to sync the power supply to half frequency of the horizontal time rate. This eliminates any RFI time switching transients (conducted or radiated) from being introduced into the video signal.

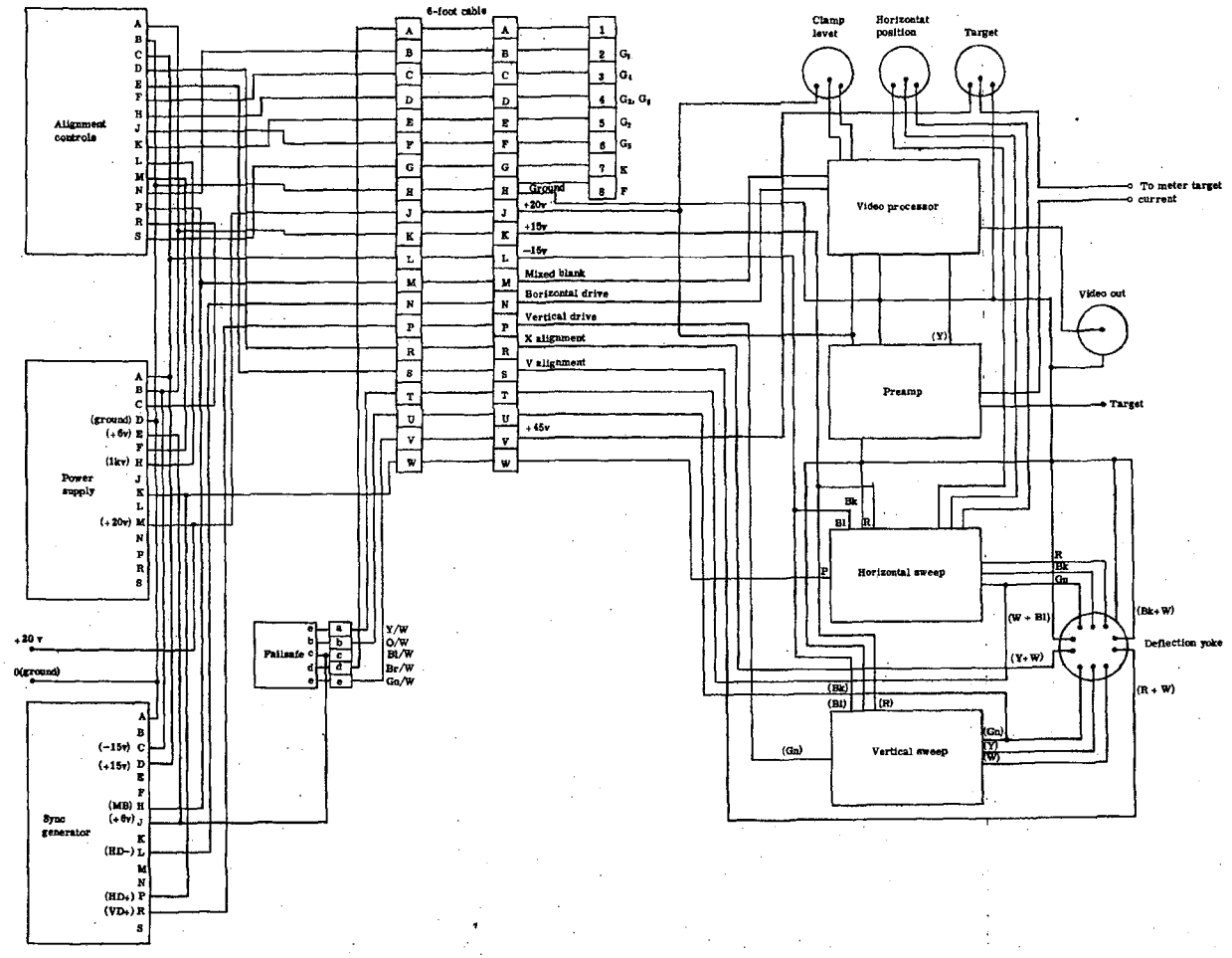

Fig. 5-1 — Intensifier vidicon system schematic

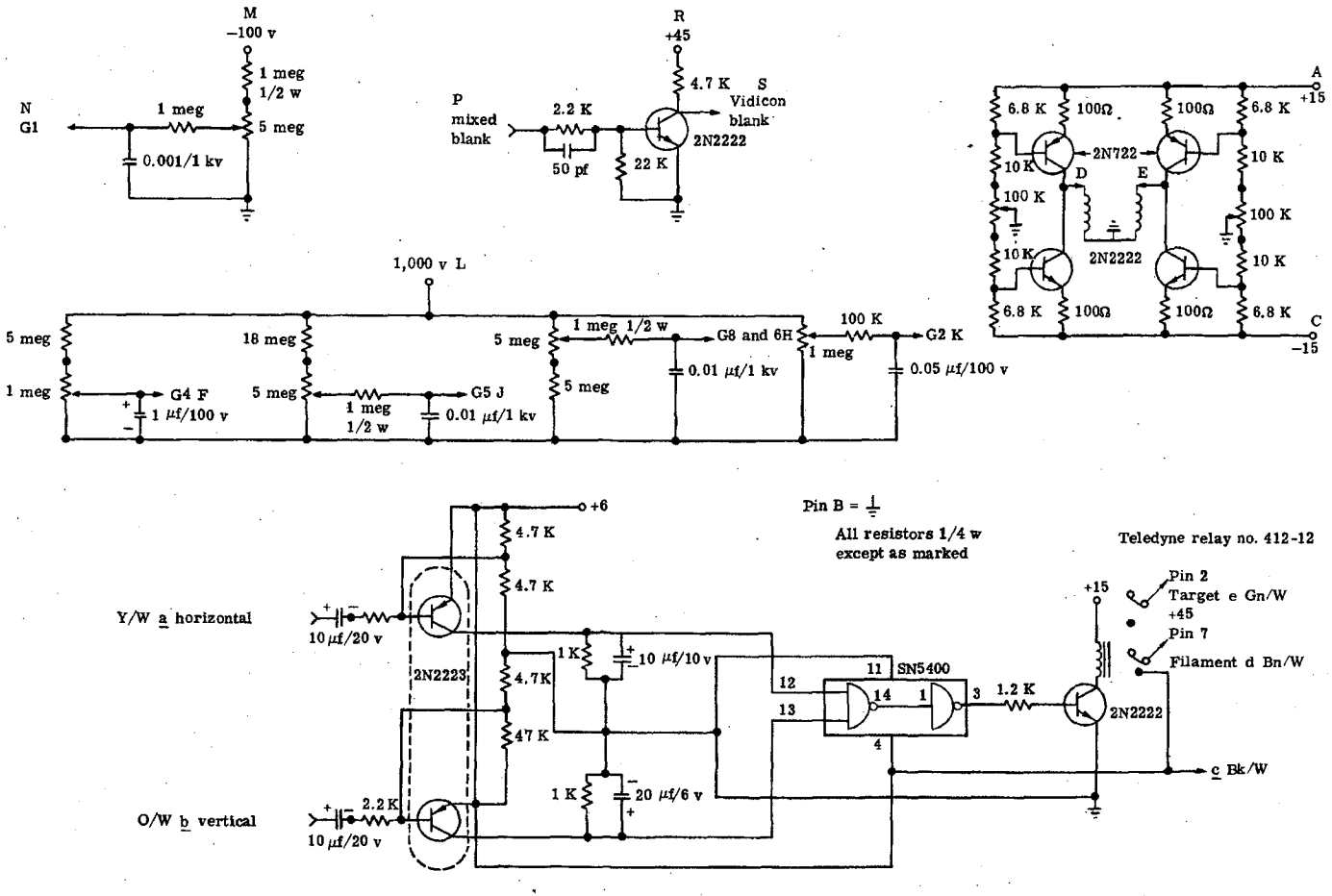

Fig. 5-2 — High voltage and failsafe circuits

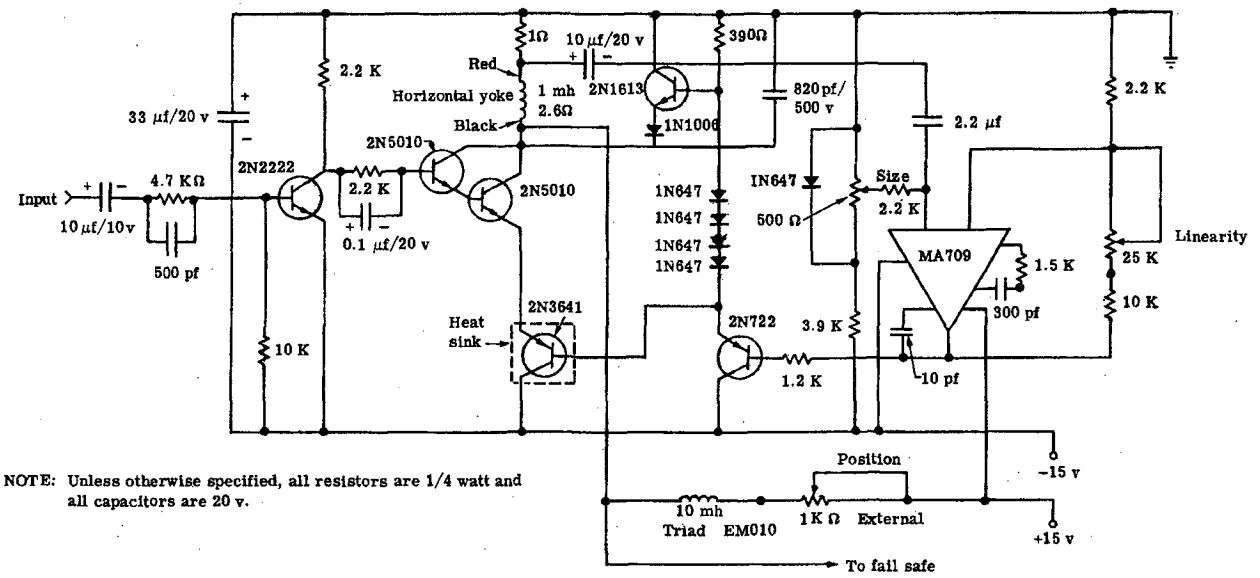

NOTE: Unless otherwise specified, all resistors are 1/4 watt and all capacitors are 20 v.

Fig. 5-3 — Horizontal deflection circuit

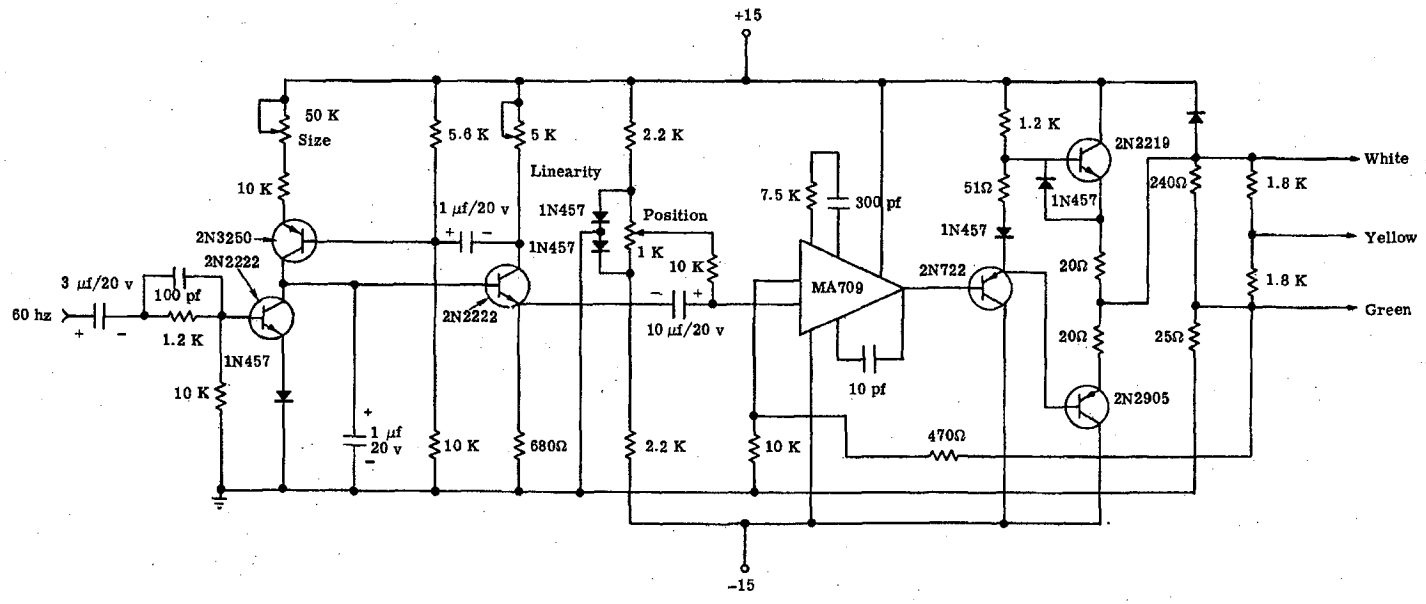

Fig. 5-4 — Vertical deflection circuit

Time Base Generator (Sync)

The sync generator is controlled by a crystal oscillator. The outputs of the generator are the horizontal and vertical drive pulses and blanking pulses, mixed blanking pulses, and mixed drive pulses (mixed sync). The generator is designed with integrated circuits and all timing signals are solely dependent on the crystal clock; no one-shots or delay lines are used. The output is capable of driving heavy loads and the logic level is 6 volts.

Preamplifier

A low noise preamplifier (Fig. 5-5) with compensation to nullify the vidicon rolloff characteristic was designed. An F.E.T. input stage was used to achieve the low noise characteristic and input high impedance to low output impedance transformation. The bandwidth of the preamplifier was designed for 7 mhz since the IV cannot resolve any more than 500 TV lines at the center of format.

Video Processor

The video processor (Fig. 5-6) was designed with a 10 mhz bandwidth and includes a keyed clamp, mixed blanking, mixed sync for tip insertion and a gain adjustment. It is capable of driving a 50-ohm coaxial cable of a relatively long length (30 feet) with no bandwidth or amplitude degradation.

5.2.3 IV Camera Test Results

This section contains the results of performance measurements on the Itek IV camera. The camera contains an RCA 8567 vidicon mated to an RCA image intensifier. Measurements are given for each of two vidicons, differing slightly from one another in resolution. Data were taken using a Telemeasurements, Incorporated 1962 resolution chart with a light box and a Wollensak 50-millimeter Cine Raptar lens. Comparative data using a Spectra Optoliner with standard RETMA resolution chart is also given on one of the tubes.

Slightly better resolution was measured with the light box, probably due to the better lens. All measurements are taken with the light box and Wollensak lens, unless noted. Resolution, dynamic range, and sensitivity were measured for each tube and are summarized in Tables 5-1 and 5-2. Measurements were taken using the experimental arrangement shown in Fig. 5-7.

Resolution was measured at each of several spatial frequencies in the center of the tube and at one spatial frequency along each of the four sides. Percent modulation was measured using the delayed-time-base oscilloscope and displaying only single lines. The single lines were identified with respect to the total raster by using the GATE A output of the oscilloscope, which provided z-axis blanking on the monitor of the single line being displayed on the oscilloscope. Resolution was normalized to 100 percent modulation using a black-to-white transition in the upper portion of the resolution chart.

Signal current, dark current, and limiting (5 percent modulation) resolution were each measured versus target illumination (I) and target voltage (V_T). Target illumination was measured by using the Spectra Optoliner (calibrated at 2,870 °K) to determine signal output current at a calibrated light level (1 foot-candle). Measurements were then taken using the Wollensak lens and lightbox, adjusted so as to give an identical signal current. Lower illuminations were obtained by using either neutral density filters or discrete increments in lens stops. Signal current measurements include dark current.

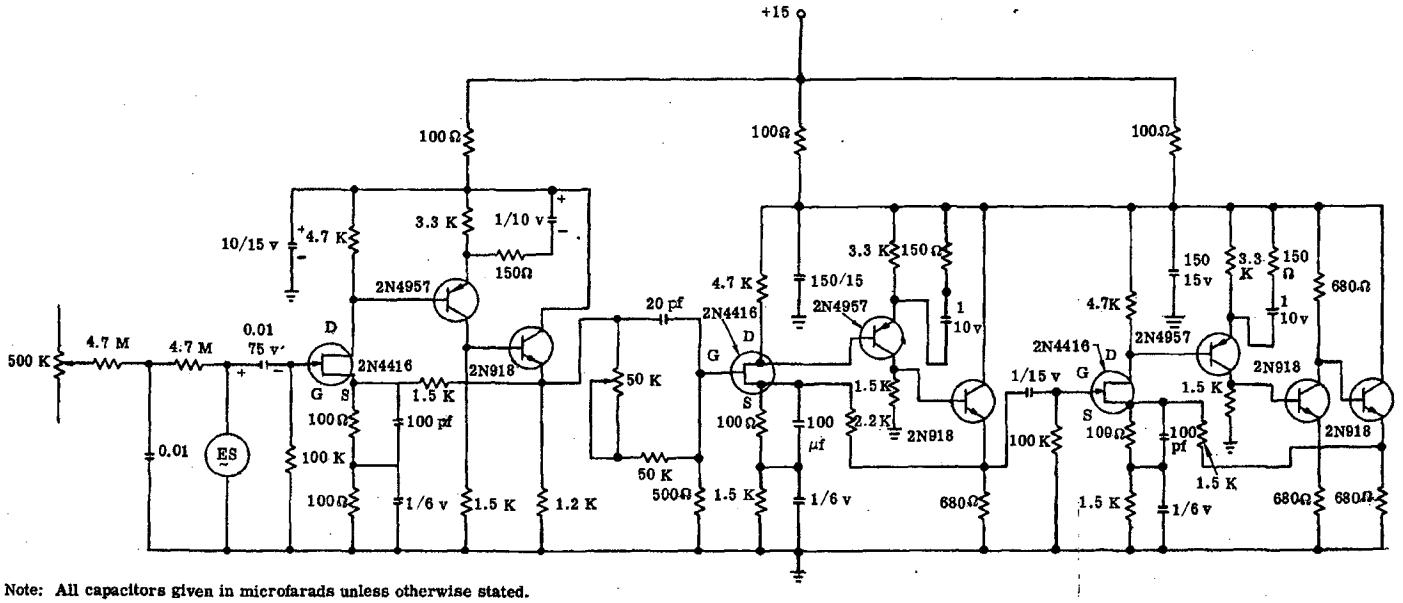

Note: All capacitors given in microfarads unless otherwise stated.
Es-standard signal generator (general radio Type 1001A) –10Ω output impedance.

Fig. 5-5 — Preamplifier

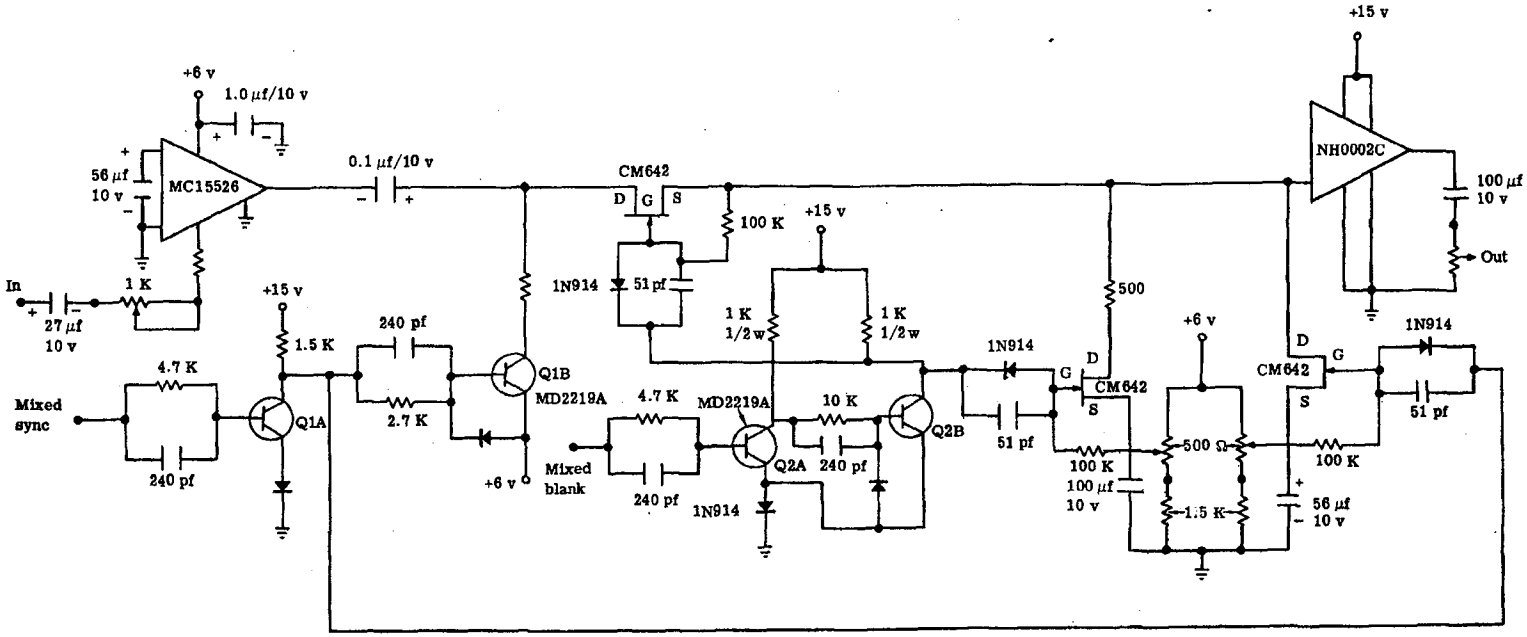

Fig. 5-6 — Video processor

Table 5-1 — Summary of Test Results for Higher Resolution Vidicon

1. Resolution (1 foot-candle at 2,870 °K, V_T = 13 volts)

	Lines Per Raster	Light Box, percent modulation
At center	200	50
	300	25
	400	15
	500	7
Top center	200	35
Bottom center	200	40
Left center	200	40
Right center	200	35

2. Signal current / dark current / limiting resolution versus target illumination (2,870 °K) and target voltage (na/na/TV lines)

I, foot-candle	V_T = 13 volts	V_T = 25 volts	V_T = 46 volts	V_T = 60 volts
10^0	240/2/525	Saturated	Saturated	—
10^{-1}	85/2/–	240/7/525	Saturated	—
10^{-2}	25/2/–	80/7/–	220/40/–	—
10^{-3}	7/2/–	22/7/–	70/40/–	–/–/300
1.25×10^{-4}	3/2/–	9/7/–	44/40/–	–/–/200

3. Number of gray scales at 1 foot-candle (2,870 °K): 9

4. Peak-to-peak noise: 325 mv

Table 5-2 — Summary of Test Results for Lower Resolution Vidicon

1. Resolution (1 foot-candle at 2,870 °K, V_T = 13 volts)

	Lines Per Raster	Optoliner, percent modulation	Light Box, percent modulation
At center	200	28	40
	300	16	20
	400	6	14
Top center	200	26	30
Bottom center	200	30	32
Left center	200	40	40
Right center	200	34	32

2. Signal current (na) versus target illumination (foot-candle at 2,870 °K)

I, foot-candle	V_T = 13 volts	V_T = 25 volts	V_T = 46 volts
10^0	225	Saturated	Saturated
10^{-1}	130	220	Saturated
10^{-2}	32	100	220
10^{-3}	10	27	98

3. Number of gray scales at (2,870 °K): 9

4. Peak-to-peak noise: 140 mv

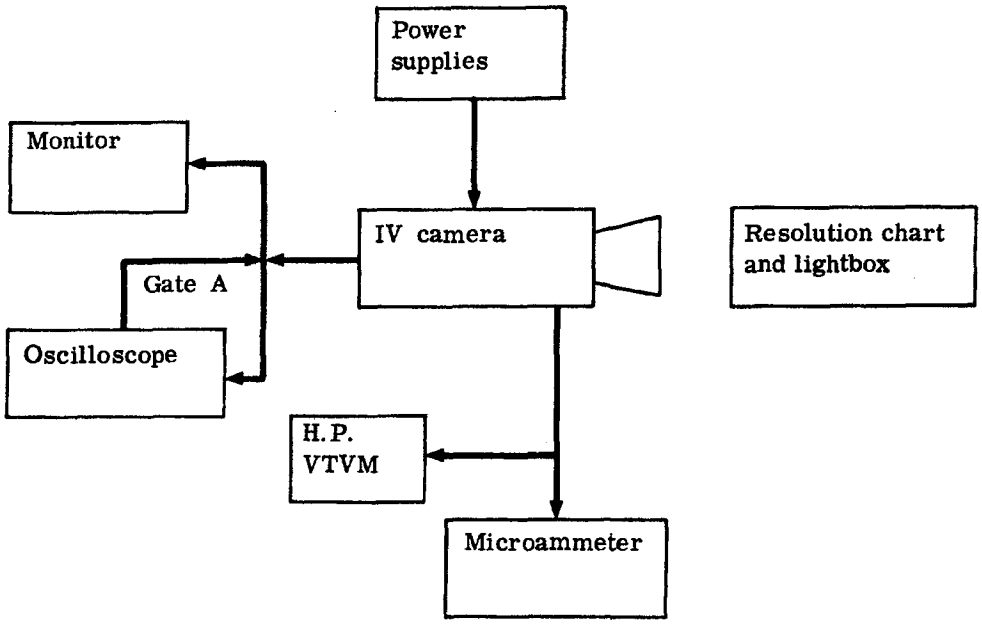

Fig. 5-7 — Intensifier vidicon camera test arrangement

The number of gray scales and peak-to-peak noise are both measurements that are more or less subjective. Gray scales were counted if there was any obvious modulation difference that was above the noise. Peak-to-peak noise is especially subjective and does not include all of the peaks. It is probably more representative of the three sigma limits of the noise distribution.

Improvements

Improvements could be made in the power supply and the preamplifier. The efficiency of the power supply could be increased by eliminating the series regulator and incorporating a switching regulator. A completely switching regulated power supply has been designed and tested in the IV but with adverse effects. The ripple at the output introduced noise in the video signal, and instability of the horizontal sweep generator required a more complicated redesign of the power supply which time did not permit.

The noise of the preamplifier has been of major concern in the IV. The equivalent input noise current is above 1 nonoampere for a signal bandwidth of 7 mhz. Several other preamplifier circuits have been designed and tested but the above noise current is the minimum value so far achieved at Itek.

5.3 INTENSIFIER RADIOMETRIC CHARACTERISTICS

5.3.1 Purpose of Measurement

A single stage 25-millimeter image intensifier was tested to evaluate its radiometric and photometric characteristics. The characteristics evaluated were: (1) photometric gain of the tube as a function of applied voltage; and (2) radiometric characteristics of the photocathode (input surface) and phosphor screen (output surface).

5.3.2 Equipment Used

1. EG&G model 585-11 monochromator housing with visible and IR gratings
2. EG&G model 585-63 detector head
3. EG&G model 585-00-63 controller
4. EG&G model 585-30 beam input optics
5. Spectra brightness meter model SB1/2
6. Bausch & Lomb model 31-33-53 microscope illuminator
7. Machlett Intensifier serial no. H1346
8. Spectra 100 foot-lambert calibrated lamp
9. Schneider componon, 80-mm, f/5.6 lens
10. Diffuse incandescent source.

5.3.3 Test Procedure

Photometric Test

The unit was tested by introducing the input face of the intensifier into the image plane formed by a Schneider Componon lens. The lens imaged a diffuse incandescent source at 1.18:1 conjugates. This condition forms an f/10.2 image (see Fig. 5-8).

Brightness at the output of the intensifier was measured with a Spectra brightness meter. Input illumination was determined by measuring scene brightness and lens transmission with the brightness meter and computing E as follows:

B_{target} = 225 foot-lamberts

B_{image} = 190 foot-lamberts

τ lens = 85 percent

Conjugate ratio = 1.18:1

$$\text{Image f/no.} = 5.6\,\frac{M+1}{M}$$

$$= 10.2$$

$$E_{image} = \frac{B \times \tau}{4\,(\text{f/no.})} = 0.45 \text{ foot-candle}$$

where B = brightness, foot-lamberts
τ = transmission
M = magnification
E = illumination, foot-candles

Perpendicular brightness was measured at various high voltage supply settings from 3 to 15 kilovolts. Brightness was also measured at various angles to determine if the output was lambertian.

Radiometric Test

Photocathode Response. The intensifier photocathode response was determined by placing the photocathode at the output of the monochromator and illuminating the photocathode surface (see Figs. 5-9 and 5-10). A Bausch & Lomb microscope illuminator was used as an energy source. The output was measured in foot-lamberts with the brightness meter. Intensifier voltage was maintained at 15 kilovolts. Various wavelengths (350 to 1,200 millimicrons) were used, and the output brightness was measured for each wavelength. The intensifier was removed and radiometric measurements on the monochromator output were made with the EG&G detector head. These readings were taken at the same wavelengths previously use to illuminate the intensifier. These two data runs provided a relationship of intensifier output to intensifier input.

Output Phosphor Response. The intensifier photocathode was illuminated with a 100 foot-lambert source and the output response was measured with a spectroradiometer (see Fig. 5-11). The test was run with intensifier voltages of 15 and 6.7 kilovolts.

5.3.4 Test Results

5.3.4.1 Photometric Gain Characteristics

Fig. 5-12 is a plot of the gain data obtained from perpendicular output brightnesses for various control voltages. Fig. 5-13 is a plot of viewing angle versus brightness.

The test data show the relationships of gain in foot-lamberts per foot-candle for various voltages. However, output energy in foot-lamberts is not meaningfull in evaluating vidicon performance. A meaningful term is gain in foot-candles per foot-candle.

It would be simple to make this conversion if the output were lambertian; however, as shown in Fig. 5-13, this is not the case when the output interface is air. For the lambertian case, the output brightness in foot-lamberts is exactly equal to the illumination in foot-candles.

Examination of the fiber output plate shows a Fresnel type reflection loss which varies with ray angle when the rays exit from the fiber optics. This loss would not be the same in a coupled IV, since all the surfaces are in optical contact.

Illumination with an air interface can be evaluated as shown in Fig. 5-14. Illumination through a small area A can be determined by integrating the total flux falling on the hemisphere.

$$F = \int_0^{\pi/2} (I_\phi)\,(d\Omega)$$

where F = flux in lumens

I_ϕ = intensity at angle ϕ

Ω = solid angle

$$d\Omega = \frac{(2\pi R \sin \phi)\, R\, (d\phi)}{R^2}$$

Examination of a normalized brightness versus viewing angle curve shows that the brightness falls off approximately as a function of cos ϕ, i.e., $B_\phi \approx B_\perp \cos \phi$. This is a conservative approximation. The perpendicular intensity of small area A is $I_\perp = B_\perp A$. The intensity varies by a cos ϕ term as the area viewed by the brightness meter increases by a cos ϕ term, i.e., $I_\phi = (B\phi)$ $(\cos \phi)$ (A). But B_ϕ as determined experimentally is $B_\perp \cos \phi$. Therefore, $I_\phi = B_\perp \cos^2 \phi\, A$. This results in the following expression:

$$E = F/A = \int_0^{\pi/2} B_\perp \cos^2 \phi \frac{(2\pi R \sin \phi)\,(R d\phi)}{R^2} = \frac{2\pi B_\perp \cos^3 \phi}{3}\Bigg]_0^{\pi/2}$$

$$E = \frac{2\pi}{3} B_\perp$$

where $B_\perp$ = brightness, candles/ft^2
E = illuminance, foot-candles

if $B_\perp$ is expressed in foot-lamberts

$$E = \frac{2}{3} B_\perp$$

As can be seen from the analysis, the conversion from brightness to foot-candles is between 0.66 and 1.0 times the perpendicular brightness in foot-lamberts. The actual illumination at the vidicon photosensitive surface would be less than this range due to losses within the vidicon faceplate. However, it is estimated that these losses are relatively small and the above stated range is valid, particularly in light of the conservatism of the cos ϕ approximation of brightness.

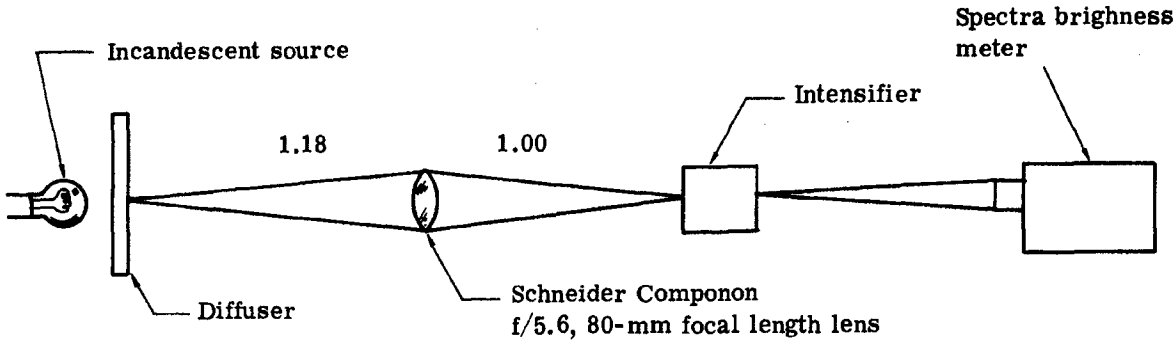

Fig. 5-8 — Photometric test arrangement

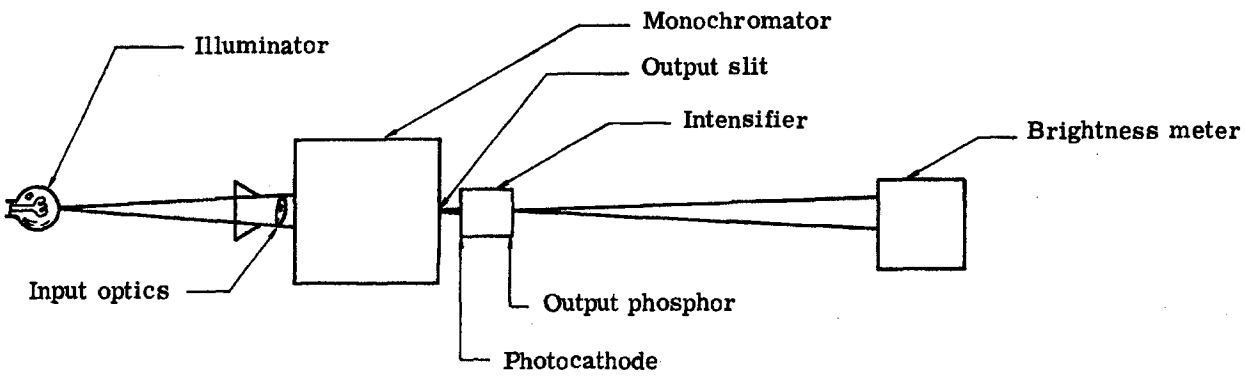

Fig. 5-9 — Photocathode response test arrangement, output brightness

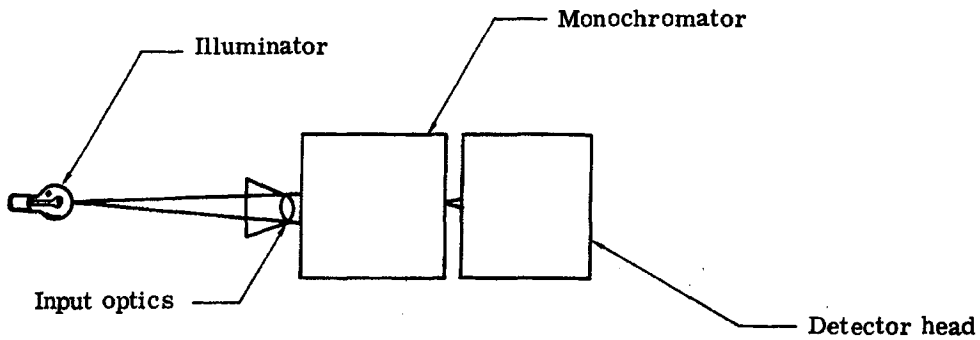

Fig. 5-10 — Photocathode response test arrangement, photocathode irradiance

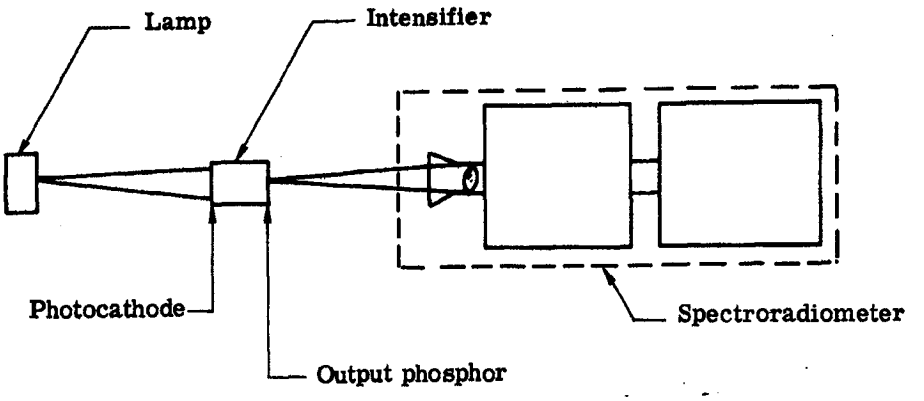

Fig. 5-11 — Output phosphor test arrangement

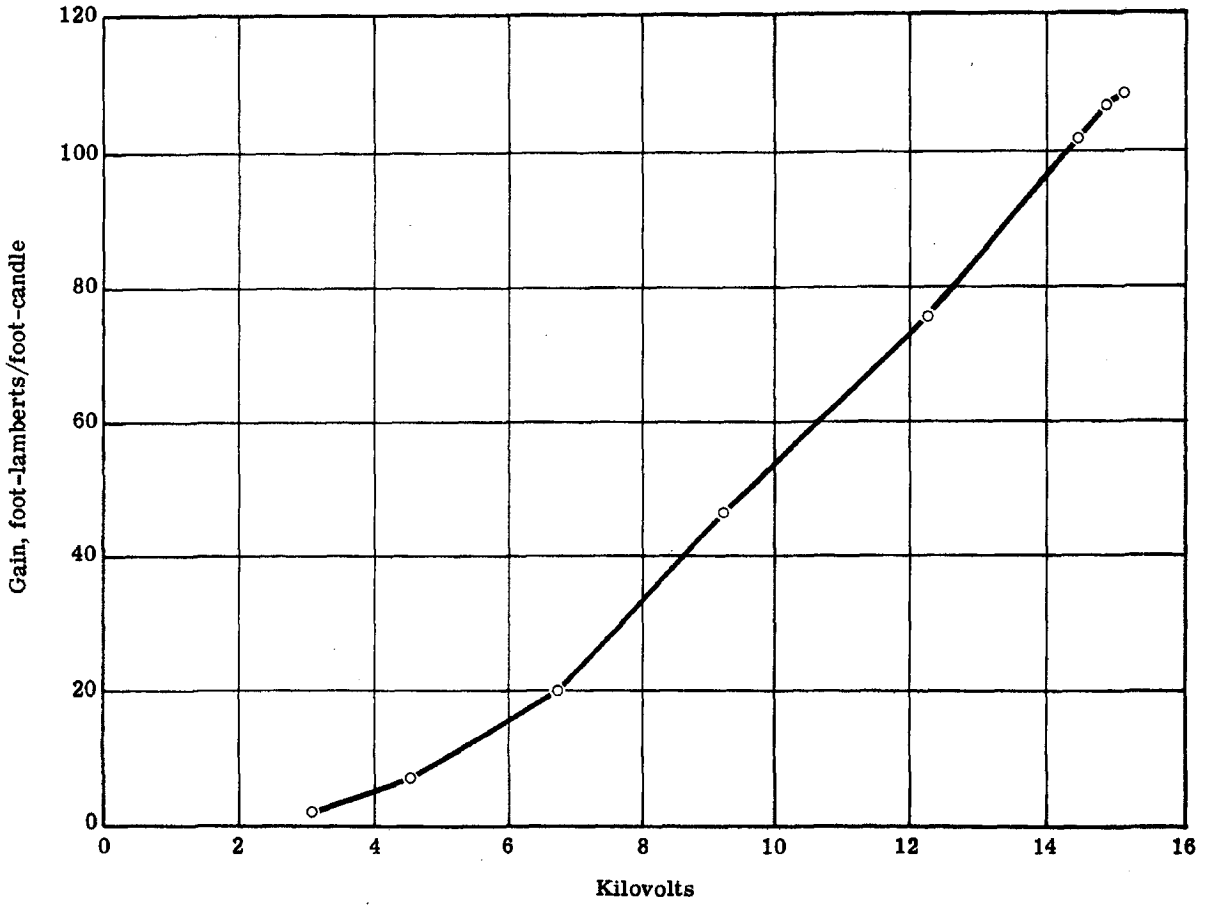

Fig. 5-12 — Gain versus voltage for perpendicular output brightness for various control brightnesses

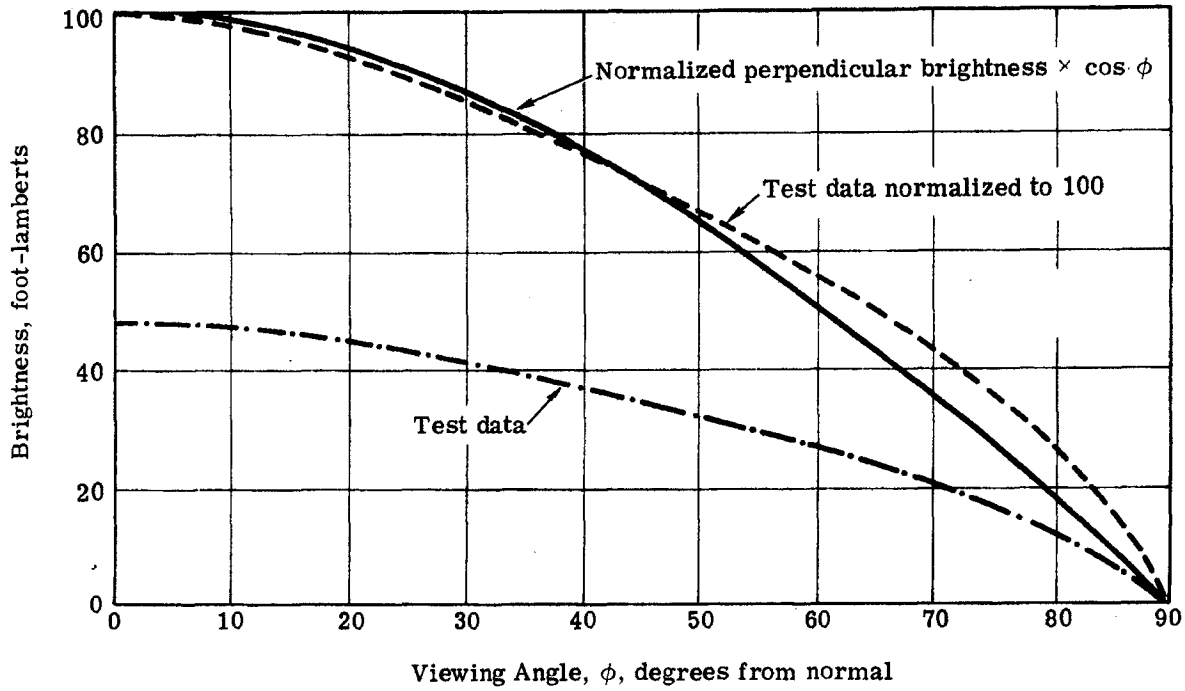

Fig. 5-13 — Viewing angle versus brightness

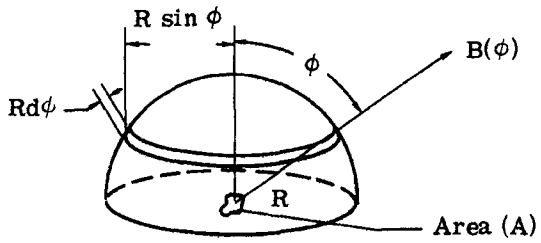

Fig. 5-14 — Illumination with an air interface

5.3.4.2 Radiometric Test

Figs. 5-15 and 5-16 are plots of the radiometric test data showing normalized response.

Photocathode response is claimed by the vendor to be S-20 with extended IR response. The experimental response curve was nearly indentical to an S-20 curve except it was displaced toward the IR by approximately 75 millimicrons.

Output phosphor response is claimed by the vendor to be P-20. The experimental curve had nearly the same shape as a P-20 but was shifted approximately 30 millimicrons toward the blue. As can be seen on Fig. 5-16, there was no appreciable difference in phosphor response at 15 kilovolts versus 6.7 kilovolts.

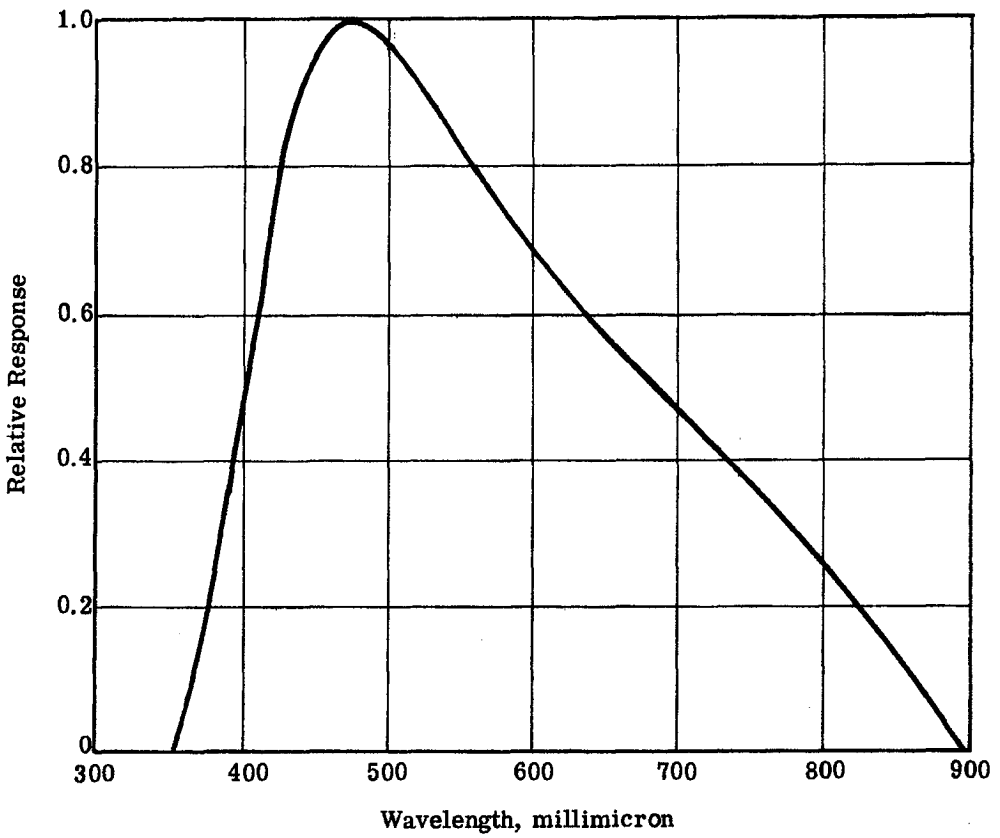

Fig. 5-15 — Relative response—intensifier photocathode

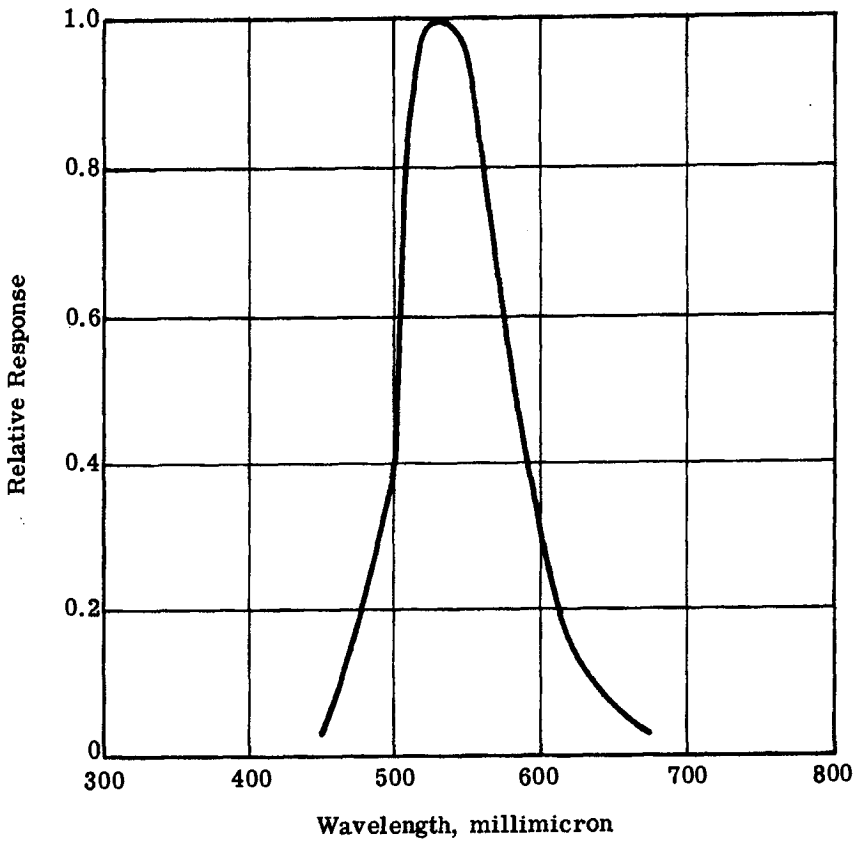

Fig. 5-16 — Relative response—intensifier output phosphor

6. POTENTIAL SENSOR IMPROVEMENTS

6.1 FIELD OF VIEW

The ETMA and EPEM sensors employ a 2 to 1 reduction between the interface aerial image and the face of the vidicon. A greater reduction would present more information to the vidicon and would reduce the magnitude of the error velocities seen by the vidicon.

The presence of more information at the vidicon face could provide two significant benefits. First, improved gain control can be expected because the possibility of encountering a scene with no information, such as an open field, is reduced. Second, scene features such as city streets, which, if viewed diagonally, can produce cross-coupling, comprise a smaller portion of the total scene and contribute less to the total sensor output.

Dynamic range and random bias variations are both dependent on modulation amplitude (see Section 2). The lower vidicon image velocities resulting from the greater minification allow a reduction in modulation amplitude, and, consequently, less random bias variations, with no sacrifice of dynamic range at the interface.

The choice of a minification ratio has always been a tradeoff between illumination level, off-axis velocities, and bias. Although the use of the image-intensifier has virtually eliminated light level as a consideration, the others are still important. However, the EPEM test results have indicated that the bias is low enough to seriously consider an increase in the minification ratio.

6.2 VIDICON CATHODE MODULATION

As indicated in Section 2, systematic bias was offset in the EPEM unit by adjustment of the vidicon alignment current. However, misalignment introduces aberrations into the vidicon electro-optical system. Limited tests have indicated that it is possible to alter the systematic bias by modulating the vidicon cathode potential at the line rate. This approach may provide greater vidicon sensitivity and an improved video signal-to-noise ratio.

6.3 FREQUENCY RESPONSE

The major deficiency in the sensor frequency response as it presently stands is the presence of a time delay caused by the scanning process. Doubling the camera frame rate would reduce the delay by approximately a factor of 2. In addition, a higher modulation frequency could be used, resulting in higher noise frequencies at the output, which would allow the time constant of the output filter to be reduced.

Appendix A

SYSTEM ENGINEERING AND ANALYSIS

1. INTRODUCTION

A description of the essential elements of the mathematical model used in a computer study of the Itek image velocity sensor has been reported previously.* The model and the associated computer programs during this initial phase of development were primarily concerned with the generation of modulation transfer functions for various conditions of image modulation and various values of constant input image velocity. These parameters are the determining elements which allow the sensor to behave as a velocity detector. The second area of development was the generation of the sensor output as a function of time through one complete modulation cycle. The third area of concentration was the harmonic analysis of the periodic output into the sensors components.

Previous to the referenced report, the primary effort has been a detailed study of the effects of the image motion modulation parameters, i.e., modulation frequency and velocity, on sensor performance.

A single discrete frequency analysis at 3.75-hz modulation was performed at this time, i.e., the input scene consisted of a target of a single, discrete, spatial frequency of unity brightness. This analysis proved valuable since it was the precursor for a later effort in determining sensor bandpass characteristics which led to a sound approach to the problem of automatic gain control (AGC).

During this period, the image motion computer program was developed further to introduce the effects of vidicon lag (i.e., incomplete erasure of a particular blur pattern during readout), such that a blur pattern carried over from one raster scan to the next at reduced intensity. Although this modified image motion program was completed, it was not used in any studies until the next stage of effort.

Also, during this initial period, no specification for the input scene spectra existed. Consequently, these first studies were made using uniform amplitude Wiener spectrum, i.e., "white" scenes, which was a convenient way of temporarily ignoring the effects of a real scene. However, the spectra were later specified and were introduced as an essential element of the sensor model.

The computer study program and the mathematical model initially proved themselves in a number of ways, some of which are indicated below:

1. Through bandwidth studies of image motion MTF curves, adjustment in video amplifier bandwidth brought about improved signal to noise ratio.

---

*Itek Report "Image Velocity Sensor," 9415-67-148, 15 August 1967. See Appendix A—System Engineering and Analysis, Sections 1 and 2, and Appendix C—Computer Programs for Sensor Analysis.

2. Plots of the second harmonic indicated that amplitude changed with input velocity and, consequently, pointed out the inadequacy of using the second harmonic as a signal for AGC over the required range of input velocities.
3. It was shown that the amplitude of the input velocity which started to show saturation effects is directly proportional to the modulation velocity. This led to an increase in the modulation velocity for an increase in the sensor dynamic range.

With this measure of success, the mathematical model was used in a series of practical problem solving efforts:

1. The sensor response due to a degradation of the Itek designed lens for purposes of establishing a minimum amplitude lens MTF which would be acceptable for use with the final product was studied.
2. By way of comparision with the lens degradation, a vidicon degradation study was made.
3. The effect of lens defocus over a range of ±0.050 inch in the interface image plane was studied.
4. A study of a possible mechanism for producing a bias signal was made. This effort was a relatively small one.
5. The possibility of a "fine-coarse" mode of operation for achieving improved sensor performance, i.e., greater dynamic range during target track and improved null accuracy after acquisition, was investigated.

The results of these studies are all reported in this report. They give an idea of the wide range of material that can be handled with relative ease and with a minimum of effort.

During this period a method of AGC was developed not based on use of the second harmonic. The mathematical model was extensively used to study the feasibility of the new technique. It was necessary to determine the sensor bandpass characteristics with varying degrees of vidicon lag and, also, to determine the dynamic range of sensor sensitivity as a function of the newly specified Wiener spectrum. It is the function of the AGC to maintain a constant sensitivity despite changes in the input scene. As a by-product of this study some interesting properties were uncovered relative to signal phase shifts with vidicon lag.

The last area that was studied during this phase of the effort was linear detection. This was a rather limited effort because of a lack of time. However, in the time available some meaningful comparisons of sensor performance were made between square law and linear detection. One very important result of this effort was to demonstrate that the AGC method developed previously when considering square law detection works equally well with the linear detector, i.e., independent of the type of detector used.

2. LENS TOLERANCE STUDY

The purpose of this study was to determine the relative effect of a range of lens MTF curves on sensor sensitivity and, consequently, under conditions of noise limited operation, the relative range of null error due to noise.

An average MTF curve over the region of the vidicon raster in the direction of image modulation was obtained for the triplet design lens which represented a fairly good lens with a half-power bandwidth at 25 lines per millimeter.* This is shown in Fig. A-1 labeled "average," together with several other degraded MTF curves labeled 25, 50, 75, and 87.5 percent. Each curve with a given percentage degradation was arrived at by taking a point on the average curve and reducing the given value of frequency by the indicated percentage maintaining the same amplitude of MTF, i.e., the 50 percent curve is obtained by multiplying the frequency scale of the "average" curve by 0.5, etc.

Each of these curves was then used in turn in the mathematical model to determine a normalized sensor sensitivity shown in Fig. A-2. These curves were generated for conditions of 15-hz modulation, 1/4-inch-per-second peak modulation velocity, zero lag and an average Wiener spectrum with exponent of 1.5. (See Section 6.2 of this Appendix or system specification no. EC701A, revision 5.)

Since the sensor null error under noise limited conditions is inversely proportional to the sensitivity, the second curve of Fig. A-2 shows the relative increase in null error with lens degradation.

The interesting feature of these curves is that between the "average" and the 25 percent degraded curves there is no noticeable change in sensitivity or null error, i.e., the sensor is quite insensitive to lens MTF variation in this region. The 50 percent degraded curve shows only a 7 percent increase in null error.

Image Defocus

A family of defocus MTF curves, each one representing the average MTF over the field of view of the vidicon, was derived for the Itek designed triplet lens. The average MTF has been computed at focus increments of 0.003 inch over a range of ±0.015 inch from paraxial focus. The nominal focus position is given by a defocus of −0.003 inch from paraxial focus, (see Fig. A-3). Because of the scale factor the defocus in the interface image plane covers the range of ±0.050 inch in increments of 0.010 inch.

These curves were used in the sensor mathematical model to determine the consequent change in sensitivity. The nominal operating conditions for the study were 15-hz modulation frequency, 1/4-inch-per-second modulation velocity, zero lag and a real scene with an average 1.5 exponent (see Fig. A-4).

The system sensitivity decreased by a factor of 1.8 from the nominal focus position. It can be seen from the curves that initially the sensitivity does not change rapidly but the relative change increases with increasing defocus. The minimum sensitivity for the 0.050-inch defocus in the interface image plane is equivalent to the 87.5 percent lens degradation reported previously.

3. VIDICON TOLERANCE STUDY

A vidicon tolerance study (similar to the lens tolerance study in Section 2) was made to determine how rapidly the sensor sensitivity deteriorated with degradation of the vidicon MTF curve. The conditions of this computer run were again similar to those of Section 2, i.e., 15-hz modulation, 1/4-inch-per-second peak modulation velocity, zero lag, and an average Wiener spectrum with an exponent of 1.5.

---

*Internal Memo No. OSED-2-68-39, 31 January 1968.

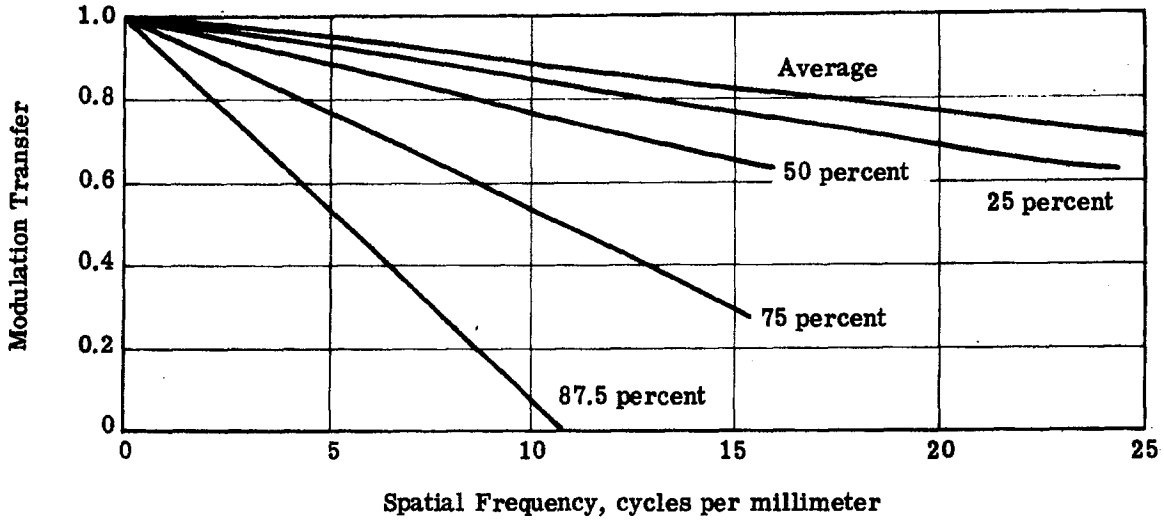

Fig. A-1 — Triplet design lens MTF and degraded curves

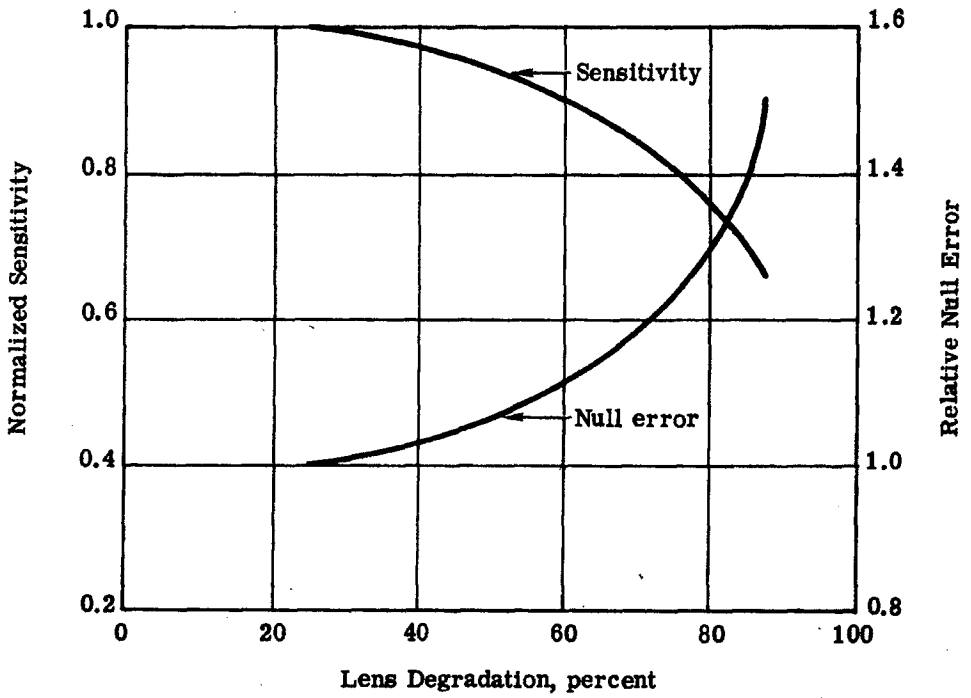

Fig. A-2 — Sensitivity and null error versus percent lens degradation

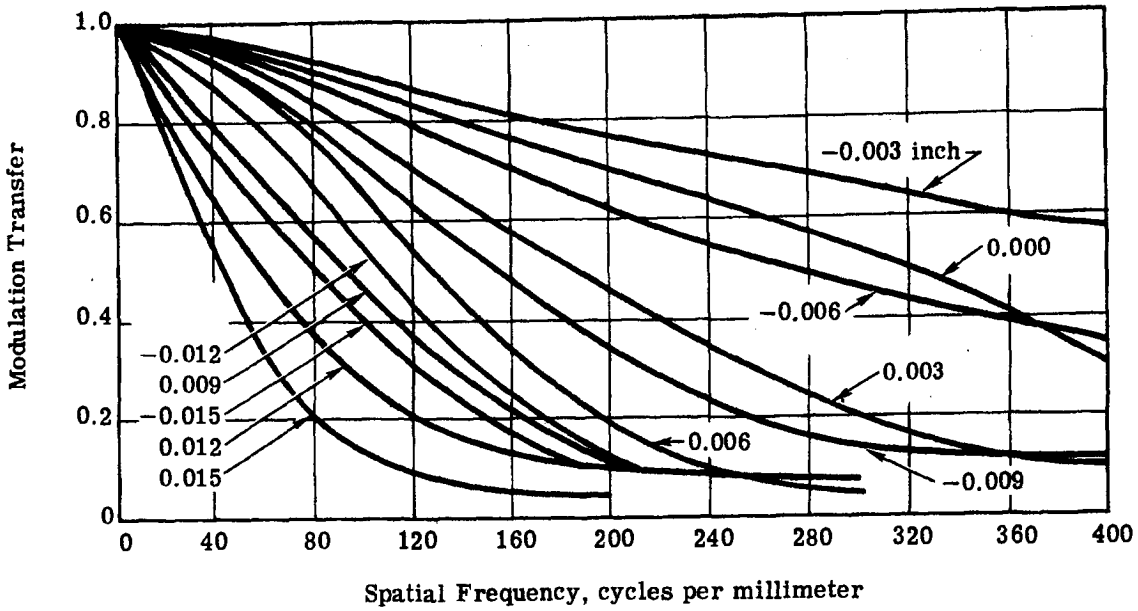

Fig. A-3 — Average MTF ±0.015 inch through focus

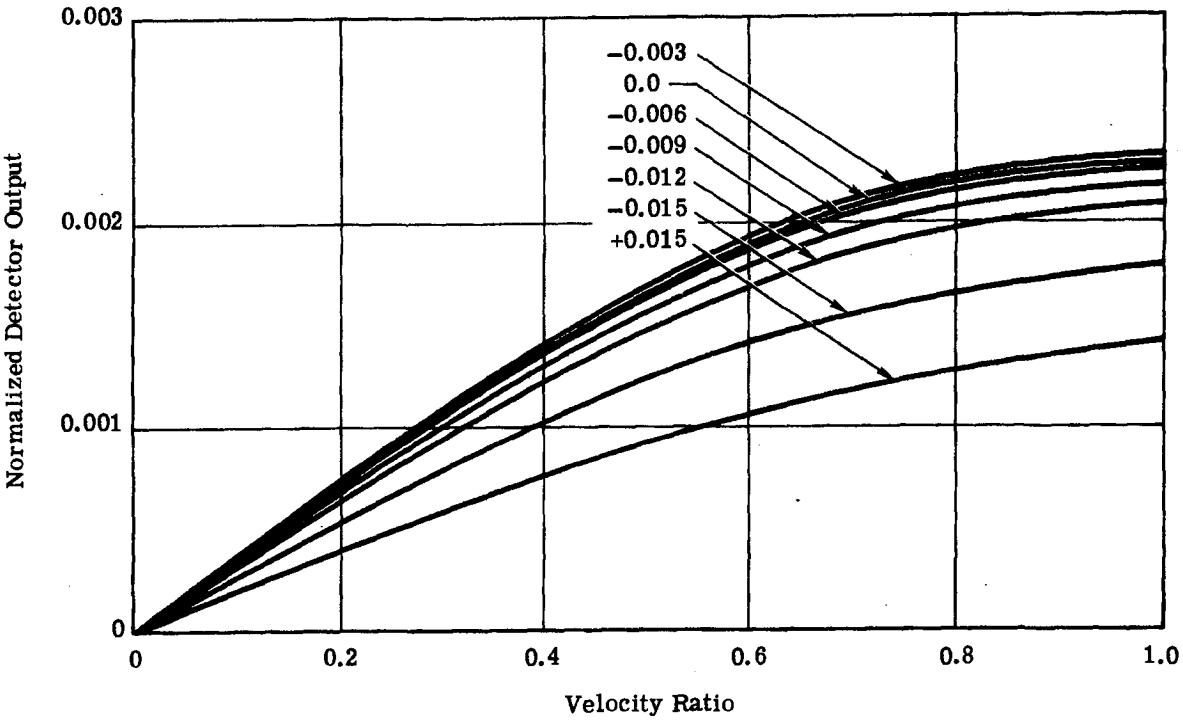

Fig. A-4 — Detector output versus velocity ratio for defocused triplet lens

Fig. A-5 is a curve of the normal vidicon MTF curve for the grid voltages as shown. This curve was degraded by 10, 20, 30, and 40 percent in the same sense that the lens was degraded (see Section 2).

Fig. A-6 shows the change in sensitivity with percent vidicon degradation and, assuming noise limited operation, a second curve shows the respective increase in the null error.

In comparison with the lens, the sensor sensitivity drops off more rapidly for changes in the vidicon MTF than for equivalent percent changes in the lens MTF.

4. FINE-COARSE MODE

Previous system studies with the mathematical model have indicated the possibility of a fine-coarse mode of operation which would provide the sensor with a degree of flexibility and improvement in performance. This fine-coarse mode would consist of a change in the peak modulation velocity of the modulator during the track of a particular target.

Fig. A-7 is a plot of sensor sensitivity as a function of peak modulation velocity under the conditions of 15-hz modulation frequency, zero lag and a flat Wiener spectrum. The figure indicates that the sensitivity increases with decreasing peak modulation velocity.

Fig. A-8 is a plot of the input saturating velocity versus the peak modulation velocity under the same conditions of operation. The input velocity required to produce saturation increases with an increase in the peak modulation velocity. Therefore, it was believed that at the start of a track a relatively high modulation velocity would give rise to a wide dynamic range of operation prior to saturation even though the sensitivity would be low. Under noise limited operation the low sensitivity gives rise to a poor null but during the initial phases of track or lock-on this is of small concern. As the relative velocity of the target is decreased through control of the tracking mirror and the wide dynamic range is no longer required, a decrease in the peak modulation velocity gives rise to increased sensitivity and consequently improved null accuracy for the concluding stages of the track.

With the inclusion of the definition of the Wiener spectrum in specification EC701A, revision 5, a repeat of the computer study that resulted in the data in Fig. A-7 was made with the substitution of the Wiener spectrum for the flat spectrum. The two limiting cases of the spectrum were used to show the bounds of sensor sensitivity, i.e., minimum and maximum rate of change of the spectrum with spatial frequency as expressed by the exponents -1.1 for minimum and -1.7 for maximum.

The results are shown in Fig. A-9. The original increase in sensitivity at the lower modulation velocities is seen to have been lost particularly with the -1.7 spectrum and no improvement in null accuracy could be expected. Although the curve of constant -1.1 spectrum indicates some increase in sensitivity at 1/8 inch per second relative to 1/4 inch per second, this increase amounts to only about 10 percent. However, the increase in sensitivity on the -1.7 curve at 1/4 inch per second relative to 1/8 and 1/16 inch per second indicates that operation around 1/4-inch-per-second modulation velocity is nearly optimum.

The difference in Figs. A-7 and A-9, indicates that the total sensitivity results from the combined effect of the sensor bandpass characteristic and the scene spectrum as given by

$$K = \int \phi(\omega)\, K(\omega)\, d\omega$$

where $\phi(\omega)$ = Wiener spectrum
$K(\omega)$ = sensor bandpass characteristic

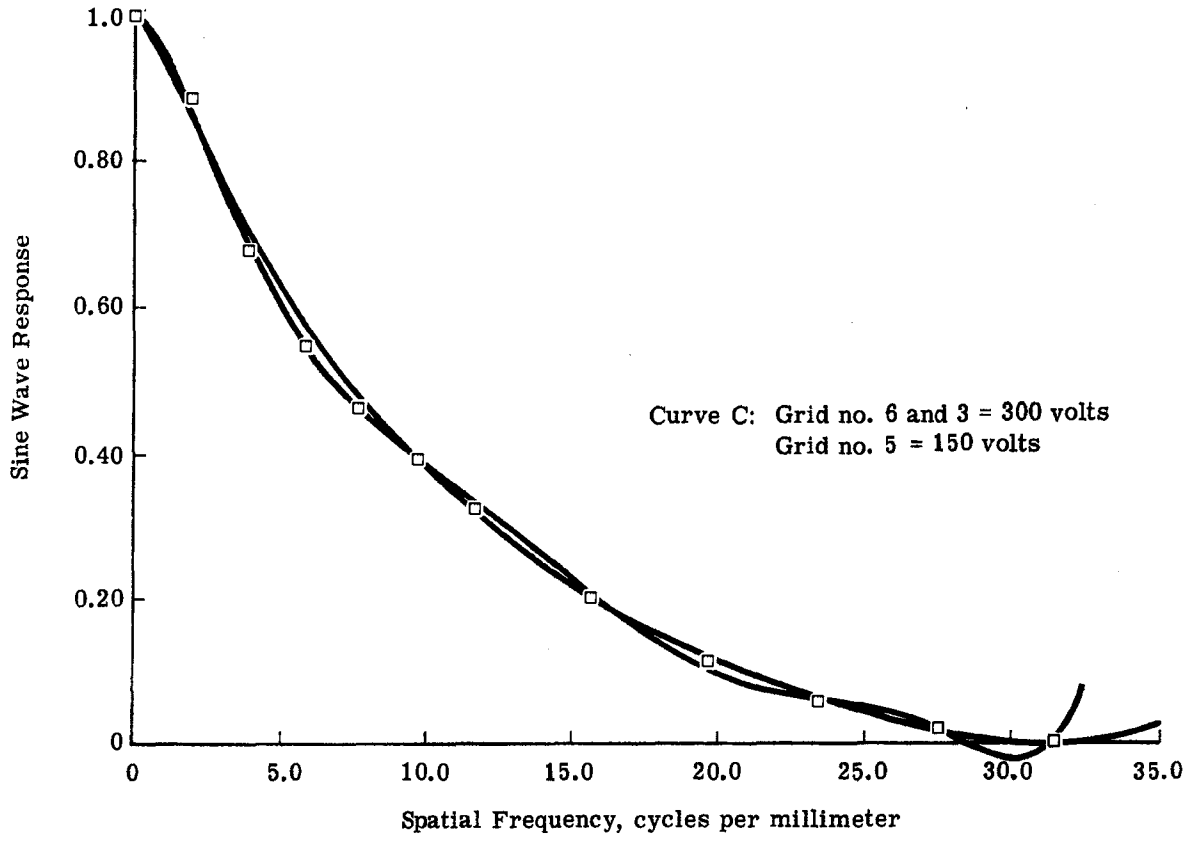

Fig. A-5 — Vidicon 8567—polynomial approximation

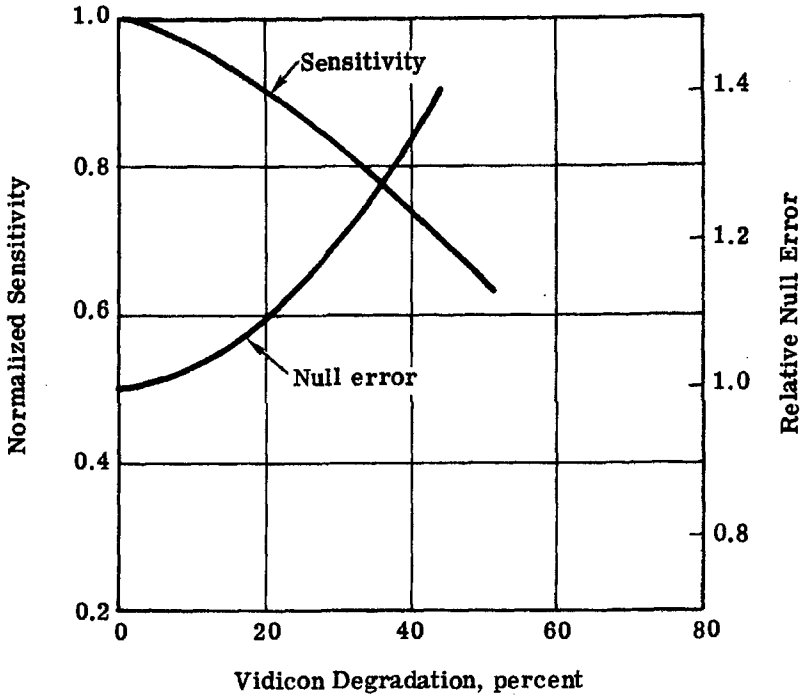

Fig. A-6 — Sensitivity and null error versus percent vidicon degradation

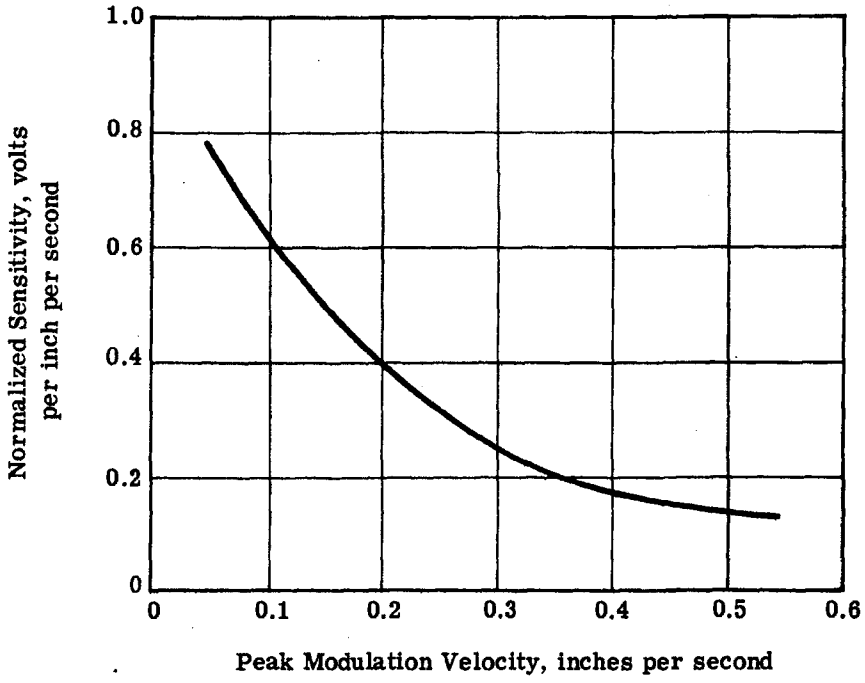

Fig. A-7 — Fundamental sensitivity versus peak modulation velocity

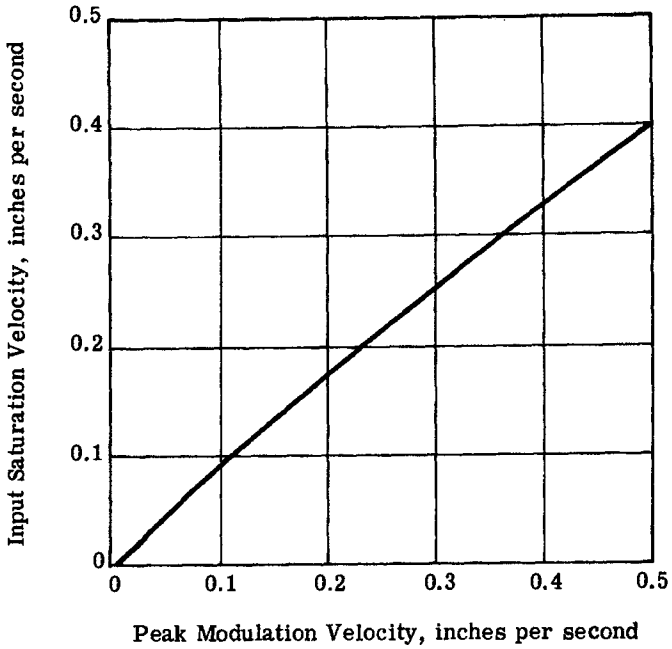

Fig. A-8 — Input saturation velocity versus peak modulation velocity

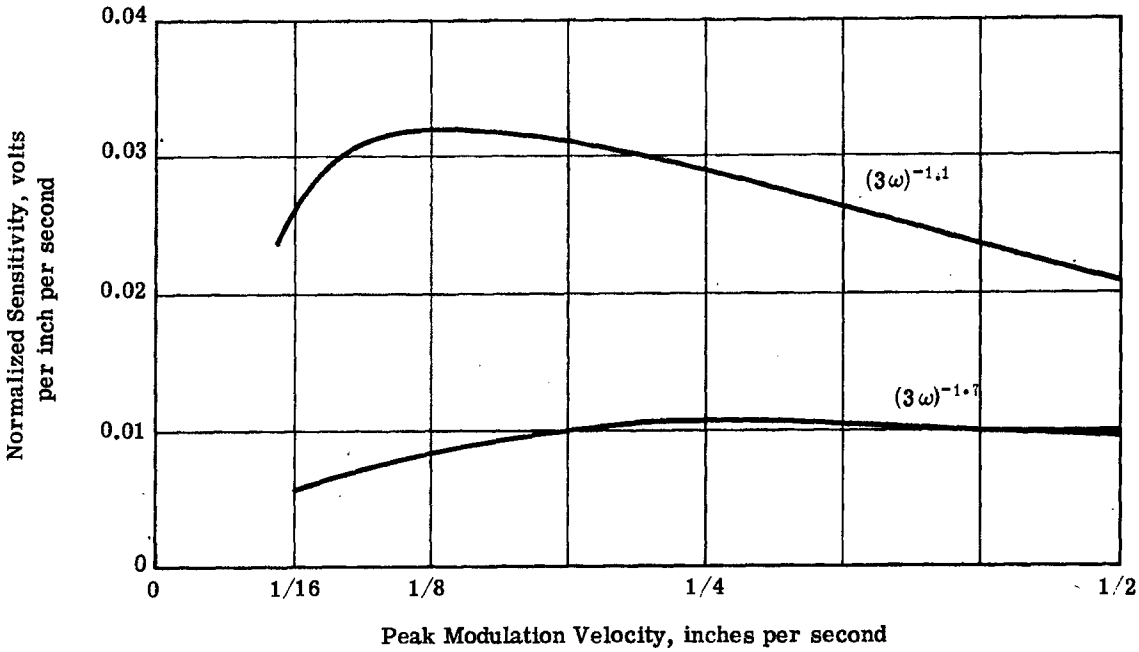

Fig. A-9 — Sensitivity versus peak modulation velocity with scene spectra

In Fig. A-7 the spectrum is assumed flat and normalized to unity such that the sensitivities at the various modulation velocities represent the value of the integral of the sensor bandpass characteristic for each value of modulation velocity. The sensitivities in Fig. A-9 are the integral of the product of the scene spectrum and the bandpass characteristic which is representative of the real situation.

5. BIAS STUDIES

A possible source of bias considered is the modulation of an image on a vidicon whose modulation transfer function chances as a function of distance from the center of the raster. Therefore, in the mathematical model the vidicon MTF was made to vary in a sinusoidal fashion at the same frequency as that of modulation. Thus, as the image is displaced sinusoidally, parts of the image (depending on the nature of the nonuniformity of the MTF and depending on the distribution of scene information across the face of the vidicon) are subjected to sinusoidal variations in spatial filtering. The amplitude of the MTF generally decreases as a function of distance from the raster center. Therefore, for image displacements away from the center greater attenuation occurs, and towards the center, amplification occurs.

Initially, to demonstrate the characteristics of this phenomenon, the vidicon MTF was assumed to degrade linearly from the raster center to the edge over all frequencies within the range of vidicon response. Also, the total degradation in performance at the edge relative to the raster center was assumed to vary in steps of 80, 60, 40, 20, and 0 percent.

Since the image modulation is limited to a peak-to-peak displacement of 0.006 inch, the peak-to-peak change in the vidicon MTF as seen by any portion of the scene is given by

$$\frac{\text{Maximum displacement}}{\text{Length of 1/2 raster width}} \times \text{percent change in MTF from center to edge}$$

Thus, for the above assumed maximum percentage changes in MTF and with an assumed 1/2 raster width of 0.24 inch, the maximum percent change in vidicon MTF over the modulation cycle corresponds to 0.5, 1.0, 1.5, 2.0, and 2.5 percent, respectively.

The results of the computer study show that some fairly high levels of bias are achieved based on the model used. It was shown that the bias over each half of the raster is of opposite polarity, as anticipated, since the direction of change in the MTF is reversed relative to the direction of modulation.

It can be stated that for equal percent degradation in the vidicon MTF over each half of the raster, the bias reduces to zero in using a full line rather than a split line since the negative bias of one side cancels or compensates the positive bias of the other side.

The model also predicts that the bias for a split line decreases with a decrease in the peak modulation displacement.

6. AUTOMATIC GAIN CONTROL (AGC)

This study was undertaken to investigate possible improvements in AGC, and to develop a rationale for the operation of an AGC circuit. It has been observed, from previous mathematical model studies, that the second harmonic, which had been used as an AGC signal, changed in amplitude by 40 to 50 percent over an input velocity range from zero to one-half the peak modulation velocity. Therefore, despite the performance of the second harmonic in accommodating changes in signal strength due to changing scene characteristics, it was also causing gain changes

with scene velocity to add to difficulties of maintaining a constant sensor sensitivity and linearity over a reasonable velocity range. The variation in second harmonic amplitude with velocity has also been confirmed experimentally to approximately the same magnitude.

The available signals for use as an AGC signal are not many. There are the higher harmonics available such as the third and fourth as well as the second harmonic and also the average dc and the average ac of the video signal.

It was observed from the mathematical model that the average video ac power was constant to better than 10 percent over the same velocity range as quoted above in connection with the second harmonic. Therefore, it was decided to investigate the possibility of using the average video power to determine how the average video power changed with scene parameters in relation to the fundamental, and to determine if the two were compatible.

6.1 Theory of AGC

Since AGC is required to make the sensor sensitivity independent of changes in scene parameters (average brightness, contrast or modulation and scene content) it is necessary to relate sensitivity to the scene. Any scene can be described in terms of its Wiener spectrum. The system specification provides, in terms of the Wiener spectrum, a range of scene characteristics to be encountered in practice at least as well as can be defined at the present time. Therefore, with the sensor bandpass characteristic and any given scene spectrum the total sensitivity is given by

$$K_{total} = \int \phi(\omega)\, K(\omega)\, d\omega \ \frac{\text{volts}}{\text{inch/second}}$$

where $\phi(\omega)$ = scene Wiener spectrum in $(\text{brightness})^2/\text{cycle/mm}$
$K(\omega)$ = bandpass characteristic expressed as volts/inch/second/$(\text{brightness})^2$ out of a square law detector

Similarly the total average power is given by

$$\bar{P}_{total} = \int \phi(\omega)\, P(\omega)\, d\omega$$

where $P(\omega)$ = the bandpass characteristic of the average video power expressed as volts/$(\text{brightness})^2$ out of a square law detector

The sensitivity, K_{total}, and the average power, $\bar{P}_{total}$, will be the same function of the scene spectrum (for purposes of AGC) provided

$$P(\omega) = \alpha\, K(\omega)$$

where α = a constant multiplier

As will be shown later, $P(\omega)$ has a low pass filter characteristic and $K(\omega)$ is a bandpass filter such that the equality above does not hold. By inclusion of a filter in a branching channel (see Fig. A-10) such that

$$P(\omega)\ |MTF|^2_{filter} = \alpha\, K(\omega)$$

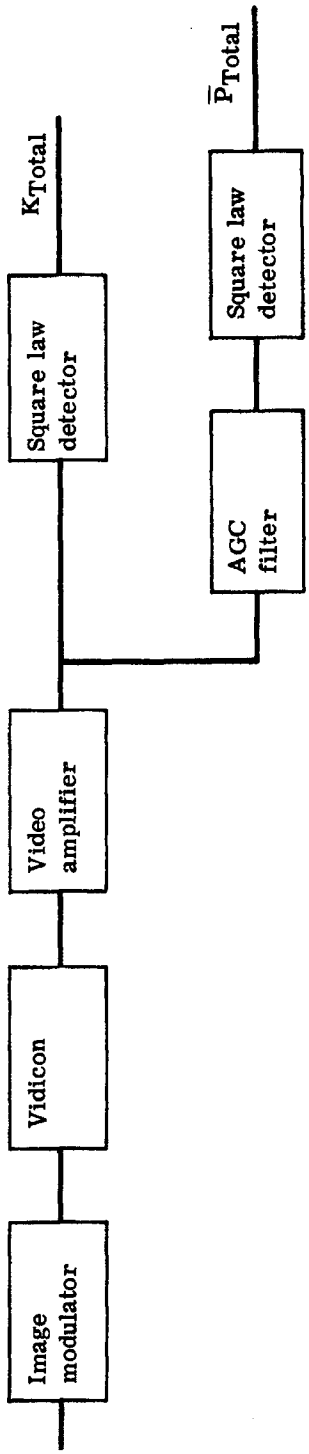

Fig. A-10 — IVS system with AGC filter in branching channel

then

$$\bar{P}_{total} = \int \phi(\omega)\, P(\omega)\, |MTF|^2\, d\omega = \alpha\, K_{total}$$

and

$$d\bar{P}_{total} = \alpha\, dK_{total}$$

Therefore, the average video power changes with scene spectrum are comparable to changes in the total sensitivity. Also, the required filter characteristics are determined directly from $K(\omega)$ and $P(\omega)$,

$$|MTF| = \left[\frac{K(\omega)}{P(\omega)}\right]^{1/2} k$$

where k = a normalizing constant

6.2 Bandpass Characteristics

To study the feasibility of the above method of AGC, the mathematical model was used to determine the bandpass characteristics of the fundamental component of the signal and the average video power.

Fig. A-11 is a plot of the amplitude of the fundamental component at the output of a square law detector versus input velocity for a range of discrete spatial frequencies used as the input scene. The brightness amplitude of each input frequency is normalized to unity. Also, a zero discharge or readout lag $\rho = 0.0$ is assumed.

It is noted that for frequencies of relatively high sensitivity, the curve is linear to an input velocity ratio of approximately 0.5 (fractional part of the peak modulation velocity). The extended linear range of the low frequency of 2/3 cycle per millimeter is of considerable interest which indicates that, generally, the linear range of low frequencies is greater than that of high frequencies.

A polarity inversion is observed over a small range of spatial frequencies for a portion of the input velocity range (see curves for $7\frac{1}{3}$ and 8 cycles per millimeter). This is of not much significance because of the relatively small amplitude of signal in comparison to some of the other frequencies.

Fig. A-12 is similar to Fig. A-11 with the addition of a 0.2 factor of lag, i.e., 0.2 of the signal remains after readout. The most significant effect of the lag is the decrease in linearity over the velocity range 0 to 0.5 and also the introduction of phase shift both as a function of input velocity and as a function of spatial frequency. As a consequence of this phase shift and the use of a phase sensitive detector in the signal processing, the fundamental amplitude has been corrected by the cosine of the phase shift from an average phase which maximizes the output. The corrections were made only over the velocity range 0 to 0.5.

Fig. A-13 is the same plot with additional lag, i.e., $\rho = 0.4$. Again the data have been corrected for phase shift over the velocity range 0 to 0.5. The most significant effect of the increased lag is the marked decrease in the linear range. The low frequencies, i.e., 2/3 and 4/3 cycles per millimeter, still show better linearity. Also, the frequency of 18/3 (6) cycles per millimeter which showed no polarity inversion for $\rho = 0.2$ (Fig. A-12) does go through an inversion when $\rho = 0.4$.

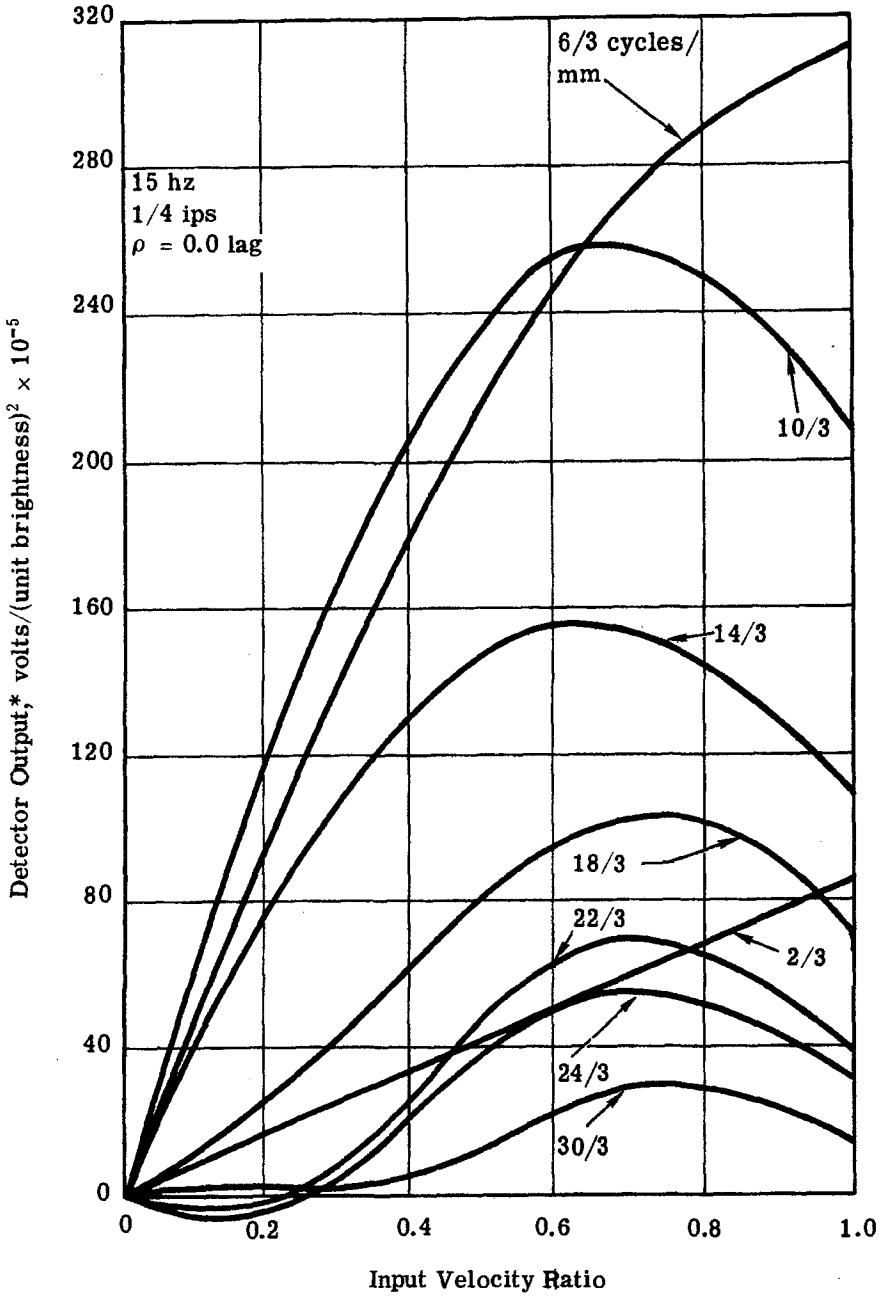

*Multiply by 96 scale factor for true normalized output volts.

Fig. A-11 — Detector output versus input velocity for a range of discrete spatial frequencies

15 hz
1/4 ips
ρ = 0.2 lag
(corrected for phase shift)

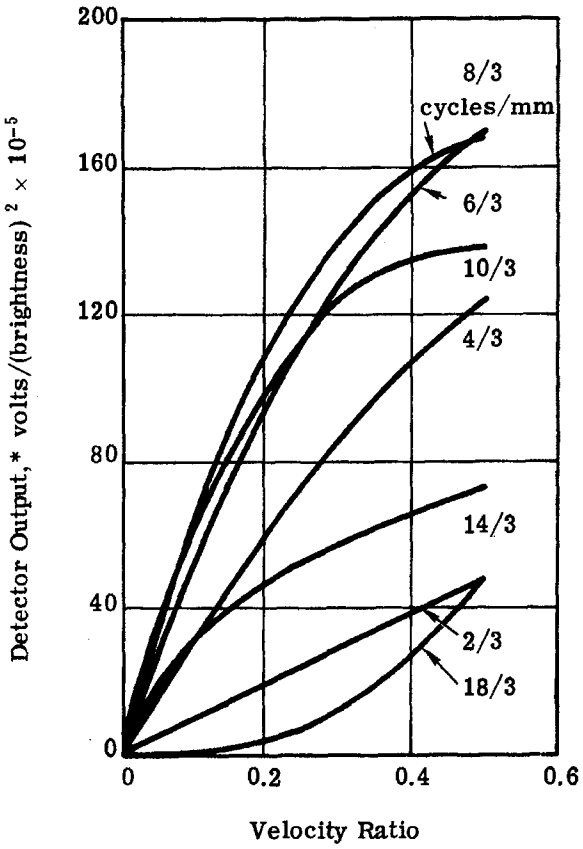

*Multiply 96 scale factor for true normalized output volts.

Fig. A-12 — Detector output versus input velocity (0.2 lag factor) for a range of discrete spatial frequencies

BIF-059-4035-69

15 hz
1/4 ips
ρ = 0.4 lag (corrected
for phase shift)

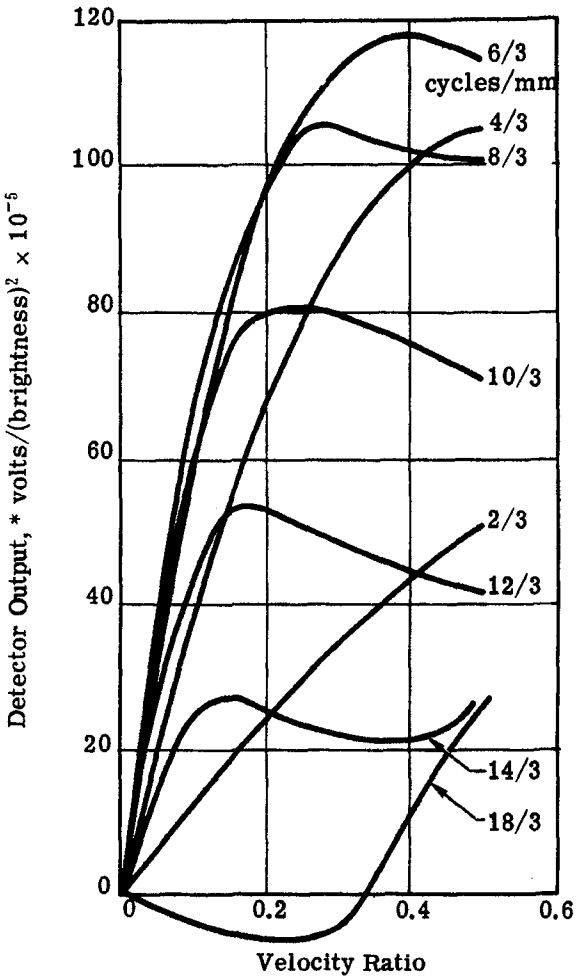

*Multiply by 96 scale factor for true normalized output volts.

Fig. A-13 — Detector output versus input velocity (0.4 lag factor) for a range of discrete spatial frequencies

From each of the figures it is possible to determine a linear sensitivity for each of the spatial frequencies which determine the bandpass characteristic, $K(\omega)$, at each value of lag. From the harmonic analysis of the detector output which gives the amplitudes of the fundamental for Figs. A-11, A-12, and A-13 the average video power is also obtained. The bandpass characteristics for the fundamental and the average video for zero lag are plotted in Fig. A-14. A plot of the AGC filter for modifying the average video as derived from the fundamental and average video bandpass characteristics is shown in Fig. A-15. Fig. A-16 is a plot of sensitivity and average video power with and without the filter of Fig. A-15 as a function of scene spectrum. The scene spectrum is defined in the system specification no. EC701A revision 5 as an inverse function of spatial frequency to the (m + 1) power

$$\phi(\omega) = \frac{K}{\omega^{(m+1)}} \frac{(\text{brightness})^2}{\text{cycles per millimeter}}$$

where $1/3 \leq \omega \leq 15$ cycles per millimeter at vidicon with 24,000:1 scale factor and $1.1 \leq m + 1 \leq 1.7$

It can be seen, from Fig. A-16, that the average power without the filter only changes half as much as the sensitivity in going from the 1.1 to the 1.7 spectrum. With the addition of the filter, the change in average power agrees very closely with the change in sensitivity (to within two decimal places) over the range of scenes.

Similarly for discharge lags of 0.2 and 0.4, the bandpass characteristics for the fundamental component and the average were determined, together with the AGC filter characteristics. Finally, the sensitivity and average power with and without the AGC filter were determined. These are plotted in Figs. A-17 through A-22.

The principle results are shown in Figs. A-19 and A-22 where it is again demonstrated that changes in the average video power with the filter follow very closely the changes in sensitivity (within 3 percent as the scene spectral density changes. With an increase in the lag, the accuracy of determining the AGC filter characteristics decreases, first of all, due to the required amplitude correction of the fundamental component for phase shift and, secondly, due to the increased error in linear approximation of the sensitivity at each spatial frequency over the velocity range of interest (see Figs. A-12 and A-13). For the case of 0.4 lag, the linear range is reduced such that linear approximations to the sensitivity were made over the velocity range 0 to 0.2 of the peak modulation velocity.

6.3 Linearization and Extended Dynamic Range

An interesting byproduct of the AGC signal which is described in Section 6.2 above is its effect on linearizing the fundamental, and thus extending its linear range beyond the input velocity ratio of 0.5 to at least a velocity ratio of 1.0 which was the upper limit of velocities used in these studies.

This comes about as a consequence of the fact that the AGC signal shows some increased dependence on velocity as lag is introduced. Assuming that the AGC is connected in a feedback loop such as to modify the forward loop gain in inverse proportion to the level of the average video, the fundamental was multiplied by the inverse of the relative change in the average detected video. The results are shown plotted in Figs. A-23 and A-24 for the two extreme cases of input scene spectrum, i.e., scene spectrum of 1.1 and 1.7. It can be seen that not only is the linearity improved over the velocity range zero to 0.5 but, also, the dynamic range is considerably extended.

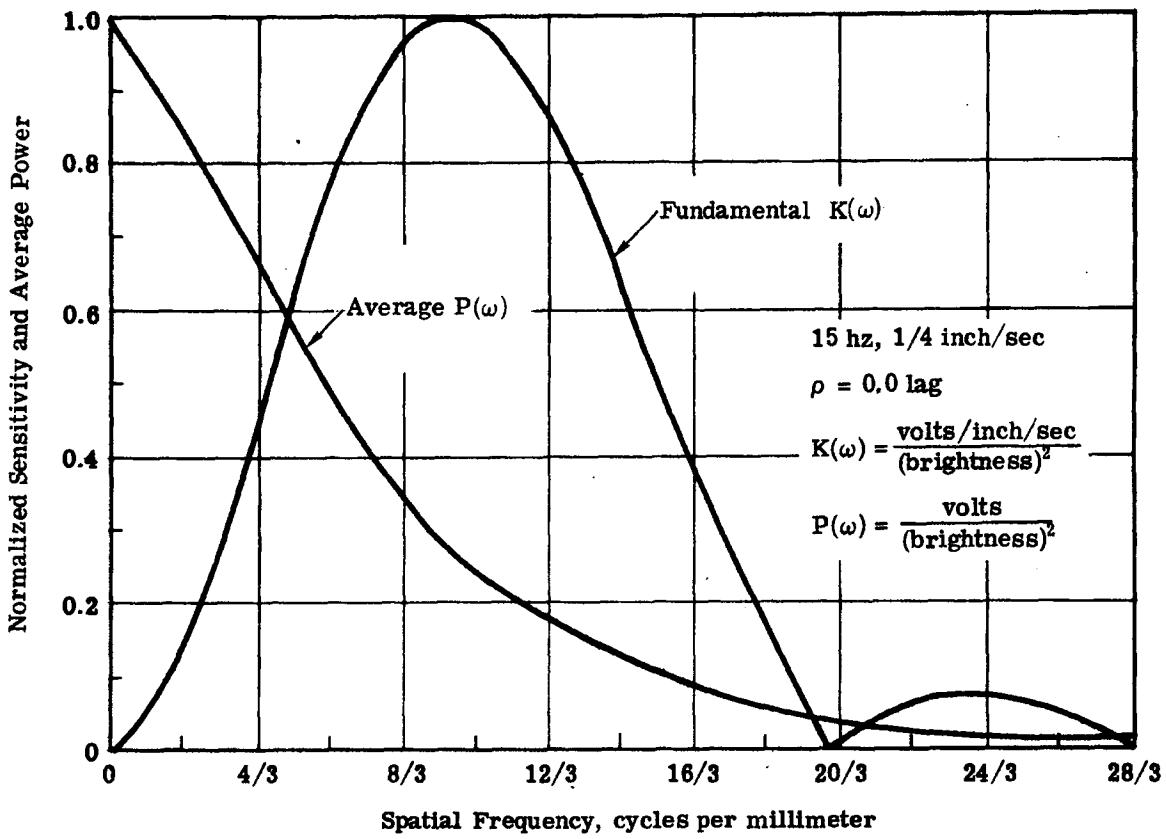

Fig. A-14 — Bandpass characteristics—fundamental component and average value

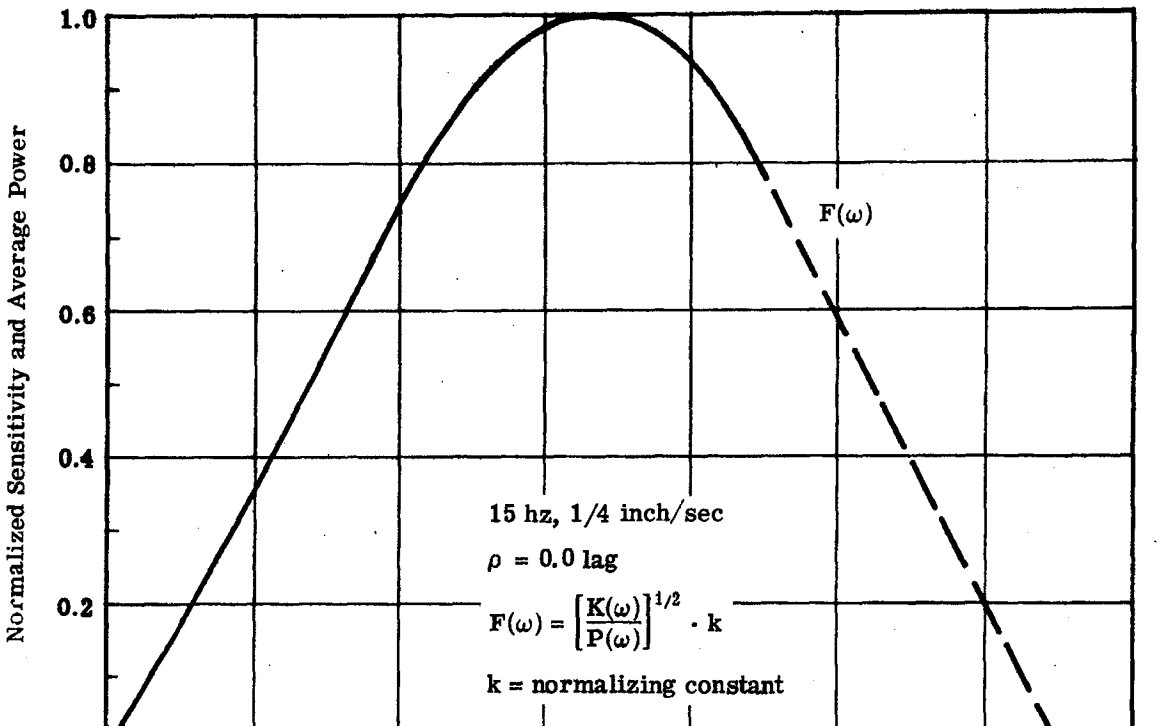

Fig. A-15 — AGC filter modifying average video as derived from fundamental and average video bandpass characteristics

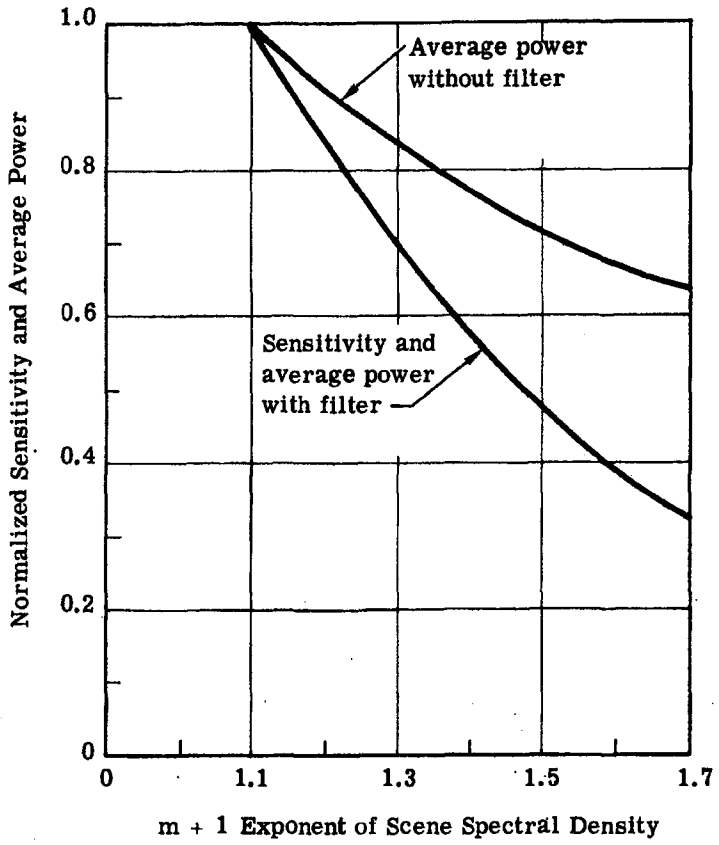

Fig. A-16 — Comparison of sensitivity and average power versus scene spectrum (0.0 lag factor)

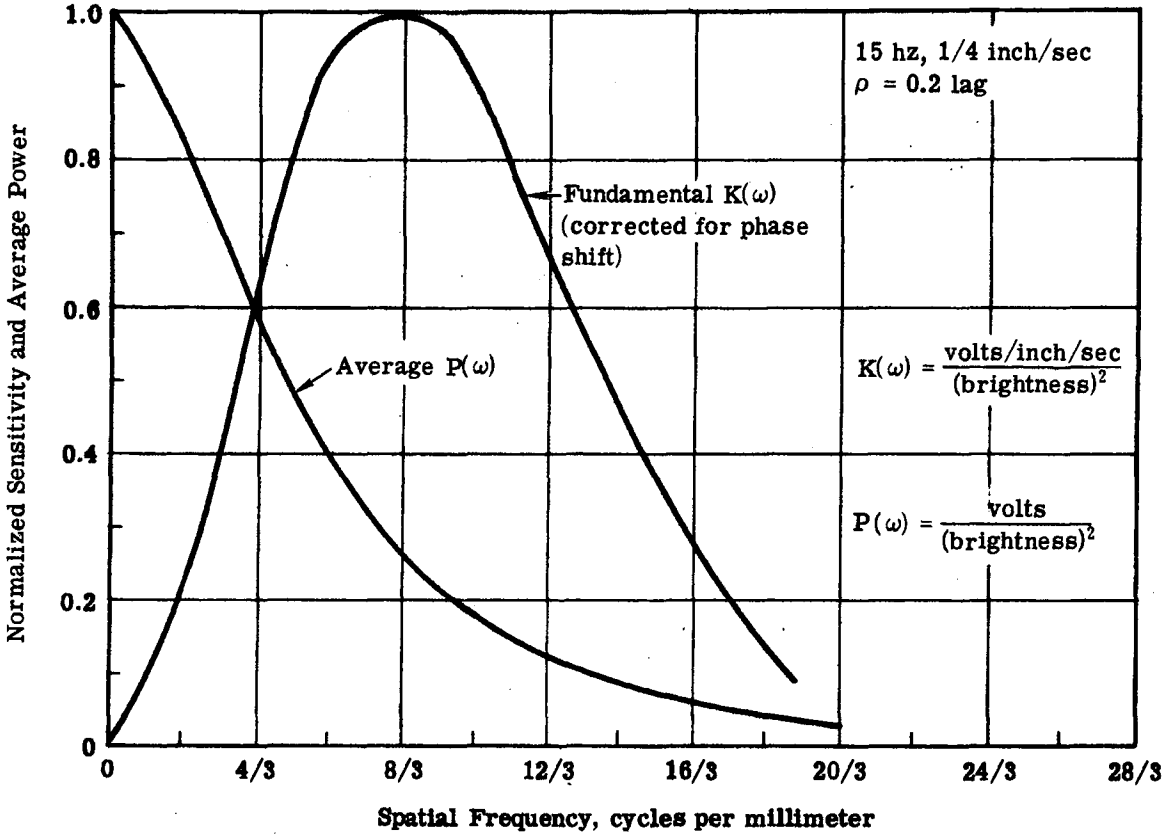

Fig. A-17 — Bandpass characteristics—fundamental component and average value (fundamental component corrected for phase shift)

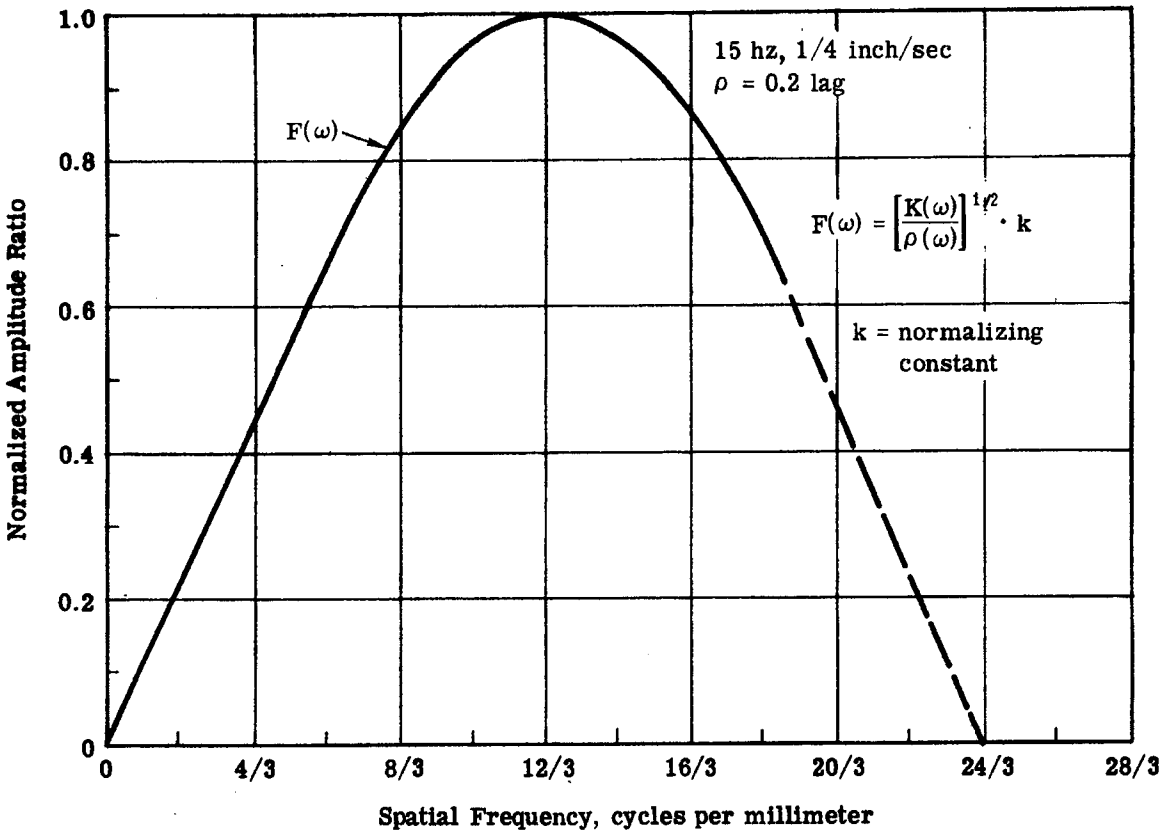

Fig. A-18 — AGC filter for 0.2 lag factor

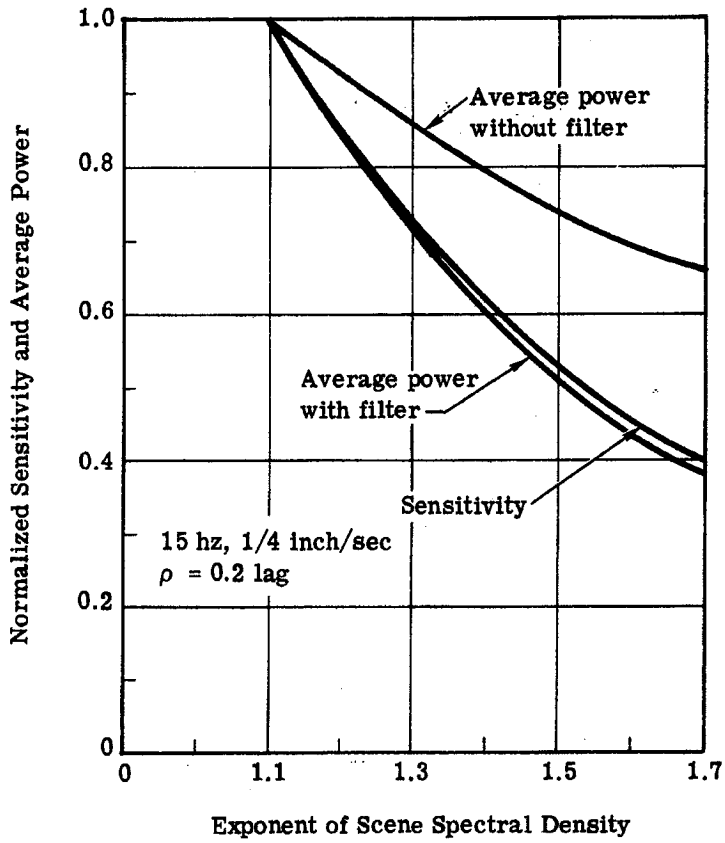

Fig. A-19 — Comparison of sensitivity and average power versus scene spectrum (0.2 lag factor)

BIF-059-4035-69

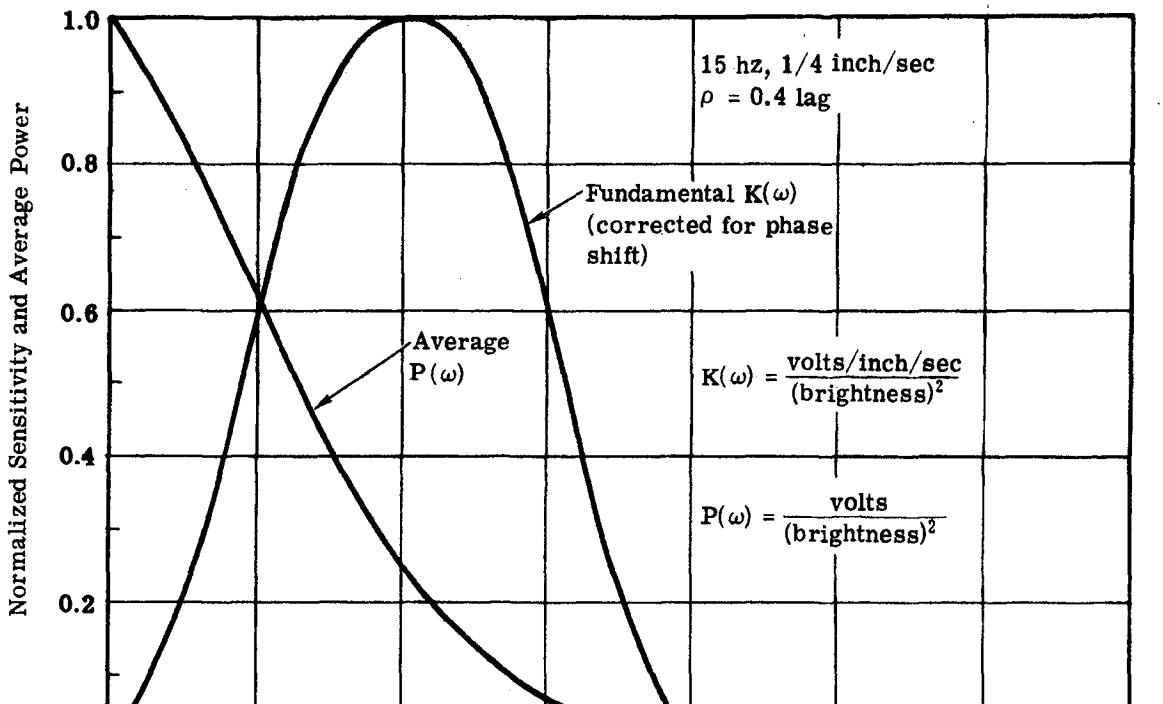

Fig. A-20 — Bandpass characteristics— fundamental component and average value (0.4 lag factor)

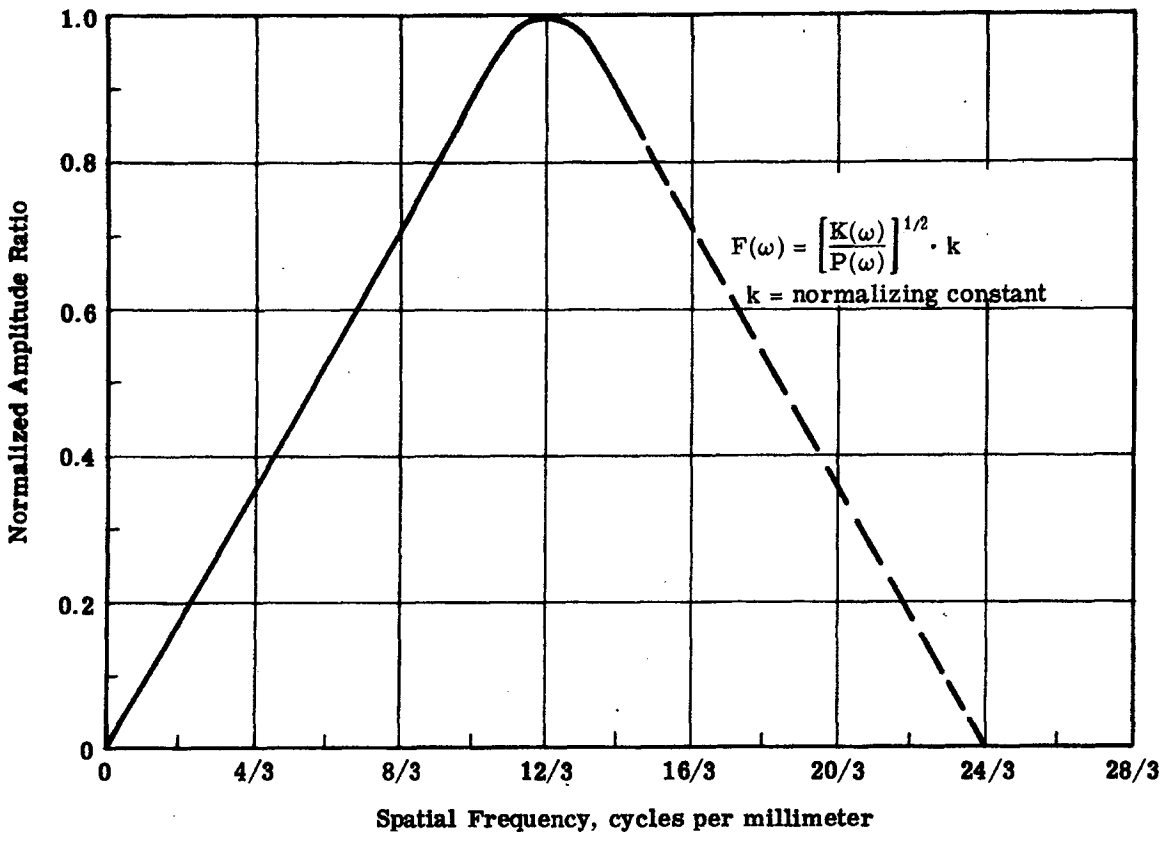

Fig. A-21 — AGC filter for 0.4 lag factor

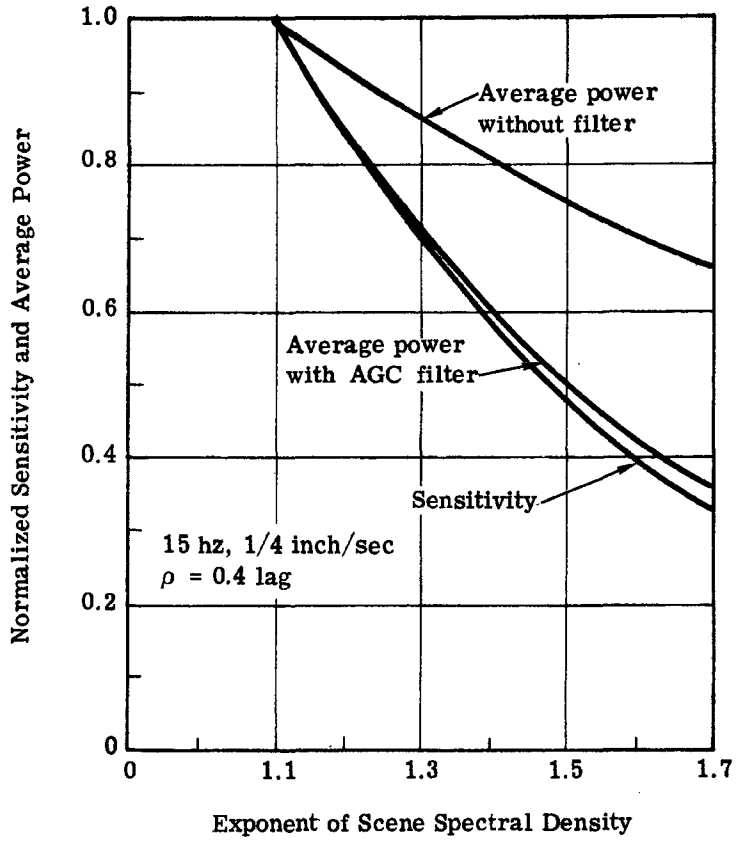

Fig. A-22 — Comparison of sensitivity and average power versus scene spectrum (0.4 lag factor)

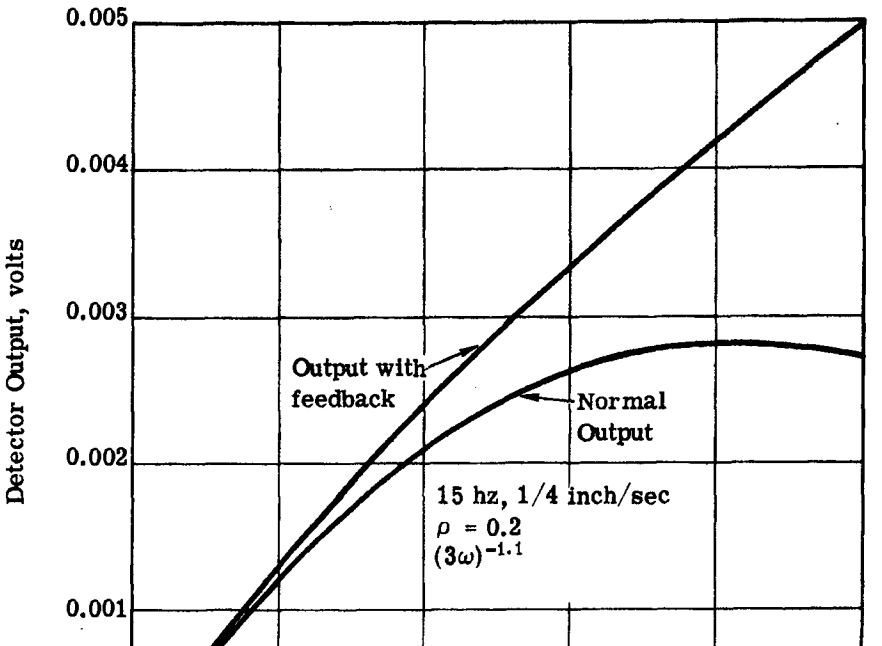

Fig. A-23 — Linearization and extended dynamic range with filtered average power—fundamental versus velocity ratio

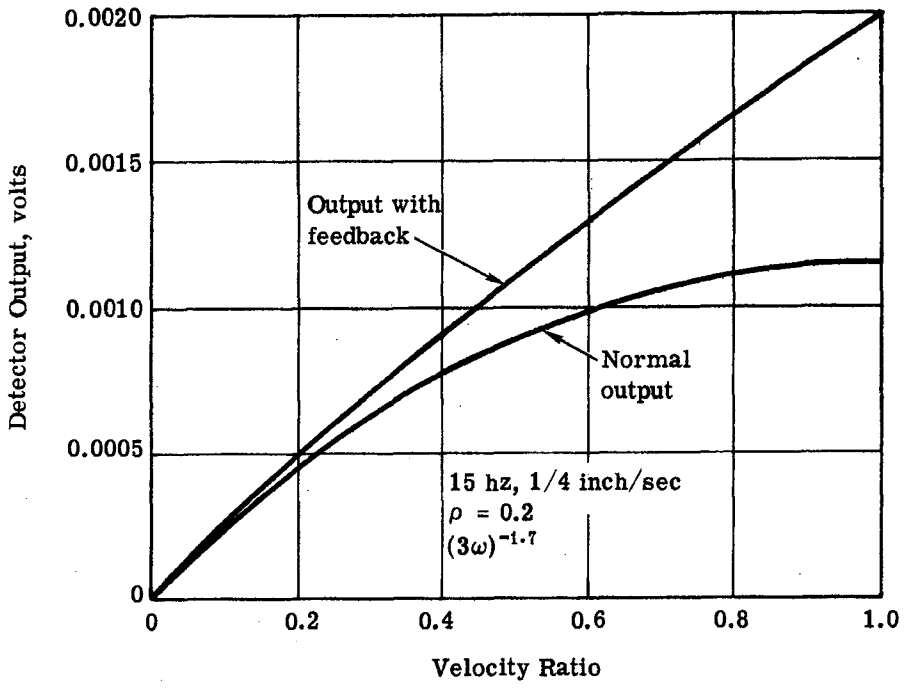

Fig. A-24 — Linearization—fundamental versus velocity ratio

This particular result should be investigated further both experimentally and with the mathematical model for the cases of 0 and 0.4 lag.

7. PHASE SHIFT WITH LAG AND SENSITIVITY

Because the phase of the fundamental shifts with lag and, the output stage of the sensor is a phase sensitive detector (PSD) (whose gain decreases as the input signal becomes out of phase with the driving reference voltage) comparisons of PSD outputs under various conditions of reference voltage settings and lag were made.

For this comparison, data generated at 15-hz and 1/4-inch-per-second modulation and an average input scene spectrum of 1.5 were used for the cases of 0.0, 0.2, and 0.4 lag.

Fig. A-25 is a plot of the integrated output over all spatial frequencies for a real scene spectrum of 1.5 for constant values of lag. It is assumed that the reference voltage to the phase sensitive detector is adjusted for each value of lag to optimize the output. It can be seen that the linear range of operation decreases with lag and the sensitivities near null are approximately equal.

Fig. A-26 is a similar plot of integrated output over all frequencies with the reference voltage set to optimize the output for zero lag only. Therefore, the outputs for ρ = 0.2 and 0.4 have been decreased correspondingly by the cosine of the relative phase shift. The linear range of operation is not changed but the sensitivity is decreased for increasing lag.

In Fig. A-27 the reference voltage has been set to optimize the output for 0.4 lag. Therefore, the outputs for ρ = 0.0 and 0.2 have been correspondingly decreased by the cosine of the relative phase shift. Again the linear range of operation has not been affected for any of the values of lag. However, it is observed that the sensitivity of the zero lag has been reduced below that of the 0.2 and the 0.4 lag.

8. DETECTION

8.1 Linear Detection

In the mathematical model, a square law characteristic had been assumed for the video detector as a mathematical simplification. In practice it is difficult to achieve a square law detector which will perform as such over a wide range of input signals, and consequently a linear detector is used.

In order to resolve some of the questions concerning possible relative advantages and disadvantages of each type of detector, a computer run was made with the following modification to simulate performance with a linear detector.

It is shown by Davenport and Root* that the average output of a linear detector is proportional to the standard deviation of the input where the input has a Gaussian probability density function.

The density function of video signals of a scene may well be approximated by a Gaussian function and, therefore, the mathematical model was modified to provide a detector output proportional to the standard deviation of the input.

---

*Davenport, and Root, "Random Signals and Noise," pp. 267-269.

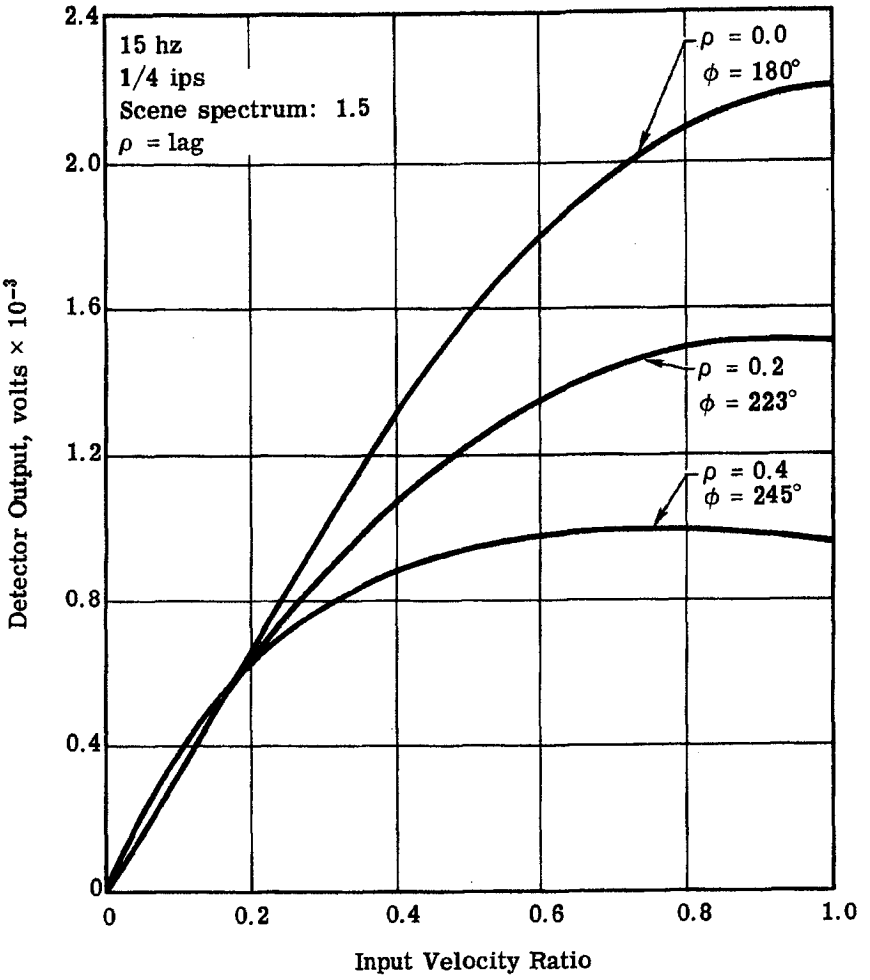

Fig. A-25 — Integrated output for 1.5 real scene spectrum (0.0, 0.2, and 0.4 lag factors)

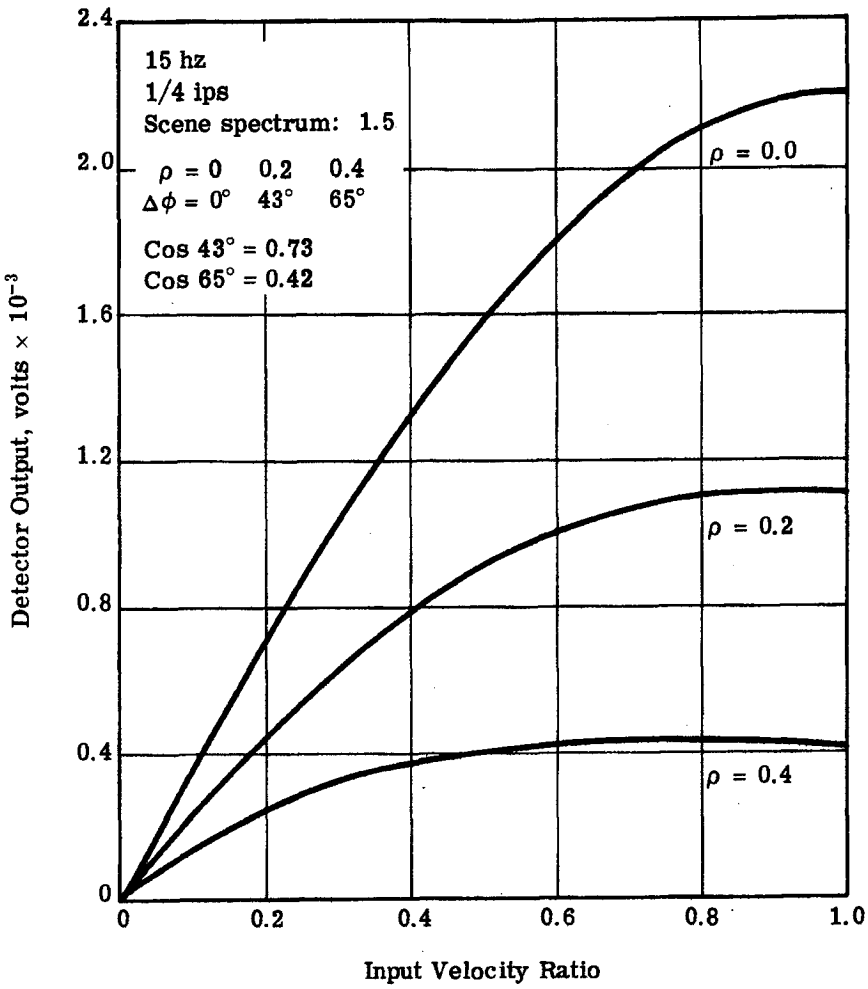

Fig. A-26 — Integrated output for 1.5 real scene spectrum, optimized for 0.0 lag factor

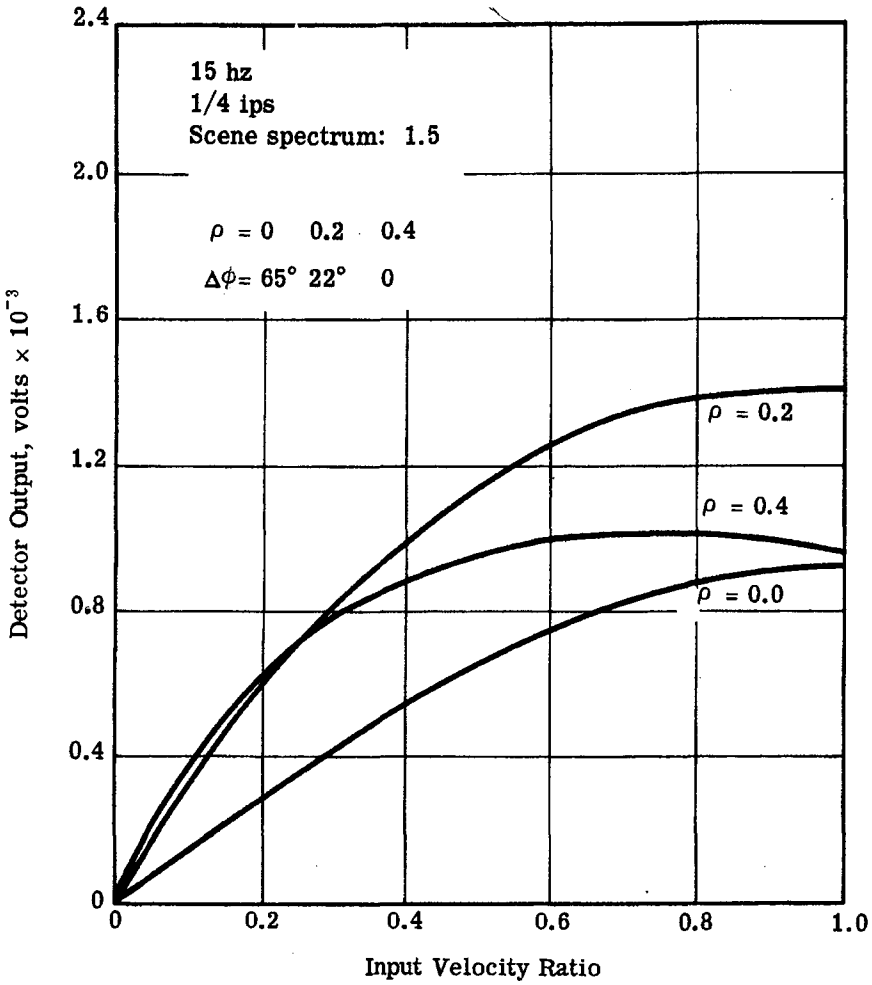

Fig. A-27 — Integrated output for real scene spectrum, optimized for 0.4 lag factor

Since, in the square law detector case, the instantaneous power into the detector was calculated throughout a modulation cycle, summed over all spatial frequencies for a particular input velocity, the standard deviation could be obtained simply by taking the square root of the power. For real scene inputs and with lag equal to zero, such a computer run was made and the detector output was then harmonically analyzed to determine the average output, the fundamental and its harmonics.

Some results of this run are shown in Figs. A-28, A-29, and A-30. The general character of the curves has not changed from that of the square law case except for changes in the ordinate scales.

It is interesting to note the behaviour of the second harmonic and the average output with velocity for purposes of an AGC signal as described in Sections 6.1 and 6.2. Similar to the results of the square law case, the average detector output is much more uniform with velocity than the second harmonic and would, therefore, seem to be much better to utilize for AGC.

Table A-1 gives a comparison of some essential characteristics between the linear and the square law detectors.

The following observations are made:

1. The square law gives approximately 2× the percent modulation of the linear for a given scene and input velocity.
2. The square law detector gives 1.0 to 1.5× the sensitivity of the linear detector depending on the scene, i.e., the factor increases with decreasing exponent of scene spectrum.
3. The linear detector shows slightly less change in sensitivity for given change in scene, i.e.:

   a. Linear 2.4:1 1.1 to 1.7 scene
   b. Square law 2.8:1 1.1 to 1.7 scene

4. The average output of the square law detector is approximately equal to the square of the average output of the linear detector.

8.2 Detector Theory

Several relationships can be derived by comparing linear and square law detectors.

The output of a square law detector is proportional to the input power, $y = kx^2$. From the mathematical model, the output of the sensor under normal operation using a square law detector with a real scene input and at some constant input velocity is harmonically analyzed into its components. Referring the sensor output through the detector gain, to the input of the detector i.e., average power into the detector, the components of the video power have the following form:

$$D_{i_{\text{Sq. law}}}(t) = a_0 + a_1 \sin \omega_M t + a_2 \sin 2\omega_M t + \ldots = \sum_n a_n e^{j\omega nt} \qquad \text{(A.1)}$$

where $D_{i_{\text{Sq. law}}}(t)$ = square law detector input (video power through a modulation cycle)

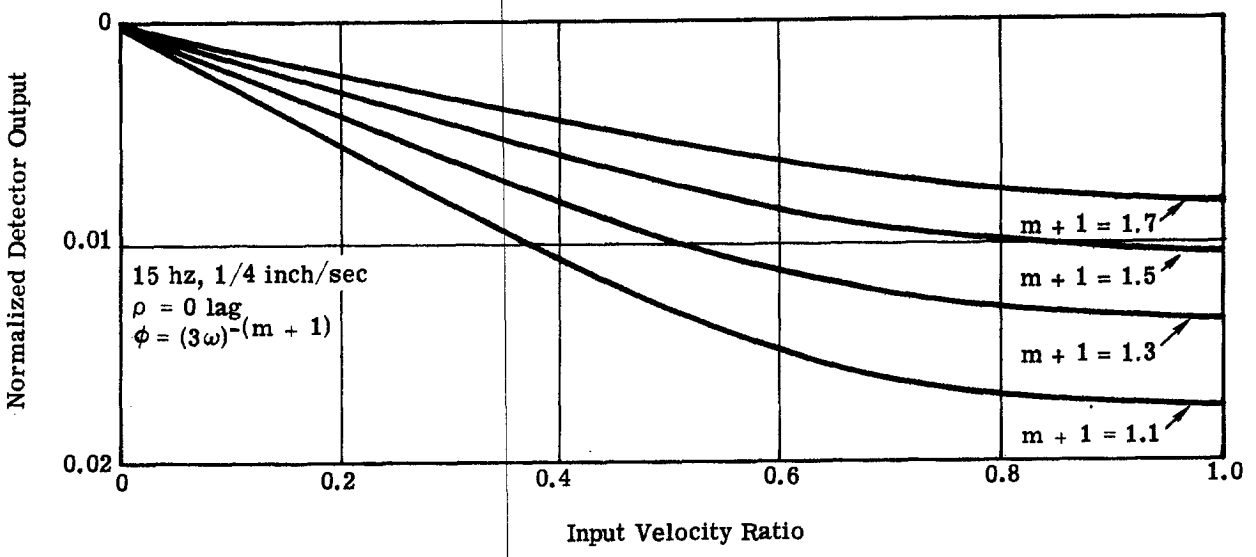

Fig. A-28 — Linear detector—fundamental versus input velocity ratio

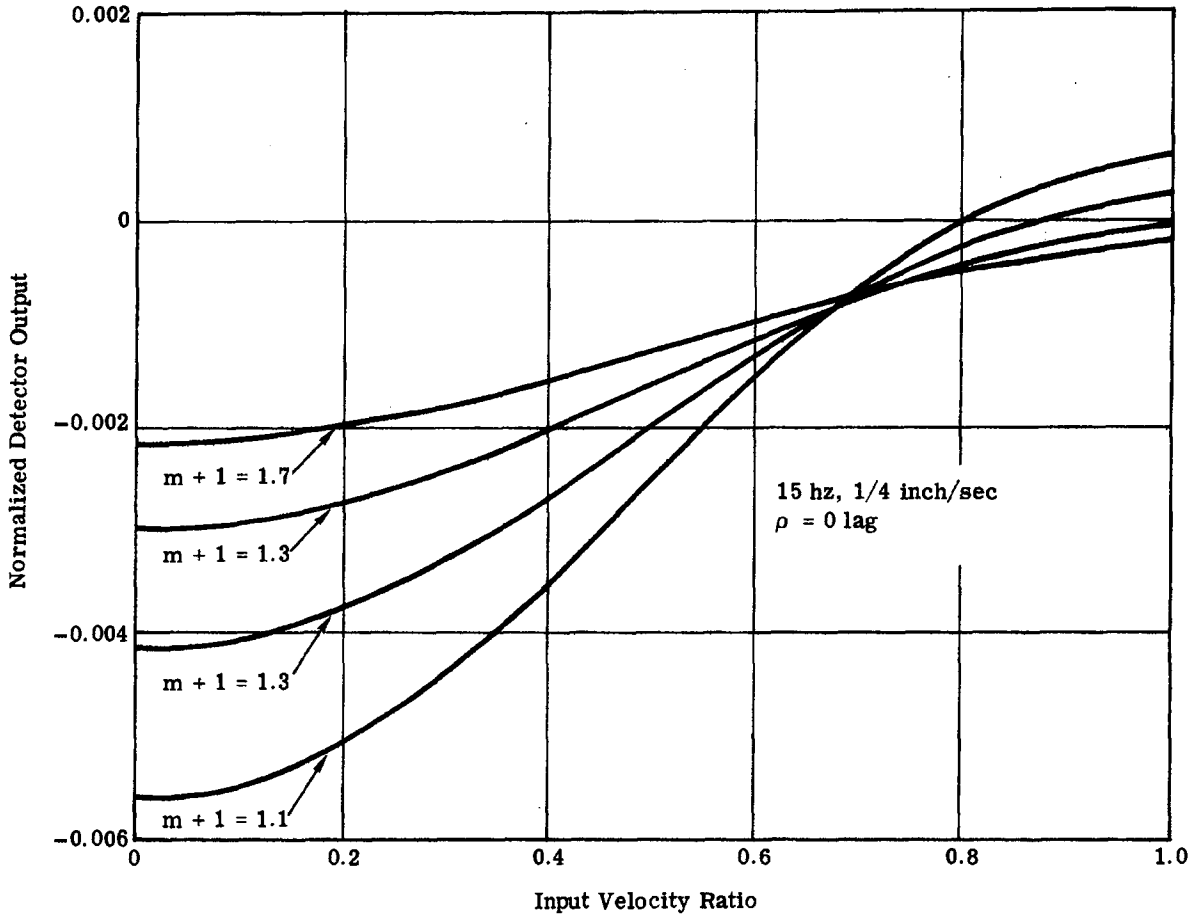

Fig. A-29 — Linear detector—second harmonic versus input velocity ratio

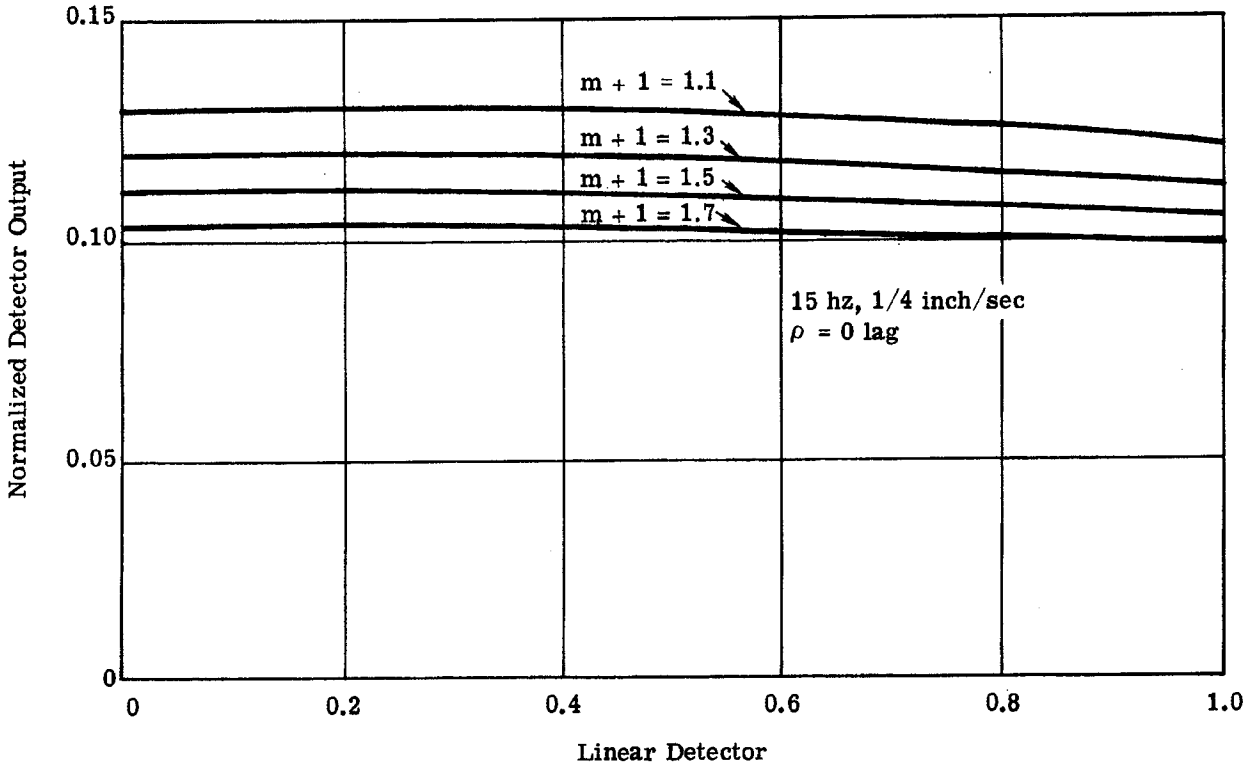

Fig. A-30 — Linear detector—average output versus input velocity ratio

Table A-1 — Comparison of Linear and Square Law Detectors

	Linear				Square Law		
Scene	Sensitivity K_{lin} v/in./sec	Average P_{lin}	M_{lin}/v Percent Modulation/ milli-in./sec	2 K_{lin} P_{lin}	Sensitivity $K_{sq\ law}$ v/in./sec	Average $P_{sq\ law}$	$M_{sq\ law}/v$ Percent Modulation/ milli-in./sec
1.1	0.58	0.74	0.078	0.86	0.87	0.55	0.16
1.3	0.44	0.68	0.065	0.60	0.60	0.46	0.13
1.5	0.32	0.62	0.052	0.40	0.42	0.40	0.11
1.7	0.24	0.58	0.041	0.28	0.31	0.35	0.089

Note: $M_{sq\ law} = 2\ M_{lin}$

$P_{sq\ law} = P_{lin}^2$

$K_{sq\ law} = 2\ K_{lin}\ P_{lin}$

The a_0 term is the average power in the ac video signal and does not include any dc power associated with the average brightness of a scene.

In Section 8, the output of a linear detector was described as proportional to the standard deviation of the input which can be described by a Gaussian density function. Therefore, for the sensor with a real scene input (approximately Gaussian) and using a linear detector, the output will be proportional to

$$D_i(t) = \sqrt{D_i(t)}$$
$$\text{Linear} \quad \text{Sq. law}$$

$$= (a_0 + a_1 \sin \omega_M t + a_2 \sin 2\omega_M t + \ . \ . \ .)^{1/2} \tag{A.2}$$

$$= \left(\sum_n a_n e^{j\omega nt} \right)^{1/2}$$

where $D_i(t)$ = input to linear detector (rms level of the video signal through a modulation cycle)
Linear

Again the mathematical model shows that the harmonic analysis of the linear detector output can be broken down into similar components, i.e.,

$$D_i(t) = b_0 + b_1 \sin \omega_M t + b_2 \sin 2\omega_M t +$$
$$\text{Linear}$$

$$= \sum_n b_n e^{j\omega nt} \tag{A.3}$$

Since $D_i^2(t) = D_i(t) =$
$\text{Linear} \quad \text{Sq. law}$

$$\left(\sum_n b_n e^{j\omega nt} \right)^2$$

an expansion of the above is equal to the following

$$D_i(t) = \left(\sum_n b_n e^{j\omega nt} \right)^2 = b_0^2 + 2b_0 b_1 \sin \omega_M t + 2b_0 b_2 \sin 2\omega_M t + \ . \ . \ .$$
$$\text{Sq. law}$$

$$+ b_i^2 \sin^2 \omega_M t + b_2^2 \sin^2 2\omega_M t + \ . \ . \ . \tag{A.4}$$

$$+ \text{cross product terms}$$

Equating similar terms in Equations (A.1) and (A.4)

$$a_0 = b_0^2 \tag{A.5}$$

$$a_1 = 2b_0\, b_1$$

$$a_2 = 2b_0\, b_2 \tag{A.6}$$

. .
. .
. .

From Equation (A.5) it is seen that the average rms input to the linear detector, b_0, is equal to the square root of the average video power into the square law detector.

Also, percent modulation of the fundamental is defined as

$$M_1 = \frac{a_1}{a_0}$$

and

$$N_1 = \frac{b_1}{b_0}$$

respectively for the square law and linear detectors. Dividing Equation (A.6) by Equation (A.5)

$$M_1 = \frac{a_1}{a_0} = \frac{2b_1}{b_0} = 2N_1 \tag{A.7}$$

Therefore, the percent modulation at a given input velocity for a square law detector is twice as great as that for a linear detector.

8.3 Percent Modulation of Image Motion MTF

Similar to the data in Figs. A-11 and A-14 for zero lag (and also for lag not equal to zero), a set of plots characteristic of the image motion, modulation transfer function (MTF) can be obtained from the mathematical model. This is accomplished by setting the lens, vidicon and amplifier transfer functions equal to unity for a discrete frequency analysis. The harmonic analysis of the output would give the Fourier series components of the amplitude of the $|MTF|^2$ for the square law detector as a function of spatial frequency and input constant velocity for a given frequency and peak velocity of image modulation. Therefore, the periodic variation in the $|MTF|^2$ can be represented by its Fourier components

$$|MTF|^2(t) = |\overline{MTF}|^2 [1 + m_1(\omega,v) \sin \omega_M t + m_2(\omega,v) \sin 2\omega_M t + \ldots]$$
Motion

$$\omega = \omega_n$$
$$v = v_m \qquad \text{(A.8)}$$

where $|\overline{MTF}|^2$ = average value of $|MTF|^2$ for $v = v_m$ and $\omega = \omega_n$
$m_1(\omega,v)$ and $m_2(\omega,v)$ = percent modulation of $|\overline{MTF}|^2$ at the fundamental and second harmonic frequencies respectively for $v = v_m$ and $\omega = \omega_n$

The fundamental component of the input power to the square law detector for a given input constant velocity is given by the following:

$$a_1 = \int \phi(\omega_x)\, m_1(\omega,v)\, |\overline{MTF}|^2(\omega,v)\, |MTF|^2_{\substack{\text{Lens}\\\text{Vid}\\\text{Amp}}}\, d\omega \Big|_{v = v_n} \qquad \text{(A.9)}$$
Motion

where a_1 = amplitude of fundamental component of video power [see Equation (A.1)]

$\phi(\omega)$ = Wiener spectrum of input scene

$|MTF|^2_{\substack{\text{Lens}\\\text{Vid}\\\text{Amp}}}$ = combined product, squared, of the lens, vidicon and amplifier modulation transfer functions

Over the linear region of operation where the signal is proportional to the input velocity (see Fig. A-11), the percent modulation is proportional to the input velocity, i.e.:

$$m_1(\omega,v) = v\, m_1(\omega)$$

and

$$m_1(\omega) = \frac{m_1(\omega,v)}{v} \quad \frac{\text{percent modulation}}{\text{input velocity}} \qquad \text{(A.10)}$$

Therefore, the total sensitivity if given by

$$K_{\substack{\text{Sq law}\\\text{total}}} = \frac{a_1}{v} = \int \phi(\omega)\, m_1(\omega)\, |\overline{MTF}|^2_{\text{Motion}}\, |MTF|^2_{\substack{\text{Lens}\\\text{Vid}\\\text{Amp}}}\, d\omega \qquad \text{(A.11)}$$

The sensor bandpass characteristic for the fundamental component is given by (see Fig. A-14)

$$K(\omega)_{\text{Sq law}} = m_1(\omega)\, |\overline{MTF}|^2_{\text{Motion}}\, |MTF|^2_{\substack{\text{Lens}\\\text{Vid}\\\text{Amp}}} \qquad \text{(A.12)}$$

and the total sensitivity in terms of the bandpass characteristic is

$$K_{\substack{\text{Sq law} \\ \text{total}}} = \int \phi(\omega)\, K(\omega)_{\text{Sq law}}\, d\omega \tag{A.13}$$

Similarly the average, video ac power, a_0, at some input velocity v_n, is given by the following:

$$a_0 = \int \phi(\omega)\, |\overline{MTF}|^2_{\text{Motion}}(\omega,v)\, |MTF|^2_{\substack{\text{Lens} \\ \text{Vid} \\ \text{Amp}}}\, d\omega \Big|_{v = v_n} \tag{A.14}$$

As mentioned in Section 6.1, the average video power is approximately constant over the linear region of operation and therefore,

$$|\overline{MTF}|^2\,(\omega,v) \approx |\overline{MTF}|^2(\omega) \tag{A.15}$$

i.e., independent of input velocity

Setting the bandpass characteristic for the average video power equal to (see Fig. A-14)

$$P(\omega) = |\overline{MTF}|^2_{\text{Motion}}(\omega)\, |MTF|^2_{\substack{\text{Lens} \\ \text{Vid} \\ \text{Amp}}} \tag{A.16}$$

and therefore,

$$a_0 = \int \phi(\omega)\, P(\omega)\, d\omega \tag{A.17}$$

Similar equations can be developed for the linear detector. Whereas the input average powers of the various input spatial frequencies are additive for the case of the square law detector, the output of the linear detector is not equal to the sum of amplitudes of the input frequencies. To see what the average rms and the amplitude of the fundamental component of the rms variation of the video signal is, turn to Equations (A.5) and (A.6).

The average for the linear detector is given by

$$b_0 = (a_0)^{1/2} = \left[\int \phi(\omega)\, P(\omega)\, d\omega\right]^{1/2} = P_{\text{Linear}} \tag{A.18}$$

and the fundamental is given by

$$b_1 = \frac{a_1}{2b_0} = \frac{V \int \phi(\omega)\, K(\omega)_{\text{Sq law}}\, d\omega}{2\left[\int \phi(\omega)\, P(\omega)\, d\omega\right]^{1/2}} \tag{A.19}$$

where $K(\omega)_{\text{Sq law}}$ and $P(\omega)$ are defined by Equations (A.12) and (A.16).

From Equation (A.19), the total linear detector sensitivity is

$$K_{\substack{\text{Linear}\\\text{total}}} = \frac{b_1}{v} = \frac{\int \phi(\omega)\, K(\omega) \quad d\omega}{2[\int \phi(\omega)\, P(\omega)\, d\omega]^{1/2}} \quad \text{Sq law} \tag{A.20}$$

and the relationship between the square law and the linear sensitivity is given by

$$K_{\substack{\text{Sq law}\\\text{total}}} = 2K_{\substack{\text{Linear}\\\text{total}}} P_{\text{Linear}} \tag{A.21}$$

Referring back to Table A-1, we can see the very close agreement as established by Equation (A.21) over a range of input scene spectrum.

It can also readily be shown that the following relationship between the percent modulation per constant input velocity exists:

$$\frac{N_1}{V} = \frac{K_{\substack{\text{Linear}\\\text{total}}}}{b_0} = \frac{1}{2}\frac{K_{\substack{\text{Sq law}\\\text{total}}}}{a_0} = \frac{1}{2}\frac{M_1}{V} \tag{A.22}$$

i.e., the percent modulation per unit input velocity for the linear detector equals one half that for the square law detector.

Again referring to Table A-1, we see the very close agreement where in the table the symbolism

$$M_{\text{Linear}} = N_1$$

and

$$M_{\text{Sq law}} = M_1$$

is used.

8.4 AGC Filter With Linear Detector

In Section 6.1 a scheme for AGC is proposed using the average value of video power together with a filter such that the bandpass characteristic of the average is made identical to the bandpass characteristic of the signal component. Thus, any changes in the scene spectrum produce identical changes in the magnitudes of the average and the signal component. The level of the average power can be used to control the gain of an amplifier in the signal channel such that the overall gain is reasonably independent of changes in the scene. The filter characteristics required were derived for a square law detector.

The same reasoning can be used to derive a filter for use with a linear detector and it is of interest to determine whether the filters are different or the same depending on the detector used.

Because of the form of the equation for the total sensitivity and the average power as given by Equations (A.18) and (A.20) for the linear detector case, it is not immediately apparent how to determine the filter characteristics directly from the ratio of the bandpass characteristics for the sensitivity and the average as was done for the square law case. Therefore, a somewhat different approach has to be taken.

A similar AGC criterion is that the percentage change in sensitivity due to the scene spectrum be equal to the percentage change in the average, i.e.,

$$\frac{\Delta K_{\substack{\text{Linear}\\\text{total}}}(\phi)}{K_{\substack{\text{Linear}\\\text{total}}}(\phi)} = \frac{K_{\substack{\text{Linear}\\\text{total}}}(\phi_1) - K_{\substack{\text{Linear}\\\text{total}}}(\phi_2)}{K_{\substack{\text{Linear}\\\text{total}}}(\phi_1)} = \delta \tag{A.23}$$

and

$$\frac{\Delta P_{\text{Linear}}(\phi)}{P_{\text{Linear}}(\phi)} = \frac{P_{\text{Linear}}(\phi_1) - P_{\text{Linear}}(\phi_2)}{P_{\text{Linear}}(\phi_1)} = \delta$$

This is equivalent to determining under what conditions the following can be made to hold:

$$\frac{K_{\substack{\text{Linear}\\\text{total}}}(\phi_2)}{K_{\substack{\text{Linear}\\\text{total}}}(\phi_1)} \stackrel{?}{=} \frac{P_{\text{Linear}}(\phi_2)}{P_{\text{Linear}}(\phi_1)} \tag{A.24}$$

By substituting Equations (A.18) and (A.20) into Equation (A.24) this reduces to the following form:

$$\frac{\int \phi_2(\omega)\, K(\omega)_{\text{Sq law}}\, d\omega}{\int \phi_1(\omega)\, K(\omega)_{\text{Sq law}}\, d\omega} \stackrel{?}{=} \frac{\int \phi_2(\omega)\, P(\omega)\, d\omega}{\int \phi_1(\omega)\, P(\omega)\, d\omega} \tag{A.25}$$

The ratios of both sides of this equation will be equal if the bandpass characteristic of $P(\omega)$ is the same as $K(\omega)_{\text{Sq law}}$ to within a constant multiplier: i.e.,

$$P(\omega) = \alpha\, K(\omega)_{\text{Sq law}} \tag{A.26}$$

This will be true if $P(\omega)$ is filtered such that

$$P(\omega)\, |MTF|^2_{\text{Linear}} = \alpha\, K(\omega)_{\text{Sq law}} \tag{A.27}$$

and

$$|MTF|_{\text{Linear}} = \left[\frac{K(\omega)_{\text{Sq law}}}{P(\omega)}\right]^{1/2} k \tag{A.28}$$

where k = a normalizing constant

This is identical to the filter characteristics derived in Section 6.1. Therefore, the filter required to provide an average signal suitable for AGC purposes using a linear detector is identical to that required for use with a square law detector.

9. COMPUTER PROGRAM DESCRIPTIONS

There have been a number of programs written in connection with the computer studies of the image velocity sensor. A brief description of each program, including a definition of the input quantities and the form of the output, is given below. The programs break down into three major groups:

1. Programs for generating the image motion MTF's which also include a program for plotting
2. Programs for supplying the point-wise products over frequency of the lens and vidicon MTF's
3. A harmonic analysis of the sensor output.

9.1 Image Motion MTF's

Program 9.1-1

A family of image motion MTF's is generated by this program as a function of the modulation frequency, the peak modulation velocity, and the input constant velocity. Since the period of modulation is longer than the exposure time, i.e., the period of one complete scan of the vidicon raster, this gives rise to a family of time-varying MTF curves which are periodic with the modulation cycle. The complex amplitudes are given.

Output. Twelve blocks of nine MTF's are written on disc number 12. Each block represents a different ground scene linear velocity. The nine subdivisions in each block are various time samples of the motion MTF during the first half cycle of motion. The last half cycle is built from the first by reflection about the midline.

Inputs. The inputs for the family of image motion MTF's are as follows:

IMTF	An integer denoting the total number of points used in frequency space
ZEROMTF	Frequency value used to normalize the frequency scale to unity. This has been the same as WU below.
WL	Smallest value of frequency used in the analysis.
WU	Largest value of frequency
IFIX	Integral number of points on the displacement curve of motion
IFID	Integral number of velocity to be considered, i.e., total number of blocks
ISBOFF, IDUMP	Not presently used

FREQC	Cycles per second modulation
VSEE	VSEE is the maximum modulation velocity in inches per second
STARTM	Total number of starts in frequency space. This value is always 16.
ISW	Lower velocity start index
IM3	Number of points to be omitted when starting in MTF of 3.75 cycles per second modulation frequency
IM7	Number of points to be omitted when starting an MTF of 7.50 cycles per second modulation frequency
IM15	Number of points to be omitted when starting an MTF of 15.0 cycles per second modulation frequency.

Program 9.1-2

This program, including the readin parameters and the output, is the same as program 1 except that it provides the square of the absolute value of the complex amplitude.

Program 9.1-3

This program was written to plot the 12 families of nine image motion MTF's. The added option of vidicon retension lag is available so one can see the degradation effect of imperfect erase on the vidicon face. The readin parameters have been described above and the system was written for the MSOS CDC system. However, it needs revision in order to be used on the current master system used at Itek. The storage medium used is tape, not disc so this would also need changing for use with programs 9.1-1 and 9.1-2.

9.2 Product-Lens and Vidicon MTF's

Program 9.2-1

This program provides the point-wise product over frequency of the amplitudes of the lens and vidicon, given the coefficients of a polynomial fit to their respective response curves.

Output. Program 9.2-1 writes five blocks of binary information on disc unit number 12. The first array is reserved for future use. Presently it is a flat Wiener spectrum. Array two is the point-wise product over frequency space of the lens and vidicon. Array three is frequency. These equally spaced points represent the independent variable used in the four other arrays. Arrays numbered four and five are the vidicon and lens MTF's, respectively.

Inputs. The inputs for program 9.2-1 are as follows:

IMTF	An integer denoting the total number of points used in frequency space
WL	Smallest value of frequency used in the analysis
WU	Largest value of frequency

ZEROMTF	Frequency value used to normalize the frequency scale to unity. This has been the same as WU.
PHA	Time reference for motion MTF's
IPOLY	Order of polynominal used to fit the lens and vidicon MTF's
KB	Integral logical unit number
SCALE	Percentage degradation of the lens MTF
LENS DATA	Fit number 1 supplies a polynomial fit to the lens and vidicon MTF data. The coefficients of these polynominals are read in as lens and vidicon data.
VIDICON DATA	Described above.

Program 9.2-2

This program is similar to program 9.2-1 except that it provides the amplitude squared of the point-wise products of the lens and vidicon. The inputs and outputs are the same.

Program 9.2-3

This program is similar to program 9.2-2 with the addition of the AGC filter MTF curve. The inputs and outputs are the same with the following exceptions:

Output. Block one is now the AGC filter. Block two is the point-wise product over frequency of the amplitude squared of the lens, vidicon, and AGC filter.

Input. AGC data; fit number 3 supplies a polynomial fit to the AGC filter. The coefficients of the polynomial are read in.

9.3 Harmonic Analysis

The harmonic analysis program calculates the integral of the point-wise product over frequency of the squared amplitudes of the lens, vidicon, image motion, and scene spectrum MTF's. The squared amplitudes give the total average video power into a square law detector. Since there are a family of time varying image motion MTF's throughout a modulation period for each value of input constant velocity and a given modulation frequency, there are a corresponding number of integrations performed. The integrations over a family of image motion MTF's for a given input constant velocity constitute a periodic time function of the detector output. A harmonic analysis of the output provides a 1:1 correspondence between the output Fourier series components and the input constant velocity together with the other input conditions, i.e., modulation frequency, peak modulation velocity, input scene spectrum, and the lens and vidicon MTF's.

The lens and vidicon MTF's and the image motion MTF's are stored on disc number 12 and are available for use by the harmonic analysis.

Since the real scene spectrum can be expressed as an analytic function, this program generates its own real scene spectrum by specification of the required (m + 1) exponent.

Also, the effect of vidicon lag is accounted for in this program. By specifying the value of lag (rho), i.e., the residual exposure function after scan, as one of the input parameters, the program vectorially adds the complex amplitudes of suitable sequences of image motion transfer functions of program 9.1-1, and provides the amplitude squared versus spatial frequency to form the new image motion MTF with lag.

Program 9.3-1

This program simulates a sensor with a square law detector. As described above, it has the options of different real scene spectra and various values of vidicon lag. It is presently set to operate for a modulation frequency of 15 hz but it can be modified to run at 7.5 and 3.75 hz.

Output. For each value of input constant velocity, the average value and the amplitude and phase of the first, second, third, and fourth harmonics are printed out.

Inputs. The inputs for program 9.3-1 are as follows:

IWUPP	Integral number of points in frequency space
IHAR	One more than the highest harmonic considered
WLOW	If we block dc, the lowest frequency value is not zero but WLOW
IUMTF	Integral value of upper frequency considered. This and the previous input allow narrow bandpass analysis.
IFID	As explained in program 9.1-1
ILENS	One, if we only want the lens MTF, otherwise zero
IVID	One, if we only want the vidicon MTF, otherwise zero
ISPEC	One, if we want a real scene spectrum, otherwise zero
IFLT	One, if we want a complete system, otherwise zero
WL2	Frequency increment
ILOOP	Number of complete times the program will be repeated
ROE	Value of retension on the vidicon face
EP	Exponent for the real scene spectrum
B and BOA	Two arrays from fit number 2 which represent the vidicon surface.

Program 9.3-2

This program performs the same analysis with the same inputs and outputs as program 9.3-1 except that it is a discrete frequency instead of a continuous frequency analysis. This is

accomplished by letting all the motion MTF values equal zero except the value at the frequency desired. As the frequency points are 1/3 cycle apart, only system response at these values is possible.

Program 9.3-3

This program performs the same analysis as program 9.3-1 except that the modulation frequency is 7.5 hz instead of 15 hz.

Program 9.3-4

This program performs the same analysis as program 9.3-2 except that the modulation frequency is 7.5 hz instead of 15 hz.

Program 9.3-5

This program simulates sensor performance with a linear detector. It uses the same inputs as program 9.3-1 and has the same outputs. The linear detector output is obtained by taking the square root of the time signal before harmonic analysis. The image motion and lens-vidicon MTF's are supplied by the squared amplitude programs 9.1-2 and 9.2-2, respectively. Therefore, the analysis can only be run for the condition of zero lag.

Program 9.3-6

This program performs the same analysis with the same inputs and outputs as program 9.3-5 except that it is a discrete frequency analysis. This is accomplished by letting all the motion MTF values equal zero except the value at the frequency desired. As the frequency points are 1/3 cycle apart, only system response at these values is possible.

Appendix B

HELIUM TEST

1. TEST DESCRIPTION AND RESULTS

In order to assess the deteriorating effect of helium on vidicon performance, the following test was performed. A television camera, without special protective modifications and enclosed in a helium environment, was viewing a TV resolution chart through a window (see Figs. B-1 and B-2). The camera system used in the test was an RCA PK301 camera with an 8134 vidicon. The camera was operated in the manual target mode.

During the test, the pressure in the test chamber was maintained between 1.0 and 2.5 psig and the temperature between 70 and 82 °F. Illumination for measurement purposes was 55 foot-candles at the target except as noted below. On 8 November, day 2 of the test, power cycling equipment was installed, and for the remainder of the test the system operated with a 25-minute on, 65-minute off power cycle.

The parameters measured periodically during the test included camera target voltage, average signal voltage, peak-to-peak signal voltage, peak-to-peak noise voltage, dark current voltage, and depth of modulation. All measurements were made using a Tektronix type 545A oscilloscope with a type 1A1 plug-in and an RCA type WV-98C VTVM. All data measured with the oscilloscope were preserved by means of oscilloscope photography.

During the first 8 days of the test, operation of the system was normal, and no significant changes were noted. All parameters remained approximately constant at the following levels: target voltage—35.2 volts; average signal—0.66 volt; peak-to-peak signal—0.70 volt; peak-to-peak noise—0.07 volt; dark current voltage—0.22 volt; depth of modulation—3 to 4 megacycles. The average signal-to-noise ratio over this period was 60 volts per volt and the TV resolution was approximately 400 lines.

On day 9 of the test, severe deterioration of system performance was noted. While there was no significant change in target voltage or in dark current voltage, the peak-to-peak noise increased to 0.08 volt and the signal voltage decreased to 0.30 volt, resulting in a signal-to-noise ratio of 22.5 volts per volt. The depth of modulation was reduced to 2 megacycles and the TV resolution was less than 200 lines. Reduction of target illumination at this time to 20 foot-candles resulted in improved operation, but previous levels of operation could not be restored.

On day 10 of the test, the system performance level was down to approximately 50 percent of the level of the previous day. The final data recordings taken were as follows: target voltage—35.7 volts; average signal—0.30 volt; peak-to-peak signal—0.12 volt; peak-to-peak noise—0.08 volt; dark current voltage—0.20 volt; depth of modulation—1 megacycle. The signal-to-noise ratio was 9 volts per volt and the TV resolution was less than 200 lines. Target illumination was 10 foot-candles.

BIF-059-4035-69

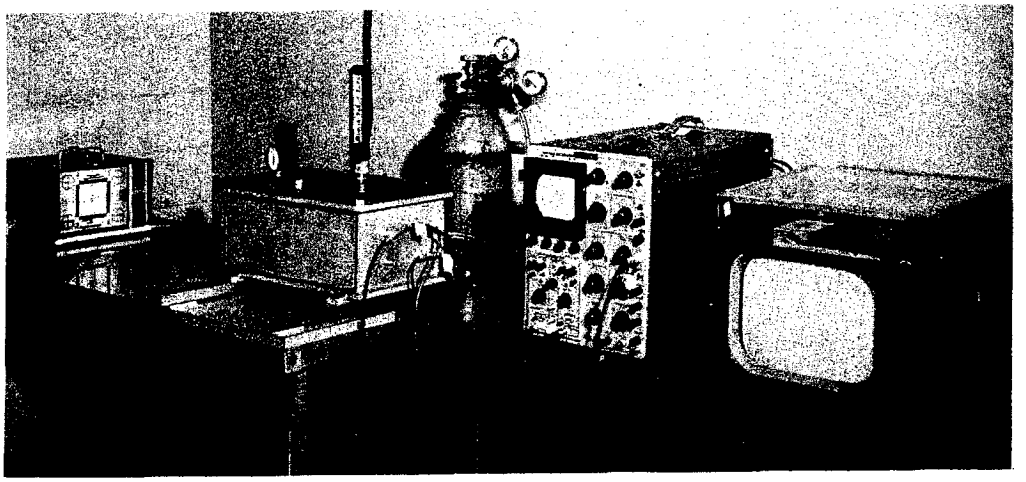

Fig. B-1 — Helium test setup

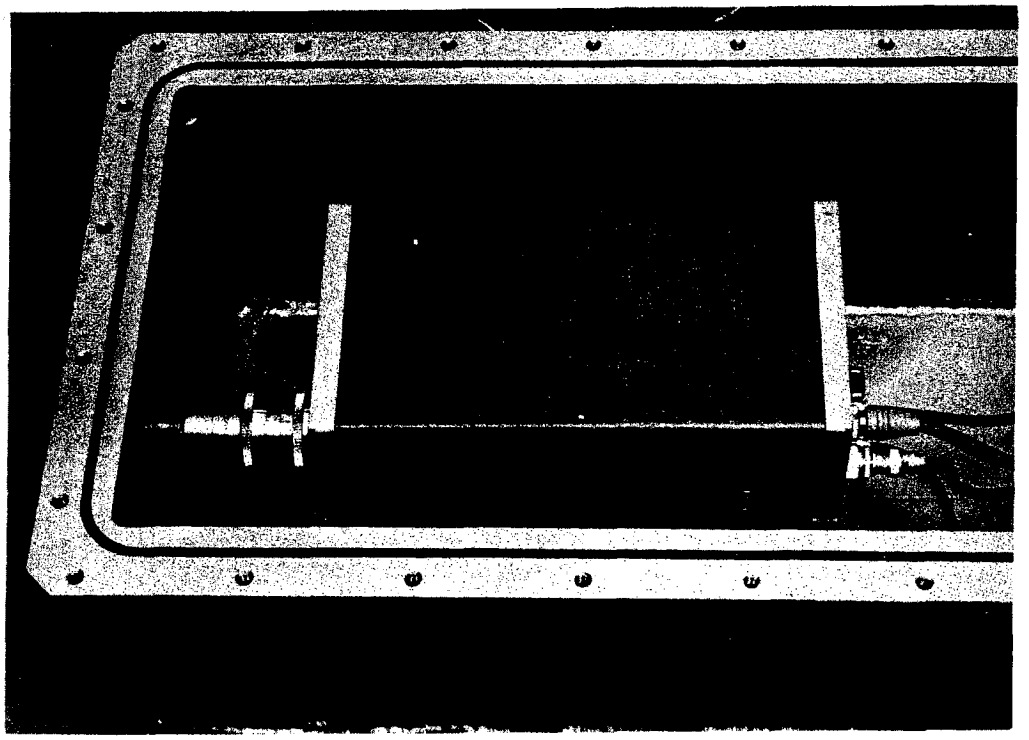

Fig. B-2 — Vidicon camera in helium chamber

The test was terminated on 16 November 1967, with the power cycle counter at 119.

2. DISCUSSION OF FAILURE MECHANISM

Helium permeation of glass has been investigated both theoretically and experimentally.[1,2,3]* These investigations have revealed that a simple Fickian diffusion model is well able to account quantitatively for the major features of experimental results. This model will not be described here. Suffice it to say that given the type and dimensions of a vidicon glass envelope as well as the temperature and partial pressure of the helium atmosphere, it is possible to determine the internal helium content of the vidicon tube as a function of time. Once this determination has been made, it is possible to consider the effects of the gas on performance.

Because helium is an inert gas, there will be no chemical reactions within the tube which might degrade performance. Rather, any possible degradation must be physical in origin. Among all possible degrading effects, there is one which obviously stands out. Its cause is the interaction between the electron scanning beam and the helium atoms within the vidicon. The consequences of this interaction are twofold: (1) the electron beam will be scattered by collisions between electrons and helium atoms; and (2) a radiating plasma will be generated by inelastic collisions. These two phenomena will be considered in turn below.

The scattering of an electron beam in a rarified gas is a function of several variables. These are the temperature, pressure, total scattering cross-section, and extent of the gas which the beam traverses. The total scattering cross-section is itself a function of the energy of the colliding electrons as well as of the kind of gas involved. Scattering due to both elastic and inelastic collisions is included in the total scattering cross-section. When these variables are all known, the amount of scattering can be determined by the equation[3,4]

$$\frac{I}{Io} = \exp\left(- \alpha p x \frac{To}{T}\right) \qquad \text{(B.1)}$$

where α = scattering coefficient (cm^2/cm^3 of gas at 0 °C and 1 torr)
p = gas pressure, torr
x = extent of gas traversed by beam, cm
To = reference absolute temperature (273.15 °K)
T = gas temperature, °K
I/Io = fraction of beam remaining unscattered

A plot of an experimental determination[5] of α for helium as a function of electron energy is given in Fig. B-3. In the case of a vidicon being permeated by helium, p is practically a linear function of time up to failure. Thus, because the other variables are almost time-invariant, the unscattered beam current should decrease exponentially as time increases linearly. This implies that, due to scattering alone, the signal current will also decrease exponentially with time.

Although test results have revealed that the signal current does indeed decrease with time when a vidicon is operated in a helium atmosphere, this decrease has not been observed to be a simple exponential function of time. Rather, the degradation shortly before complete failure has been extremely rapid in comparison with earlier degradation. This observation shows that there must be at least one other important phenomenon contributing toward eventual failure. The most

*References are listed in Section 4 of this appendix.

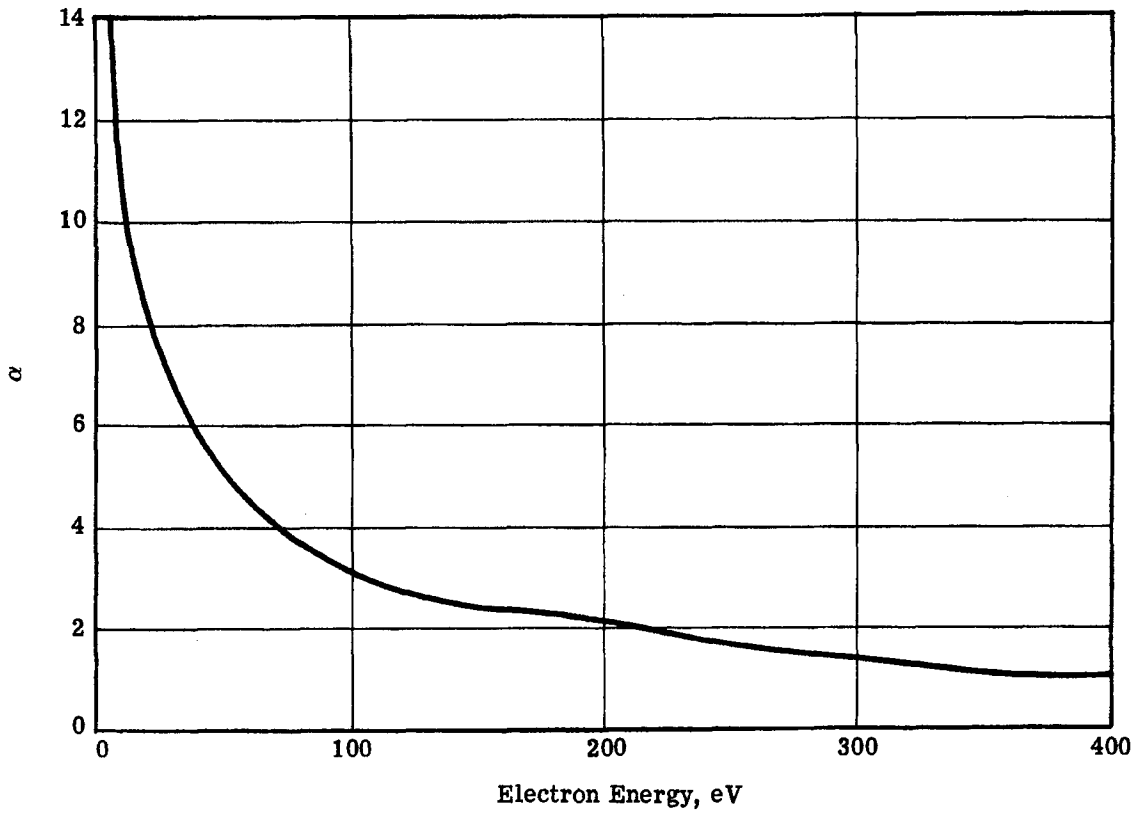

Fig. B-3 — Total scattering cross-section coefficient for electron-helium atom collisions (after Normand, 1930)

probable identity of this second important phenomenon has previously been mentioned. It is the generation of a radiating and conducting plasma within the vidicon by means of both primary and secondary inelastic electron-helium atom scattering. Although the appearance and importance of this phenomenon can hardly be doubted, a quantitative, theoretical discussion would be a very difficult undertaking. A qualitative discussion, however, can more readily be undertaken.

During normal operation of a 1-inch vidicon, the scanning electron beam must traverse a distance of about 10 centimeters from gun to collecting grid or target. The average beam electron begins this journey after being accelerated through approximately 300 volts. Since the ionization potentials for a singly and doubly ionized helium atom are 24.6 and 54.4 volts respectively, a 300 e-V electron is obviously capable of completely ionizing a helium atom during an inelastic collision. Even a secondary electron could induce ionization, especially if the colliding atom is already in an excited state. Secondary electrons will be produced not only through primary collisions, but also as a result of collisions between metastable helium atoms and the metallic vidicon electrodes. All these scattering and ionization processes will generate not only ions and free electons but also photons. When these photons impinge on the photoconductive layer of the vidicon, they will of course tend to "wash out" or obliterate the image impressed on the layer from the outside. The decelerating electric field just beyond the photoconductive layer will prevent discharge of the layer by the flux of secondary electons directed at it, but will be unable to prevent internally generated photons and slightly scattered primary electrons from seriously degrading the image. These degrading effects can be expected to increase rapidly as more and more helium permeates the vidicon envelope. Possibly some additional degradation may result from unwanted currents flowing through the conducting plasma between internal electrodes maintained at different potentials.

Although the reality of the aforementioned phenomena is quite credible, a theoretical, quantitative estimate of their contribution to the degradation in performance and eventual failure of a vidicon is unfortunately difficult to formulate. Further tests could materially assist such a formulation. It does seem quite reasonable, however, to ascribe test results already observed to the phenomena just discussed, especially since no other plausible failure mechanisms are evident. These conclusions would be further strengthened if observation of a helium immersed vidicon near failure revealed a glowing plasma within the tube.

3. DESIGN CONSIDERATIONS

The existing specification states that "on" orbit environment shall be 30 percent helium, 70 percent oxygen at either 5 psia or 14.7 psia with a total time of 2,500 hours. The worst case pressure gives a partial pressure of He of 4.4 psia.

Comparing this with the tests results of 200 hours of satisfactory performance at 15 psia He, mission time would be limited to 680 hours (15/4.4 x 200) if the vidicon tube is directly exposed to the environment.

It is presently planned to seal the vidicon tube from the outside environment (see Fig. B-4). However, the sealing materials are permeable to He; hence, it is not possible to completely exclude He from the vidicon tube. Based on the mission time of 2,500 hours and the test results, an average pressure of (15 x 200 hours/2,500 hours) 0.8 psia surrounding the vidicon would be satisfactory.

BIF-059-4035-69

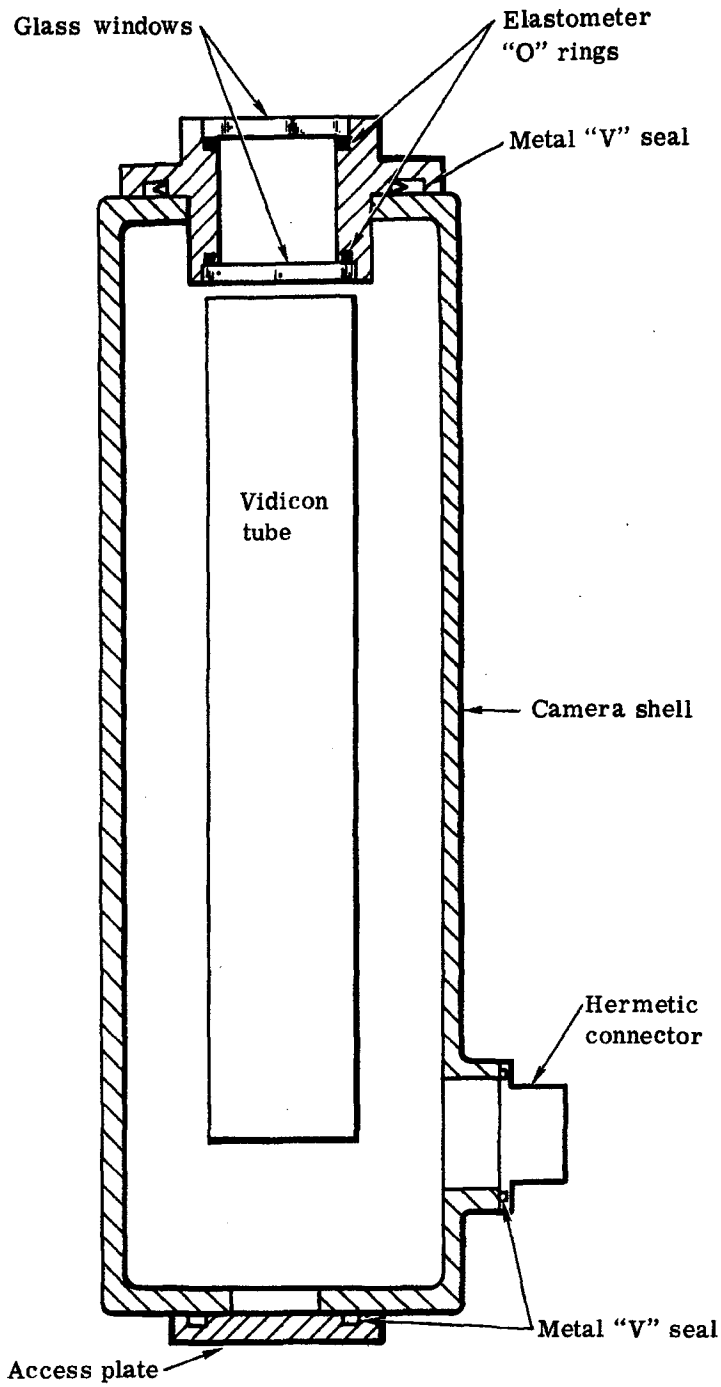

Fig. B-4 — Vidicon camera packaging

The empty volume around the vidicon tube is approximately 16 in.^{3}. The allowable helium flow rate into the camera shell is found as follows:

$$m' \leq \frac{m}{t} \leq \frac{P \cdot V}{R \cdot T \cdot t}$$

where m' = maximum flow rate, lb m/sec
m = total mass, lb m
t = time, sec = $2{,}500 \times 3{,}600 = 9.0 \times 10^6$ sec
R = gas constant = 386.33 ft-lb$_f$/lb m -°R
T = temperature, °R = 460 + 140 = 600 °R
P = allowable pressure at 2,500 hours = $(0.8 \times 2) = 1.6$ psia
V = volume = 16 in.^{3}

$$m' \leq \frac{(1.6 \times 144)\left(\frac{16}{1{,}728}\right)}{(386.33)(600)\,(9.0 \times 10^6)}$$

$$\leq 1.02 \times 10^{-12} \frac{\text{lb m}}{\text{sec}}$$

$$Q' = \frac{m'}{P}$$

where Q' = maximum flow rate, std cc/sec
P_{He} = 0.0104 lb m/ft^3 at STP

$$Q' \leq \frac{1.02 \times 10^{-12} \text{ lb m}}{0.0104 \frac{\text{lb m}}{\text{ft}^3}} \times 2.832 \frac{\text{cm}^3}{\text{ft}^3} \times 10^4$$

$$Q' \leq 2.78 \times 10^{-6} \frac{\text{std cc}}{\text{sec}}$$

The permeability constants of the seal materials at 140 °F are as follows:

Butyl "O" rings *

$$K = 3 \times 10^{-9} \frac{\text{std cc}}{\text{sec}} \frac{\text{cm thick}}{\text{cm Hg} \cdot \text{cm}^2 \text{ area}}$$

Glass windows†

$$K = 1 \times 10^{-10} \frac{\text{std cc}}{\text{sec}} \frac{\text{cm thick}}{\text{cm Hg} \cdot \text{cm}^2 \text{ area}}$$

*Handbook of Vacuum Physics vol. 3, part 4.
† Conservative estimate based on many published values of various glass types.

$$Q = K \cdot \frac{P \cdot A}{T}$$

where Q = flow rate, std cc/sec
K = permeability constant = std cc/sec . cm thick/cm^2 area
A = area, cm^2
P = pressure differential, cm Hg = 22.7 cm Hg
T = thickness, cm

The above equation does not account for the change in differential pressure with time which would give an exponential flow rate. However, for small He pressure increases, the equation is valid and conservative.

The camera will have a dual window which will be two pieces of glass in series, approximately 1.25 inches in diameter and 0.10 inch thick. One of the windows will be the field flattener. These will be sealed to a metal bezel with butyl "O" rings. The bezel in turn will be sealed to the camera shell with metal teflon coated "V" seals.

$$Q' \text{ "O" ring} = 3 \times 10^{-9} (L) (22.7) \times 2.52 \text{ cm/in.}$$

where L = length of seal, inches

$$Q' \text{ "O" ring} = 1.71 \times 10^{-7} (L) \frac{\text{std cc}}{\text{sec-in.}}$$

for 0.1-inch diameter cross-section "O" rings

$$Q' \text{ glass} = \frac{1 \times 10^{-10} \times \Pi/4 \, (1.25)^2 \times 22.7 \times 2.52 \text{ cm/in.}}{0.1}$$

$$= 7.0 \times 10^{-8} \text{ std cc/sec}$$

It is presently estimated there will be approximately 6 inches of seal length giving a Q' "O" ring = 1.026×10^{-6} std cc/sec.

As can be seen, the total permeation rate $[(1.03 + 0.07) \times 10^{-6}]$ of 1.10×10^{-6} std cc/sec is less than the allowable of 2.78×10^{-6} by a factor of approximately 3. Additionally, the redundant window seal will provide a reduced flow rate as a function of the volume between the two windows, and the rate is computed for a worst case temperature and pressure.

Further testing will be required to validate the computed leakage rates and the performance of the vidicon tube in a helium environment versus time.

Additional testing and analysis are required to evaluate the intensifier performance in a helium environment. Consideration must be given to the relatively high voltage potentials within the tube and the permeability of the fiber optic faceplates.

4. REFERENCES

1. Studt, P. L., Mechanism of Gaseous Permeation through Glass, Single-Crystal Silicon and Germanium, and Stress-Enhanced Gaseous Permeation Through Alumina Bodies, University of California, Lawrence Radiation Laboratory, Berkeley, NASA N63-11998 (1962).

2. Rode, J. J., Permeation of Helium into Vacuum Tubes, Bendix Corporation Clearinghouse, U. S. Dept. of Commerce, BDX-613-30 (1964).
3. Massey, H. S. W., and Burhop, E. H. S., "Electronic and Ionic Impact Phenomena," Clarendon Press, Oxford, 1952.
4. Chantry, P. J., Phelps, A. V., and Schuly, G. J., Theory of Electron Collision Experiments at Intermediate and High Gas Densities, Westinghouse Research Laboratory, Pittsburgh, Pennsylvania, AD636533 (1966).
5. Normand, C. E., The Absorption Coefficient for Slow Electrons in Gases, Phys. Rev. 35:1217 (1930).